

MULTI-WAVELENGTH STUDIES
OF VHE GAMMA-RAY BLAZARS

A Dissertation

Submitted to the Faculty

of

Purdue University

by

Daniel D. Gall

In Partial Fulfillment of the

Requirements for the Degree

of

Doctor of Philosophy

August 2010

Purdue University

West Lafayette, Indiana

To my wife, Jacquie, for her unlimited patience and love, and
to my parents for their unwavering support.

“It’s all really there ... but you’ve got to stop and think about it to really get the pleasure about the complexity; the inconceivable nature of nature.”

–*Richard Feynman*

ACKNOWLEDGMENTS

I would first like to give thanks for the personal (and financial!) support provided by my wife, Jacquie, and my parents, David and Becky, throughout my years of graduate study. The completion of this dissertation would not have been possible without their constant encouragement and support. In addition, my close friend, Elliot Gruszka, has been supportive throughout my career in physics, and my friends John Millis and Josh Shive have provided me moral support and the hope that graduate school really does come to an end.

I have many people to thank for their contribution to my professional development. My advisor Wei Cui has made his years of knowledge and experience available to me and has deepened my understanding of the complexity of the universe that we live in. In addition, through his support I have been able to interact with colleagues from around the world through meetings and conferences.

I would like to thank Glenn Sembroski for the many useful conversations concerning VERITAS, data analysis and astrophysics in general. His support has been essential to my development at Purdue. I would like to thank Markus Böttcher for many helpful discussions concerning blazar modeling and his contributions to my work. I also need to extend thanks to Brian Humensky and Niklas Karlsson for being consistently helpful in answering my questions about the details of VERITAS analysis. In addition, I want to thank my dissertation committee members, John P. Finley, Matthew L. Lister, and Thomas E. Clark, for the advice they have given and the knowledge they have shared with me throughout my time at Purdue.

I am also grateful for the group of graduate students that I have had the opportunity to study with during my time at Purdue. Ben Zitzer, in particular, has been a great help through discussions about VERITAS and our respective research. I have received significant help from other members of my advisor's research group. Yongquan

Xue, Gabor Pszota, Chulhoon Chang, Angelo Varlotta and Miguel Araya-Arguedas have all contributed to my work through sharing their experience and general discussions on research. They have also allowed me to understand other areas of study in better detail.

TABLE OF CONTENTS

	Page
LIST OF TABLES	viii
LIST OF FIGURES	ix
SYMBOLS	xiv
ABBREVIATIONS	xv
ABSTRACT	xvi
1 Introduction	1
1.1 Observations and Classification of Active Galactic Nuclei	1
1.1.1 A Unified Model for AGN	1
1.1.2 The Blazar Class of AGN	4
1.1.3 Relativistic Effects: Beaming and Doppler Boosting	7
1.2 Emission Models for TeV Blazars	9
1.2.1 Leptonic Models: Synchrotron Self Compton	10
1.2.2 Hadronic Models	11
1.3 Motivation and Structure	12
2 X-ray Astronomy	15
2.1 XMM-Newton	15
2.1.1 Instrumentation and Characteristics	15
2.1.2 EPIC-PN Observing Modes and Data Analysis	19
2.1.3 OM Observing Modes and Data Analysis	23
2.2 Suzaku	24
2.2.1 Instrumentation and Characteristics	24
2.2.2 XIS Observing Modes and Data Analysis	26
2.2.3 HXD Data Analysis	31
3 Gamma-ray Astronomy	33
3.1 Imaging Atmospheric Cherenkov Technique	33
3.1.1 Electromagnetic Showers	34
3.1.2 Cherenkov Radiation from Electromagnetic Showers	35
3.1.3 Imaging Atmospheric Cherenkov Telescopes	38
3.2 VERITAS	43
3.2.1 VERITAS Hardware	43
3.2.2 VERITAS Data Analysis	54
4 A Multiwavelength Study of the Blazar Markarian 421	73

	Page
4.1 Introduction	73
4.2 Observations and Data Reduction	75
4.2.1 XMM-Newton Observations	75
4.2.2 TeV Gamma-Ray Observations	77
4.3 Results	85
4.3.1 Time Averaged TeV Gamma-Ray Spectra	85
4.3.2 Spectral Energy Distribution and Modeling	86
4.3.3 Cross-Band Correlation	88
4.3.4 Spectral Hysteresis	93
4.4 Discussion	93
5 Spectral Energy Distribution of Markarian 501: Quiescent State vs. Extreme Outburst	99
5.1 Introduction	99
5.2 Data Selection and Analysis	101
5.2.1 Suzaku: X-ray	101
5.2.2 VERITAS: VHE γ -ray	103
5.2.3 MAGIC: VHE γ -ray	105
5.2.4 Fermi: γ -ray ($20 \text{ MeV} < E < 300 \text{ GeV}$)	106
5.2.5 Results	108
5.2.6 Discussion	112
6 Summary and Future Work	119
LIST OF REFERENCES	121
A VERITAS Analysis Pipeline Automation	125
A.1 Introduction	125
A.2 Filesystem	125
A.2.1 ROOT	125
A.2.2 VEGAS	126
A.2.3 Data Files	126
A.2.4 Configuration Files and Lookup Tables	127
A.3 Initial Configuration	127
A.4 vaMProc	128
A.5 vaPipe	132
A.6 vaPipe: Code	132
A.7 vaMProc: Code	146
VITA	157

LIST OF TABLES

Table	Page
2.1 PN Observing Modes	19
3.1 Image parameters as currently calculated for VERITAS analysis.	62
4.1 Summary of Markarian 421 <i>XMM-Newton</i> Observations.	77
4.2 Whipple Event Selection Parameters	79
4.3 MAGIC Cuts. Leakage parameter is defined as the ratio of the signal in the outer pixels of the camera to the total signal.	81
4.4 VERITAS Cuts	83
4.5 Gamma-ray data run information. Some data were removed due to adverse meteorological conditions.	84
4.6 SED Model Parameters	89
5.1 SED Model Comparisons	113
5.2 Cooling Timescales	117

LIST OF FIGURES

Figure	Page
1.1 A diagram of AGN types. Though they make up only a few percent of the overall AGN population, blazars are the dominant type detected in VHE γ -rays.	2
1.2 An illustration showing the geometric arguments for inferring emission region radius from variability timescale.	3
1.3 An illustration depicting the unified model of AGN components. The model attributes the differing AGN types to the observer's viewing angle. Several different viewing angles are labeled with their associated AGN type. Image credit:NASA	5
1.4 Observational characteristics of the blazar Markarian 421.	6
1.5 An illustration depicting the relativistic beaming effect. The photons emitted by the cloud moving with relativistic velocities are highly beamed within a cone of half angle of $1/\gamma$	7
1.6 An illustration depicting the relativistic Doppler shift. Adapted from [85].	9
2.1 An illustration depicting the opaqueness of the atmosphere across the electromagnetic spectrum. Most frequencies are inaccessible from ground based observatories and must utilize space-based or other alternatives for detection. Image credit: ESA/Hubble.	16
2.2 A model showing the XMM-Newton scientific instruments. Image courtesy ESA.	17
2.3 Image of one of the three X-ray telescope mirror assemblies aboard XMM-Newton. Image courtesy of ESA.	17
2.4 Illustration of grazing mirrors. The incoming X-ray photons are reflected off from mirrors at a very low angle of incidence.	18
2.5 A preflight image (a) and schematic view (b) of the PN detector array.	18
2.6 Examples of the operating modes of XMM PN. The upper left shows full frame mode and the upper right shows windowed mode with a large window. The lower left shows windowed mode with a small window, and the lower right shows an example of timing mode. Note the loss of imaging in one dimension during timing mode. Image courtesy ESA.	20

Figure	Page
2.7 A schematic of the optical monitor aboard <i>XMM-Newton</i> . Image courtesy ESA.	23
2.8 A plot of the effective areas of the OM when different filters are in operation. Image courtesy ESA.	24
2.9 Schematic view of the Suzaku spacecraft. [74]	25
2.10 Schematic drawing of the HXD. [?]	27
2.11 XIS effective area for a single XRT showing Image courtesy NASA. . .	28
2.12 Illustration of the XIS 5 x 5, 3 x 3, and 2 x 2 editing modes. Image courtesy NASA.	29
3.1 A simple model of an electromagnetic shower in the upper atmosphere initiated by a photon with energy E . The energy per particle or photon is shown for each level on the left. Adapted from [65], Figure 4.17.	36
3.2 Simulations showing a air shower simulations and simulated Cherenkov telescope images for a γ -ray initiated electromagnetic shower, a hadronic shower, and a hadronic shower with a muon ring in the camera. Note the additional transverse components in the hadronic showers and the difference in images produced in the camera plane. Adapted from [73]; simulations courtesy Glenn Sembroski, Purdue University.	37
3.3 An illustration of the imaging of an electromagnetic shower in the focal plane of an imaging Cherenkov telescope that is located within the Cherenkov light pool of the electromagnetic shower. Image from [33]. .	40
3.4 An example of a γ -ray event triggered in all four telescopes of the VERITAS array. The semi-major axes of each ellipse are extended and intersect at the shower core location. Archival VERITAS image.	42
3.5 The VERITAS experiment located at the Fred Lawrence Whipple Observatory near Tucson, AZ. Archival image courtesy the VERITAS collaboration.	43
3.6 An image of VERITAS telescope 1 showing the 12 m optical support structure with 350 mirror facets and the camera box at the 12m focal point of the optics. (As of the time of writing, telescope 1 has been moved from the location pictured here to a location providing more uniform separation between the telescopes in the array.)	45
3.7 The PSF of a VERITAS telescope before (left) and after (right) mirror alignment. The circle indicates the size of a PMT. Plot taken from [72].	46

Figure	Page
3.8 Images of a VERITAS camera without the light cones mounted (a) and the light cones that are mounted to the front of the camera to reduce light lost between pixels and light not coming from the mirrors (b). Archival images courtesy of the VERITAS collaboration.	46
3.9 A schematic diagram of a typical PMT.	47
3.10 An image of a pixel from the VERITAS camera before assembly. The inset shows a close up of the preamplifier board. Image from [76].	47
3.11 A plot quantum efficiency of a Photonis PMT over several wavelengths. Image Credit: Ben Zitzer.	48
3.12 A block diagram of the CFDs used for the VERITAS Level 1 trigger. Image taken from [53].	51
3.13 A plot of the mean pedestal value vs. the pedvars for a single telescope.	56
3.14 A plot of the distribution of T_{offset} values for all the pixels in a single telescope. The y-axis shows the log of the number of pixels and the x-axis shows the T_{offset} value in ns.	57
3.15 A plot of the distribution of relative gain values for all the pixels in a single telescope. The y-axis shows the log of the number of pixels and the x-axis shows the relative gain value.	59
3.16 A plot of the distribution of relative pedvars for all the pixels in a single telescope. The y-axis shows the log of the number of pixels and the x-axis shows the relative pedvar value. The window of allowed relative pedvar values from -1.5 to 4 is shown.	60
3.17 An illustration of some of the Hillas parameters used for analysis.	61
3.18 A plot of shower core locations shown in ground coordinates.	64
4.1 TeV spectral analysis results, showing the data obtained with MAGIC (squares, $\alpha = 2.28 \pm 0.09$ and $F_0 = 2.49 \pm 0.17$), <i>Whipple</i> (diamonds, $\alpha = 2.23 \pm 0.38$ and $F_0 = 2.65 \pm 0.77$) and <i>VERITAS</i> (crosses, $\alpha = 2.91 \pm 0.13$ and $F_0 = 2.01 \pm 0.15$).	86
4.2 Spectral energy distribution with the SSC model for the 2006 (teal blue) and 2008 (red) data. The data from <i>XMM-Newton OM</i> , <i>XMM-Newton EPN</i> , <i>MAGIC</i> , <i>Whipple</i> and <i>VERITAS</i> are shown with triangles, filled circles, squares, diamonds, and crosses, respectively, with data taken during the <i>MAGIC</i> , <i>Whipple</i> and <i>VERITAS</i> observation times shown in green, blue and red. Error bars for the XMM-Newton OM data and much of the XMM-Newton EPN data are smaller than the data points.	88

Figure	Page
4.3 Plot of light curves from (a) 2006 observations and (b) 2008 observations. <i>XMM-Newton</i> OM data (200-300nm) is shown with triangles in units of cts s^{-1} . <i>XMM-Newton</i> EPN data (0.5 - 10.0 keV) is shown with filled circles in units of cts s^{-1} . Error bars for the EPN data are smaller than the data points. The data from <i>MAGIC</i> , <i>Whipple</i> and <i>VERITAS</i> are shown with squares, diamonds, and crosses, respectively in units of $\text{photons cm}^{-1} \text{s}^{-2}$ (above 250 GeV). Note that the EPN and OM scales differ on the 2006 and 2008 panels.	90
4.4 Plot of simultaneous <i>XMM-Newton</i> EPN (0.5 - 10 keV) and TeV data to search for correlation between the two bands. <i>MAGIC</i> data points are designated by squares, <i>Whipple</i> points by diamonds, and <i>VERITAS</i> points by crosses. All <i>XMM-Newton</i> data used for this plot was analyzed with XMMSAS version 8.0.0 to maintain consistency. The dotted line is the X-ray/TeV gamma-ray correlation best fit from [19] converted to the appropriate units. The dot-dashed line has the same slope but is scaled to the average of our <i>Whipple</i> 10m results.	92
4.5 Hardness ratio vs intensity plots to study spectral hysteresis during the increase in activity centered around 17 ks into the 2006 <i>XMM-Newton</i> observation. Three bands are used for this analysis. The upper panel uses (3-10 keV)/(1-3 keV) for the hardness ratio, the middle panel uses (1-3 keV)/(0.5-1 keV), and the bottom panel uses (3-10 keV)/(0.5-1 keV). The arrows indicate the progression of time. Clockwise hysteresis is present in all three panels, indicating a lag in the lower energy bands.	94
5.1 Time coverages of Mrk 501 by the instruments involved in the multi-wavelength campaign. Data gaps due to orbital constraints are not indicated.	103
5.2 Light curves of Mrk 501 in the passing band of Suzaku/HXD, Suzaku/XIS, <i>MAGIC</i> and <i>VERITAS</i>	109
5.3 Observed X-ray spectrum of Mrk 501. They were made from the XIS and HXD/PIN data separately. The solid histogram shows the best fits to the data with a broken power-law model (see text). The bottom panel shows the residuals of the fit.	112
5.4 VHE spectrum from <i>VERITAS</i> (diamonds) and <i>MAGIC</i> (triangles), including the best fits power law models. <i>VERITAS</i> model shown with solid line, and <i>MAGIC</i> model shown with dashed line. The slopes of the power law models agree well, with a slight normalization offset, corresponding to the moderately higher TeV flux levels during the <i>MAGIC</i> observation.	113

- 5.5 Spectral energy distributions of Mrk 501 in the quiescent state (in blue) and in an extreme outburst (in red). The former were made from data obtained in the present campaign with Suzaku (filled circles), Fermi (squares), VERITAS (diamonds), and MAGIC (triangles). The latter were taken from [77], with X-ray data from BeppoSAX (open circles), GeV gamma-ray upper limit from EGRET, and TeV γ -ray data from Whipple (star). Corresponding fits for each year are shown. The solid lines show the SSC fit, dotted lines take EBL absorption into account. The TeV data points are not EBL corrected. 114

SYMBOLS

m	mass
v	velocity
c	speed of light in vacuum
β	v/c
P	power
ν	frequency
F	flux
γ	Lorentz factor
δ	Doppler factor

ABBREVIATIONS

AGN	Active Galactic Nuclei
CCD	Charge Coupled Device
EPIC	European Photon Imaging Camera (<i>XMM-Newton</i>)
HXD	Hard X-ray Detector (<i>Suzaku</i>)
IACT	Imaging atmospheric Cherenkov Technique (or sometimes Telescope)
OM	Optical Monitor (<i>XMM-Newton</i>)
PMT	Photomultiplier Tube
VBF	VERITAS Bank Format
VERITAS	Very Energetic Radiation Imaging Telescope Array System
VHE	Very High Energy ($E > 100$ GeV)
XIS	X-ray Imaging Spectrometer (<i>Suzaku</i>)
XRT	X-ray Telescope (<i>Suzaku</i>)

ABSTRACT

Gall, Daniel D. Ph.D., Purdue University, August 2010. Multi-wavelength Studies of VHE Gamma-ray Blazars. Major Professor: Wei K. Cui.

Blazars, particularly those detected in TeV γ -rays, are some of the most violent astrophysical objects yet observed. They display extreme variability on multiple timescales over a broad range of energies. These sources make excellent laboratories for studying the environment within the jets of active galactic nuclei, as the bulk of the detected emission is from the jets. These sources have been well studied at multiple wavelengths, and much insight has been gained into the nature of these extreme objects. This work described in this dissertation attempts to expand the understanding of two particular blazars, Markarian 421 and Markarian 501, by improving on previous observational techniques and utilizing state of the art detectors for obtaining data.

The first project described focused on obtaining strictly simultaneous multi-wavelength data, covering a broad energy range, to search for any multi-wavelength correlations and to provide an accurate spectral energy distribution. This simultaneous data is essential for these sources due to their rapid variability. The most widely accepted models for emission within blazars, known as synchrotron self Compton, depend on a strong connection between the X-ray and γ -ray photons. The simplest of these models predicts a strong correlation between the observed flux in these two bands, but this study did not observe such a correlation, though the synchrotron self Compton models could match the data.

The second project focused on obtaining a state of the art measurement of the quiescent state of the blazar Markarian 501. This object is generally quite weak, and previous very high energy ($E > 100$ GeV) γ -ray experiments were not able to

detect the source in the quiescent state. Neither was the source detected by previous γ -ray space telescopes operating in a lower energy range. This project used data from the current generation of experiments to obtain a carefully sampled spectral energy distribution of the source in the quiet state and investigated some of the characteristic timescales involved in this state.

1. Introduction

1.1 Observations and Classification of Active Galactic Nuclei

The spectra of most galaxies typically show absorption lines and are the result of the combined light of all the stars within these galaxies. A smaller subset of galaxies have been found to have significantly different spectral properties, particularly emission lines superimposed on top of the normal spectra. The first of these galaxies was identified in 1908 by Edward A. Fath while he was studying the spectral properties of a number of galaxies [39]. He observed broad emission lines in the galaxy NGC 1068. Emission lines from NGC 1068 as well as two other galaxies were confirmed by Edwin Hubble in his study of “extragalactic nebulae” [47].

The broad emission lines noted by Fath and Hubble were later associated with bright galactic nuclei by Carl K. Seyfert [87]. These galaxies were the first species of a “zoo” of what became known as active galactic nuclei (AGN). This zoo consists of Seyfert galaxies, radio galaxies, quasars, QSOs and blazars. Most of these galaxies share in common a continuum of emission over a broad range of frequencies. This continuum spectrum is non-thermal and is easily distinguishable from the blackbody spectra of stars or the combined spectra of many stars in typical galaxies.

A diagram of the various AGN types is shown in Figure 1.1.

1.1.1 A Unified Model for AGN

A geometric model for unifying the the many types of AGN based on the observer’s line of sight has been widely accepted [92]. This model describes the basic components that are thought to be shared among all AGN. The central engine that drives the emission is thought to be a supermassive black hole with typical masses on the order

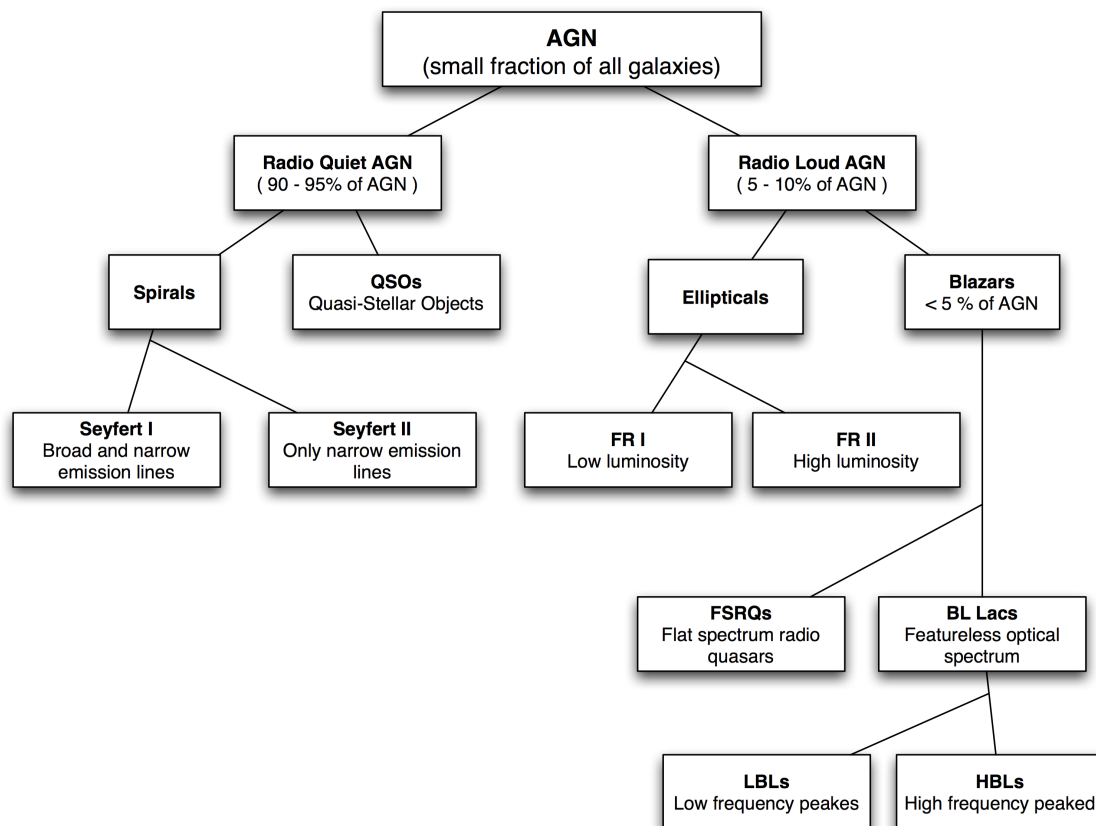


Figure 1.1. A diagram of AGN types. Though they make up only a few percent of the overall AGN population, blazars are the dominant type detected in VHE γ -rays.

of $10^8 M_{\odot}$. Accretion onto a black hole provides an efficient method to liberate the potential energy of inflowing matter in the form of the extreme luminosities observed. In addition, the rapid variability observed in many AGN provides a strong argument for the luminosities to be emerging from a very compact region within the nucleus of the galaxy.

For AGN, the size of the emitting region can be inferred from the variability timescale of the source. An upper limit maybe placed on the size of the emission region using speed of light constraints. For an optically thick, spherical emission

region that rapidly increases in brightness, the increase in brightness is communicated to the observer first by photons from the nearest part of the sphere. The variability signature from the edge of the sphere arrives last, smearing out the brightening time by a factor of $\Delta t \approx R/c$ for distant sources where R is the radius of the emission region (see Figure 1.2). If the emission region is moving with respect to the observer and at a distance corresponding to a redshift z , the upper limit on the radius of the emission region can be found to be:

$$R \leq \frac{\delta c \Delta t}{(1+z)}, \quad (1.1)$$

where δ is the Doppler factor, discussed in Section 1.1.3. In a simplified scenario for a nearby source with variability on the order of 1 hour (sub-hour variability has been observed) and a Doppler factor of 1, the radius can be found to be on the order of 10^{14} cm, about 7 times the distance from the Earth to the Sun [29].

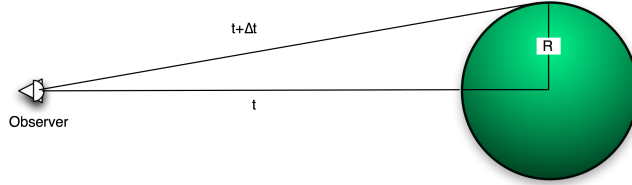


Figure 1.2. An illustration showing the geometric arguments for inferring emission region radius from variability timescale.

In addition, a lower limit on the mass within this emission region can be found assuming that the object is emitting at the Eddington luminosity. Beyond this luminosity, the outward transfer of momentum by radiation overpowers the inward gravitational force and accretion will cease. For ionized hydrogen, the Eddington luminosity is:

$$L_{Edd} = 1.3 \times 10^{38} \frac{M}{M_{\odot}} \text{ ergs s}^{-1}. \quad (1.2)$$

For a luminosity of $\sim 10^{46}$ erg s^{-1} (the bolometric luminosity of Markarian 421), the lower limit on the mass is $\sim 10^8 M_{\odot}$. A mass this large confined to the small space

implied by the variability constraints is strong evidence for the central engine to be a supermassive black hole.

Surrounding the central black hole is a hot accretion disk that emits thermally in the UV to soft X-ray range. This disk in turn is surrounded by an optically thick dusty torus. Rapidly moving clouds which produce Doppler broadened emission lines are located above (and below) the accretion disk. These clouds are responsible for the broad lines noted by Fath and Hubble. Further out from the disk, slower moving clouds produce narrow emission lines. In radio-loud AGN, powerful, relativistic jets of particles flow out for the region near the central black hole, oriented generally perpendicular to the accretion disk. Charged particles within these jets emit synchrotron radiation in the range from radio through X-ray. These jets are absent in radio quiet AGN.

Some of the different AGN classes are thought to arise from the angle at which the observer views the AGN. As galaxies are randomly oriented on the sky, many different viewing arrangements are possible, resulting in different properties as measured by the observer. When viewed edge on, the dusty torus will obscure the broad line emission regions close to the accretion disk, allowing only the narrow emission lines to be detected. At steeper angles to the accretion disk, both broad and narrow lines can be observed. The blazar class of AGN arises when the observer's viewing angle is oriented very closely to the axis of the jets in a radio-loud AGN. Figure 1.3 shows an illustration of the various AGN components and the viewing angle effects.

1.1.2 The Blazar Class of AGN

The focus of this dissertation is on the blazar class of AGN. While all AGN are quite spectacular objects, blazars are, observationally, the most powerful and extreme emitters due to the close alignment of their jets to the observer's line of sight. Blazars characteristically have highly variable non-thermal emission across all energy bands, thought to originate within highly relativistic jets of material. The rapid variability

of these objects implies that the extreme emission is produced within highly compact regions, and the small angles to the line of sight result in relativistic effects such as beaming and apparent superluminal motion. In addition, the observed variability occurs on a broad range of timescales from flares on the order of minutes to larger outbursts lasting weeks or months (see Figure 1.4(a)).

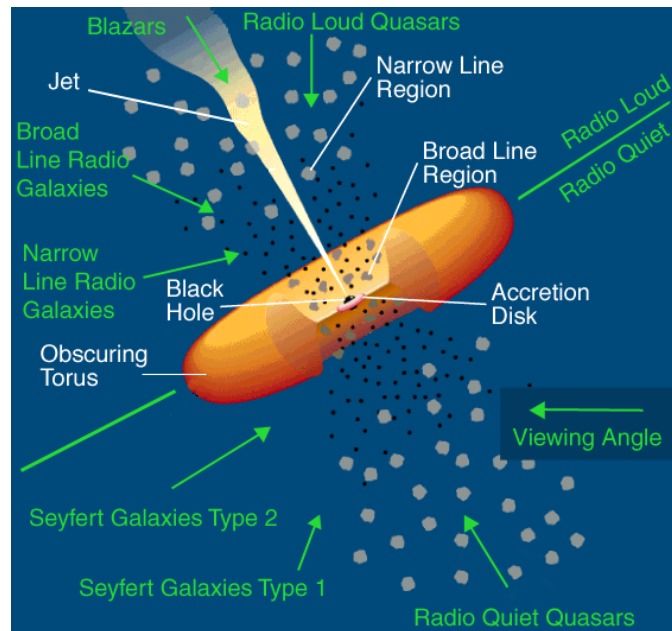
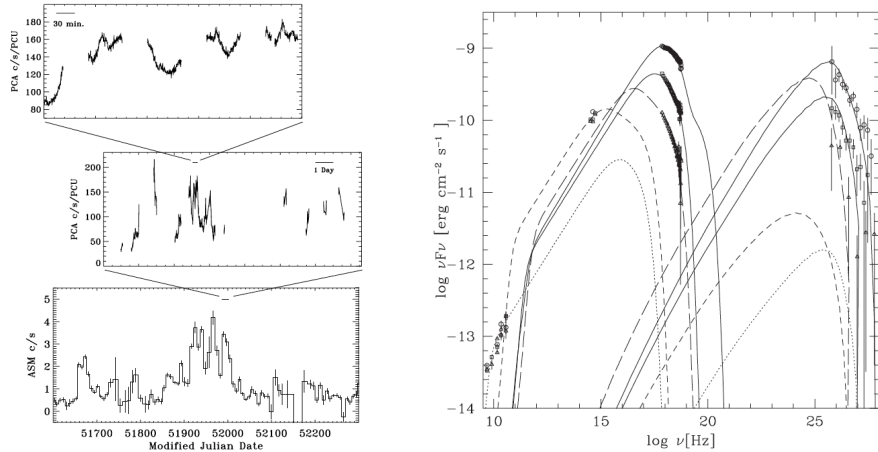


Figure 1.3. An illustration depicting the unified model of AGN components. The model attributes the differing AGN types to the observer's viewing angle. Several different viewing angles are labeled with their associated AGN type. Image credit:NASA

TeV blazars, or those that are detected in TeV γ -rays, emit similar amounts of power at both X-ray and TeV energies, making these bands particularly important for studying their characteristics. The typical blazar SED, when plotted as νF_ν against ν , displays two spectral peaks. The lower energy peak for TeV blazars occurs in the X-ray energy band while the higher energy peak occurs in TeV γ -rays (see Figure 1.4(b)). Models attempting to replicate the SED patterns measured by multi-wavelength observations are critical to gaining understanding about the emission

mechanism and the environment within the AGN jet. A general description of these models can be found in Section 1.2.

The name blazar was coined by the astronomer Ed Spiegel in 1978 and is a combination of the names of the two types of objects that make up the blazar class: BL Lacertae type objects (BL Lacs) and flat spectrum radio quasars (FSRQs). FSRQs are highly variable quasars that have broad emission lines within their spectra. They are also known as optically violent variable quasars (OVVs) and make up a small percentage of all quasars. BL Lacs, named for the prototype object BL Lacerta, generally show no emission lines (or possibly very weak lines). Though spectral lines are the primary difference between the two types of blazars, there are also differences between the level of polarization at certain wavelengths and the ratio of fluxes within different energy bands.



(a) Flaring observed at multiple timescales in X-ray observations of Markarian 421. Figure from [35].

(b) An SED plot for multiple observations of Markarian 421. The two peaked profile is common among blazars, though the peaks occur at varying energies. Figure from [19].

Figure 1.4. Observational characteristics of the blazar Markarian 421.

1.1.3 Relativistic Effects: Beaming and Doppler Boosting

Blazars make excellent laboratories for studying the acceleration processes within the relativistic jets of AGN because the emission coming from the jets is boosted in both frequency and intensity due to relativistic effects. Relativistic beaming results in much of the emitted radiation being beamed along the direction of the bulk motion of the jet. For blazars, this direction is very close to the observer's line of sight, so the intensity of the radiation from the jet is boosted significantly for the observer. In addition, the relativistic Doppler effect can significantly boost the frequency at which the radiation is observed.

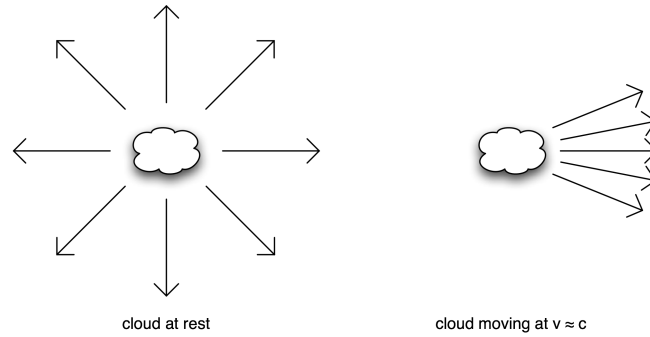


Figure 1.5. An illustration depicting the relativistic beaming effect. The photons emitted by the cloud moving with relativistic velocities are highly beamed within a cone of half angle of $1/\gamma$.

Relativistic beaming occurs when the source emitting radiation is moving at relativistic velocities. Figure 1.5 illustrates this effect. A light source is at rest in frame S' and emitting light isotropically. In the observer's frame S , the source is moving with relativistic velocity u in the x direction. To find the direction in frame S of a light ray that in frame S' is emitted perpendicular to the x -axis, velocity transforms must be made [29]:

$$v_x = \frac{v'_x + u}{1 + uv'_x/c^2} = u \quad (1.3)$$

$$v_y = \frac{v'_y \sqrt{1 - u^2/c^2}}{1 + uv'_x/c^2} = c \sqrt{1 - u^2/c^2} \quad (1.4)$$

This shows that the light ray is no longer traveling perpendicular to the direction of motion of the light source as measured in the S frame. Instead it is emitted at some angle θ from the x -direction. This angle is defined as $\sin \theta = v_y/v$ or, from Equations 1.3 and 1.4, $\sin \theta = \sqrt{1 - u^2/c^2} = \gamma^{-1}$. Here, γ is the Lorentz factor of the moving light source. For highly relativistic speeds, when $u \approx c$, the angle becomes very small and the light emitted in the hemisphere towards the direction of motion of the source is tightly beamed into a cone of light with half angle $1/\gamma$.

The relativistic Doppler effect works to shift the frequencies observed from those emitted by the source [85]. Consider the situation depicted in Figure 1.6. In the observer's rest frame a source emitting photons is moving with relativistic velocity v . The source emits one full period of radiation, with a frequency of ν' in the source frame, as it travels from point 1 to point 2. The observer measures the time taken to move from 1 to 2 as:

$$\Delta t = \gamma \frac{1}{\nu'} . \quad (1.5)$$

The difference in arrival times, as measured by the observer, of the radiation emitted at point 1 and point 2 will differ by Δt minus the time it takes the light to travel distance d (as shown in Figure 1.6:

$$\Delta t_{obs} = \Delta t - \frac{d}{c} = \Delta t - \frac{l \cos \theta}{c} = \Delta t - \frac{v \Delta t \cos \theta}{c} = \Delta t \left(1 - \frac{v}{c} \cos \theta \right) . \quad (1.6)$$

This means the observer will measure a frequency of:

$$\nu = \frac{1}{\Delta t_{obs}} = \frac{\nu'}{\gamma \left(1 - \frac{v}{c} \cos \theta \right)} = \delta \nu' , \quad (1.7)$$

where δ is known as the Doppler factor. It can be seen that for small values of θ , the effect becomes more important.

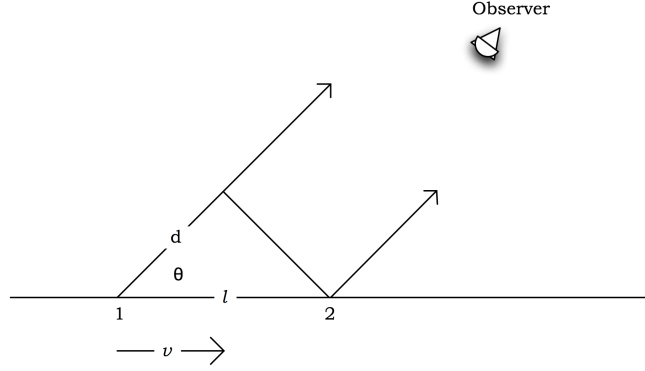


Figure 1.6. An illustration depicting the relativistic Doppler shift. Adapted from [85].

1.2 Emission Models for TeV Blazars

Many models have been proposed that attempt to explain the broad band SEDs and variability patterns observed in TeV blazars. The consensus among the models is that the low energy peak in the SEDs can be attributed to synchrotron radiation from relativistic electrons and positrons in the blazar jet. The total power emitted by synchrotron radiation for a collection of electrons with isotropic pitch angles is:

$$P_{syn} = \frac{4}{3} \sigma_T c \beta^2 \gamma^2 U_B , \quad (1.8)$$

where σ_T is the Thompson cross section and U_B is the magnetic energy density within the emission region [85]. This synchrotron radiation peaks at:

$$\nu_{syn} = \frac{4}{3} 2.8 \times 10^6 B \gamma^2 \frac{\delta}{1+z} \text{ Hz} , \quad (1.9)$$

where ν_{syn} is the frequency of the synchrotron peak, $2.8 \times 10^6 B$ is the Larmor frequency and γ is the Lorentz factor of the bulk of the electrons.

The two primary classes of blazar emission models are named for the particles that they utilize to explain the high energy SED peak. These two model classes, hadronic and leptonic, are discussed below along with the mechanisms exploited to explain the emission observed in the sources.

1.2.1 Leptonic Models: Synchrotron Self Compton

The most popular and widely accepted emission models for TeV blazars are of the type known as synchrotron self Compton (SSC). These models explain the high energy peak of the SEDs with the non-thermal electrons inverse Compton up scattering the photons they have already emitted to higher energies. This class of models was first developed in 1969 [52] and was later applied to emission from relativistic jets.

Simple SSC models use a single, usually spherical, emission zone moving in a relativistic jet of material. The key parameters usually involved in these models are the size of the emission region, the bulk Lorentz factor of the material in the jet, the energy spectrum of the electrons that are injected into the jet, and the magnetic field within the emission region.

The energetic electrons interacting with the magnetic field emit synchrotron radiation. Some of these synchrotron photons then become the “seeds” for emission at higher energies. In the SSC scenario, the high energy peak is the result of inverse Compton interactions between the same population of high energy electrons and the synchrotron photons they produce. The power lost by an electron undergoing inverse Compton scattering is:

$$P_{ssc} = \frac{4}{3} \sigma_{TC} \beta^2 \gamma^2 U_{syn} , \quad (1.10)$$

where U_{syn} is the energy density of the synchrotron photons. From Equations 1.10 and 1.8 we can see that the ratio between energy losses due to synchrotron radiation

and inverse Compton scattering is the same as the ratio of the energy densities of the magnetic field and the photons:

$$\frac{P_{syn}}{P_{ssc}} = \frac{U_B}{U_{syn}} . \quad (1.11)$$

In addition, the peak of the emission from inverse Compton interactions is related to the peak of the synchrotron emission by:

$$\nu_{ssc} \approx \frac{4}{3} \gamma^2 \nu_{syn} , \quad (1.12)$$

where ν_{ssc} is the frequency of the inverse Compton peak. The close relationship between the radiation initiated by synchrotron and inverse Compton processes is a key part of the SSC model. This class of models is able to provide good fits to the observed broad band emission, and if this scenario is valid, a close correlation between the flux at X-ray and VHE γ -ray energies should be observed.

1.2.2 Hadronic Models

An alternative scenario that has been used to explain the broadband SED of blazars involves hadronic components within the jets of the AGN. The hadronic models account for the TeV emission by π^0 or charged pion decay with subsequent synchrotron and/or Compton emission from decay products, or synchrotron radiation from ultra-relativistic hadrons [5, 67, 78]. Proton synchrotron radiation requires protons with energy above 10^{19} eV within a highly magnetized region.

The key difference between the hadronic and leptonic models is the postulated origin of the X-ray and γ -ray peaks in the SED. While the leptonic SSC models generally predict that these peaks have ties to the same population of electrons, the hadronic models attribute these peaks to two independent electron populations. This provides a critical observable differentiation between the model classes. If the emission in the X-ray and γ -ray bands is indeed related to the same electron population, some correlation should be observed as sources undergo flux variations.

1.3 Motivation and Structure

As discussed above, their high luminosity and extreme variability make blazars unique and interesting sources for studying the environment within the jets of AGN. Because the emission is Doppler boosted in intensity, nearly all the emission that we see from blazars originates within the jet. Detailed morphological studies can be made with high resolution radio observations, and precise timing measurements can be made with a number of instruments.

Due to the broad band nature of the emission from blazars, stretching over several orders of magnitude in frequency, multi-wavelength studies are essential to differentiate between the proposed emission scenarios. For TeV blazars, measurements in X-rays through TeV are very important because the low and high energy SED peaks of these sources generally reside in these two bands. The location of the peaks provide tight constraints on the emission models that attempt to explain what is observed, and observations at these energies is the focus of this dissertation.

In addition, the rapid variability that has been observed implies very compact regions for the emission and makes it important to utilize observations that are as simultaneous as possible when studying sources at many wavelengths. The variability of these sources also provides an opportunity to test for the correlations at different wavelengths predicted by some emission models. To provide the greatest dynamical range for such measurements, it is useful to attempt to observe sources as they exhibit extreme behavior (i.e., observing the source as it transitions from a quiet state to an extreme outburst).

The primary focus of this dissertation work has been to study the broadband emission of TeV blazars to attempt to gain new insight into the emission mechanism and place tighter constraints on the models used to explain this emission. This work has primarily involved observations at X-ray and VHE γ -ray energies. Chapter 2 discusses the instrumentation and techniques used in X-ray astronomy as applied to this work. Chapter 3 discusses the instrumentation used to study the sources in very

high energy (VHE) γ -rays. Finally, detailed studies of two TeV blazars, Markarian 421 and Markarian 501 are presented in Chapters 4 and 5.

2. X-ray Astronomy

Traditionally, the efforts of astronomers were linked to the portion of the electromagnetic spectrum to which human eyes are sensitive. In 1931, Karl Jansky discovered radio emission from astronomical sources while studying thunderstorms. This led to the development of radio astronomy. The visible and radio bands are easily able to penetrate the Earth's atmosphere to ground level, whereas other wavelengths are absorbed in the upper atmosphere (see Figure 2.1). The development of astronomy at other wavelengths had to wait until the space age. With the development of rocket technology, X-ray (120 eV to 120 keV) measurements were possible, first by sounding rockets sent above much of the atmosphere and later by X-ray satellites. This opened up a region of the electromagnetic spectrum that was previously inaccessible and allowed for the study and detection of many new classes of astrophysical objects. In particular, the study of the broadband emission of blazars that emit strongly in X-rays would not be possible without the development of X-ray astronomy. This chapter will discuss X-ray astronomy and describe the hardware specifications and analysis techniques used for the two observatories primarily used for this thesis research: *XMM-Newton* and *Suzaku*.

2.1 XMM-Newton

2.1.1 Instrumentation and Characteristics

At the time of its launch, XMM-Newton was the largest scientific payload launched by the European Space Agency, with a length of 10 meters to accommodate the X-ray imaging system and a total mass of 4000 kg. XMM-Newton uses a system of nested grazing incidence mirrors (see Figure 2.3), common to X-ray imaging telescopes, where

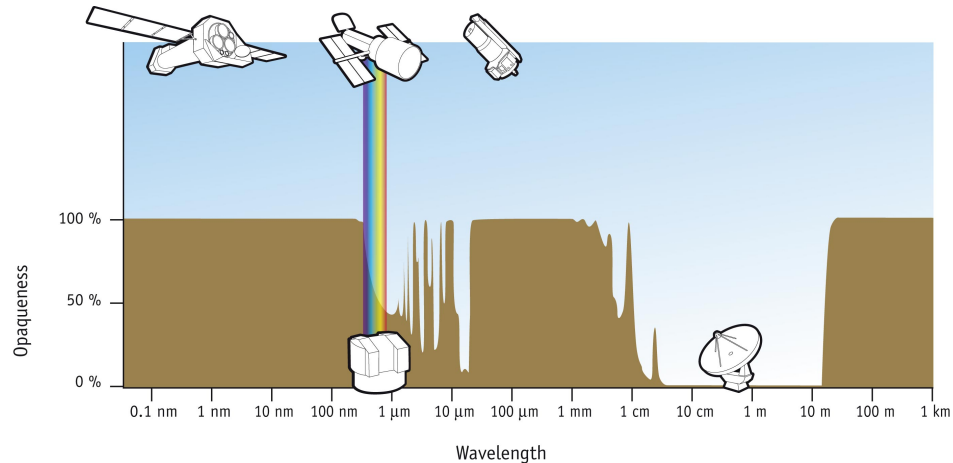


Figure 2.1. An illustration depicting the opacity of the atmosphere across the electromagnetic spectrum. Most frequencies are inaccessible from ground based observatories and must utilize space-based or other alternatives for detection. Image credit: ESA/Hubble.

the incoming X-ray photons are reflected at a very small angle of incidence (see Figure 2.4). This configuration is necessary due to the large penetration depth that X-ray photons are capable of. *XMM-Newton's* orbit is highly eccentric. Its closest approach to Earth is 7000 km while its furthest distance is 114000 km. This orbit allows for the instruments to be cooled passively, and enables long uninterrupted exposures [55].

XMM-Newton has three X-ray mirror assemblies, each focusing incoming X-rays on one of three X-ray imaging detectors, which together make up the European Photon Imaging Camera (EPIC) [90]. Two of the detectors consist of metal oxide semiconductor (MOS) CCDs that are in line with reflection grating spectrometers (RGS). The gratings deflect approximately half of the incoming X-ray flux to a separate set of CCDs which capture the diffraction patterns and provide high spectral resolution in the range from 0.33 to 2.5 keV. The remaining X-ray flux is focused on the two MOS cameras which each consist of an array of seven front illuminated CCDs. The MOS and RGS instruments were not used in this thesis work and will not be described in further detail. The remaining EPIC imaging detector is the pn CCD array (PN), which consists of 12 CCD chips arranged in three quadrants forming a single

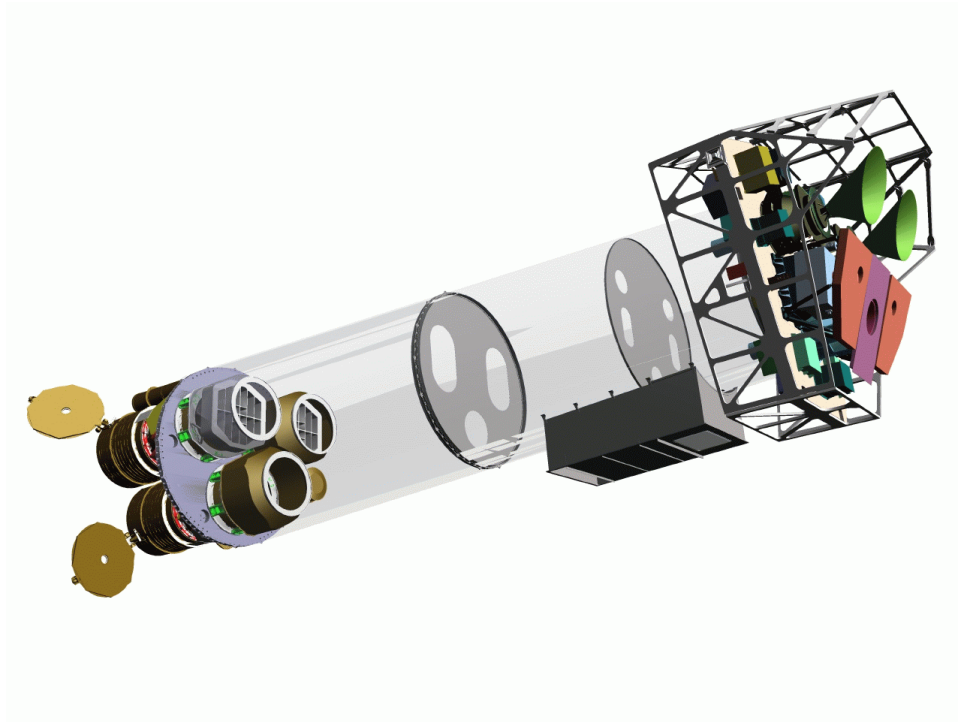


Figure 2.2. A model showing the XMM-Newton scientific instruments. Image courtesy ESA.

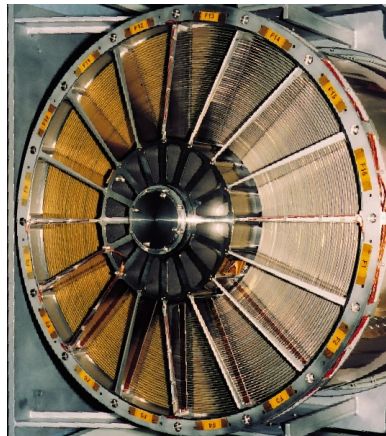


Figure 2.3. Image of one of the three X-ray telescope mirror assemblies aboard XMM-Newton. Image courtesy of ESA.

uniform surface on the focal plane (see Figure 2.5) . In addition to the X-ray imaging detectors, there is also a co-aligned UV/optical monitoring telescope (OM) on board

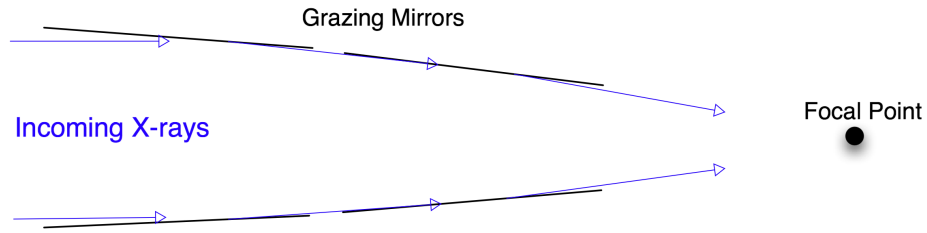
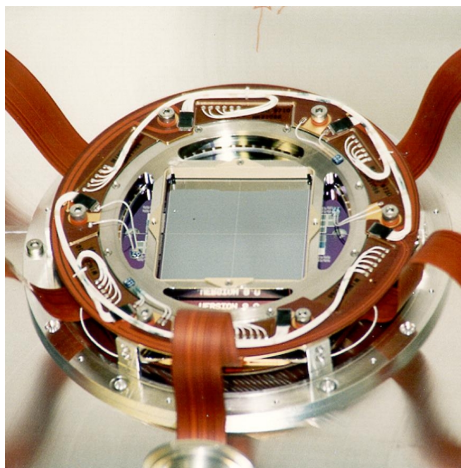
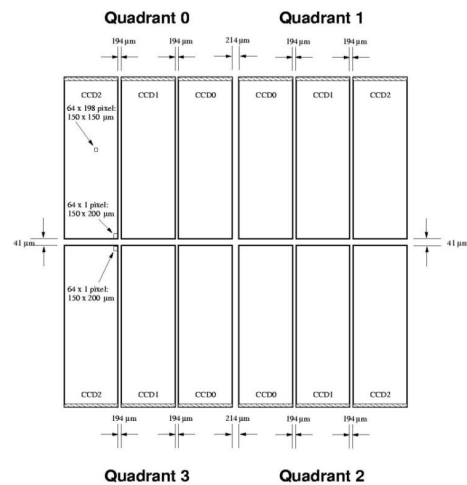


Figure 2.4. Illustration of grazing mirrors. The incoming X-ray photons are reflected off from mirrors at a very low angle of incidence.

XMM-Newton which is useful for providing simultaneous multi-wavelength data in the optical band [70]. A model showing the *XMM-Newton* scientific instruments can be seen in Figure 2.7.



(a) To provide uniform coverage over the entire field of view, multiple CCDs were fabricated on one silicon wafer. Image courtesy of ESA.



(b) An image illustrating the boundaries of the individual CCDs within the PN detector array. Image courtesy of ESA.

Figure 2.5. A preflight image (a) and schematic view (b) of the PN detector array.

Table 2.1
PN Observing Modes

PN Mode (pixels)	Time Resolution	Live time (%)	Max Rate (diffuse; s^{-1})	Max Rate (pt src; s^{-1})
Full frame (376 x 384)	73.4 ms	99.9	1000	6
Large window (198 x 384)	47.7 ms	94.9	1500	10
Small window (63 x 64)	5.7 ms	71.0	12000	100
Timing (64 x 200)	0.03 ms	99.5	<i>N/A</i>	800
Burst (64 x 180)	$7\mu s$	3.0	<i>N/A</i>	60000

2.1.2 EPIC-PN Observing Modes and Data Analysis

In the standard mode of operation, called “full frame mode,” the 12 CCDs in the array are read out sequentially. Each chip takes 4 ms to read out, for a total of 48 ms readout time. An optional mode, called “windowed mode,” reduces the readout time by only reading out a specified area of the PN array. This also reduces the time that photons can accumulate in the region to be read out, so in addition to reducing readout time and increasing time resolution, the potential for photon pile up is reduced. For even greater time resolution and reduction in photon pileup, a third mode known as “fast mode” is used. This mode has two options: timing and burst. Timing mode provides a high live time and very good time resolution. In addition, photon pile up is greatly reduced. The greatest time resolution is available in burst mode, however, the live time is greatly reduced to a duty cycle of 3%. The results used for this dissertation deal exclusively with data taken in fast timing mode.

Reprocessing Raw Data Files

All *XMM-Newton* data is available at the XMM-Newton Science Archive. Downloaded data includes the original data files (ODF), which contain uncalibrated photon files and housekeeping data. In addition, pipeline processing subsystem (PPS) files are included which consist of the calibrated data from each observation. The *XMM-*

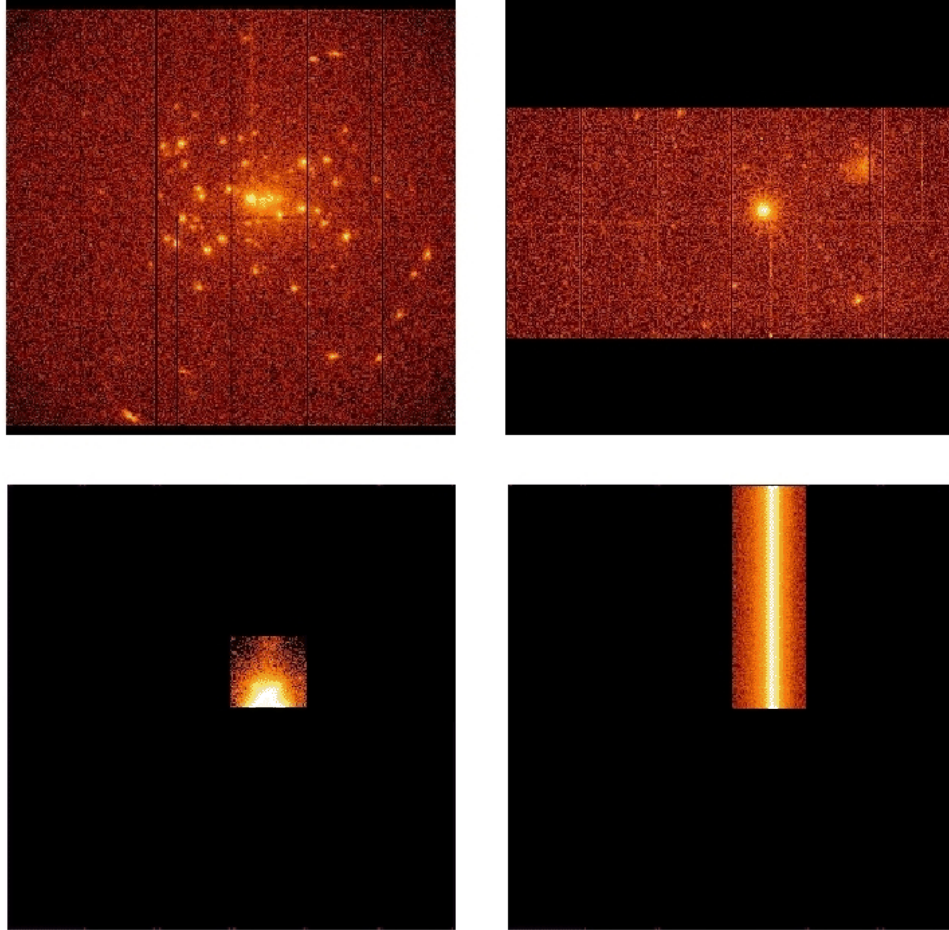


Figure 2.6. Examples of the operating modes of XMM PN. The upper left shows full frame mode and the upper right shows windowed mode with a large window. The lower left shows windowed mode with a small window, and the lower right shows an example of timing mode. Note the loss of imaging in one dimension during timing mode. Image courtesy ESA.

Newton data reduction is performed using the Science Analysis System (SAS), a package developed and maintained by the *XMM-Newton* Science Operations Center. Because SAS is under continuing development, it is generally recommended to reprocess the ODFs with the latest version of SAS and current calibration files (CCFs).

The steps for reprocessing raw data files and for further data analysis procedures are laid out in the SAS analysis threads.¹ The first task when reprocessing the ODFs is to run the SAS process *cifbuild*. This process determines which CCFs are required to calibrate a given set of ODFs and creates a corresponding CCF index file (CIF). Once a CIF has been created for an observation, the task *odfingest* is run to store the CCF file information and housekeeping data to the ODF summary file. Finally, the task *epchain* combines several calibration tasks to produce calibrated PN event files.

Event Filtering

The calibrated PN event files must be filtered based on several quality constraints depending on the specific goals of the analyst. The filtering process is performed with the *evselect* process within SAS. Once filtering criteria are selected, *evselect* is also used to extract images, light curves, and spectra from the calibrated event files. The standard filtering procedure places cuts on event patterns, quality flags that are assigned during calibration, and the energy range accepted for further analysis. Event patterns are assigned based on how many pixels are involved in an event. Single pixel events are assigned pattern 0, double events fall in pattern 1–4, and triple and quadruple pixel events are assigned pattern 5–12. For timing analysis, it is recommended to use only single and double pixel events (i.e. $PATTERN \leq 4$). The quality flag is based on several criteria, such as if a pixel involved in an event is near a bad pixel or the edge of a CCD chip. For the analysis used here, only events with the most conservative quality flag ($FLAG == 0$) are used. Finally, due to calibration uncertainties, only events with certain energies are used for further analysis. Here, the energy range used is between 0.5 and 10.0 keV. In addition, light curves above 10 keV using the full exposure area are generated to search for soft proton flaring. This contributes a significant background that can only be avoided by excluding times

¹<http://xmm.esac.esa.int/sas/current/documentation/threads/>

where the proton flaring rate is high. Good time intervals are created where the count rate in this regime is below a recommended level and used to further filter the events.

Data Product Extraction

Once a filtered event file has been created using *evselect*, an image can be created. This image is used to select source and background regions for further light curve and spectral analysis. For the timing mode data used in this dissertation, a rectangle is used for the source region, containing the columns in RAWX coordinates centered on the source and all of the active pixels in RAWY. To avoid contamination from photons originating from the source, background regions are selected far from the source location using rectangles similar to those used for the source region. Using the regions created in the extracted image, light curves and spectra can be produced using *evselect*.

RMFs and ARFs

In general, X-ray spectral analysis is performed by convolving a model spectrum with the response of the detector to attempt to match the observed data. This process allows the analyst to put constraints on the spectral model and allow the calculation of physical quantities such as fluxes and absorption columns. In order to perform this task, the response of the detector must be accurately characterized for each observation. This characterization is stored in two types of files: redistribution matrix files (RMFs) and ancillary response files (ARFs) [50].

The RMF contains a “redistribution matrix” that describes how a photon of a given energy is “redistributed” into the discrete energy channels of the detector. This file is generated by the SAS task *rmfgen*. The ARF describes the sensitivity of the detector to a photon of a given energy. This is often dependent on the geometry and physical properties of the detector as well as other properties. Essentially the ARF

provides the energy dependent effective area of the detector. The ARF is generated by the SAS task *arfgen*.

2.1.3 OM Observing Modes and Data Analysis

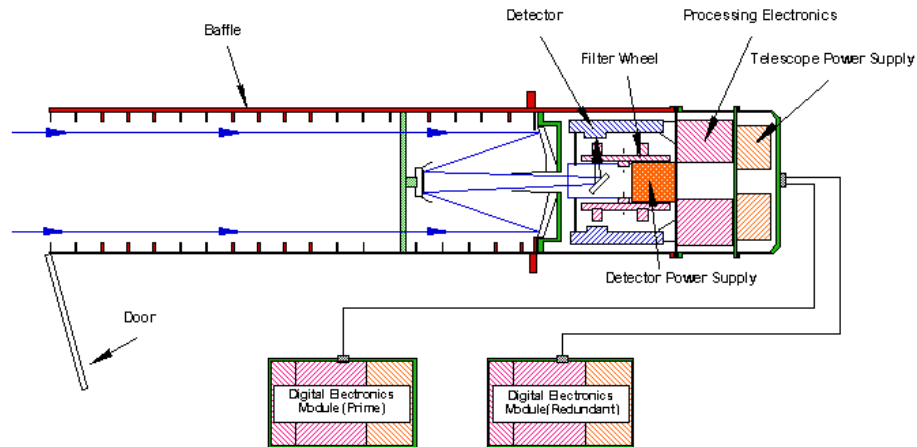


Figure 2.7. A schematic of the optical monitor aboard *XMM-Newton*. Image courtesy ESA.

The OM has three modes of operation: IMAGING, FAST, and GRISM modes. Most OM data and all of the data used in this dissertation are taken in IMAGING mode. In addition to the mode of operation, observers may choose from several filters for a given observation. There are 6 available broadband filters (UVW2, UVM2, UVW1, U, B and V), a filter that covers the entire spectral band from UVW2 through V, and an opaque filter to protect the OM in the case of a very bright source. The effective areas of the OM for the various filters is shown in Figure 2.8.

The OM data is reprocessed from the ODFs using the *omichain* analysis chain. This command calls various sub tasks to proceed through the three main parts of the analysis chain. The first task combines multiple exposures and performs a flat fielding calculation. Then, the images are processed by several tasks that apply calibration corrections. These corrections include accounting for source tracking, flat fielding

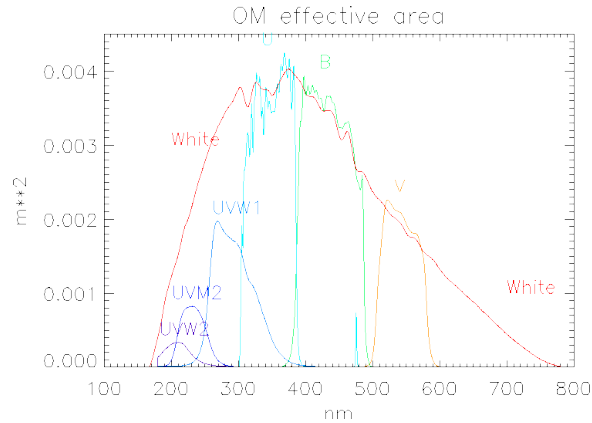


Figure 2.8. A plot of the effective areas of the OM when different filters are in operation. Image courtesy ESA.

and removing bad pixels. Astrometry and photometry calculations are made on the images, and an automatic source detection procedure is called. Finally, the source lists corresponding to different filters (if multiple filters are used) can be combined.

Further details of the analysis procedures for *XMM-Newton* PN and OM data can be found in Chapter 4. Details of the spectral fitting procedures typically used for X-ray analysis can be found in Chapters 4 and 5.

2.2 Suzaku

2.2.1 Instrumentation and Characteristics

The Suzaku X-ray observatory, formerly Astro E-2, is the latest in a series of Japanese X-ray satellites and is the product of a collaboration between institutions in the United States and Japan [74]. It is the replacement for the Astro E satellite whose launch vehicle failed, resulting in the destruction of the satellite. The spacecraft is approximately 7 m in length with a mass of 1706 kg. Five grazing incidence X-ray telescopes (XRTs), similar in design to those on board *XMM-Newton* focus incident X-rays on to *Suzaku's* focal plane instruments. Of the original three, Suzaku has two operating instruments for studying X-ray emission: the X-ray imaging spectrometer

[63, XIS] and the hard X-ray detector ([91], [61], HXD). The third instrument, the X-ray Spectrometer malfunctioned after launch and is no longer operational [57, XRS].

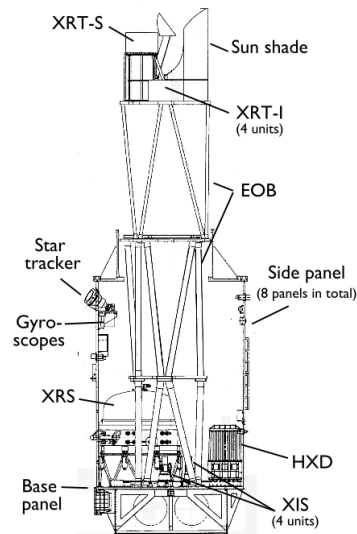


Figure 2.9. Schematic view of the Suzaku spacecraft. [74]

XIS Instrumentation

The XIS instrument consists of four X-ray telescopes with imaging CCD cameras in their focal plane. Three of the CCDs are front illuminated, and one CCD is back illuminated to provide extended sensitivity to soft X-rays (see Figure 2.11). Each camera consists of a single CCD chip with 1024×1024 pixels that view an $18' \times 18'$ window of the sky. The combined energy range of these CCDs is 0.2 - 12.0 keV.

HXD Instrumentation

The HXD is not an imaging instrument like the XIS; it is a collimated instrument that expands the energy sensitivity of Suzaku to the 10 - 600 keV band by using two types of detectors. The HXD consists of 16 “well” shaped counter units arranged in a 4×4 matrix. Each well counter consists of bismuth germanate (BGO ; $\text{Bi}_4\text{Ge}_3\text{O}_{12}$)

and gadolinium silicate [GSO; $\text{Gd}_2\text{SiO}_5(\text{Ce})$] scintillator crystals, PIN diodes, fine collimators, a photomultiplier tube, and front-end electronics (see Figure 2.10). The upper part of each unit consists of walls of BGO crystals for active collimation and passive fine collimators made of thin phosphor bronze sheets. The primary detectors are located at the base of each well in a layered structure. At the top layer are the PIN diodes, covering the energy range from 10 - 70 keV.

Above 70 keV, the PIN diodes become transparent to X-rays, allowing the radiation through to the GSO scintillators which are at the next layer. Below the GSO crystal is another block of BGO crystal for active shielding. At the base of each well, a photomultiplier tube collects the scintillation light from both the BGO and GSO crystals. BGO and GSO scintillators were chosen for the HXD due to their different rise/decay times of ~ 706 ns for BGO and ~ 122 ns for GSO. This difference allows the signals from the sensors and shielding to easily be discriminated using the signal from a single photomultiplier.

The field of view of the HXD is dependent on incident photon energy. The passive fine collimators limit the field of view below approximately 100 keV to a $34' \times 34'$ FWHM square opening. Above 100 keV, the BGO scintillators provide active collimation that defines a $4.5^\circ \times 4.5^\circ$ FWHM square opening.

The observing modes and data reduction methods for Suzaku's instruments will be discussed in the following sections.

2.2.2 XIS Observing Modes and Data Analysis

Clocking Modes

The XIS CCDs can operate in two clocking modes (normal and P-sum) that are chosen depending on the source being observed. In addition, the normal mode has a window and burst option that may be applied depending to deal with bright sources. When operating in the normal mode with no additional options, each full CCD is read out every 8 s, producing a 2-dimensional image. The P-sum mode sums a selectable

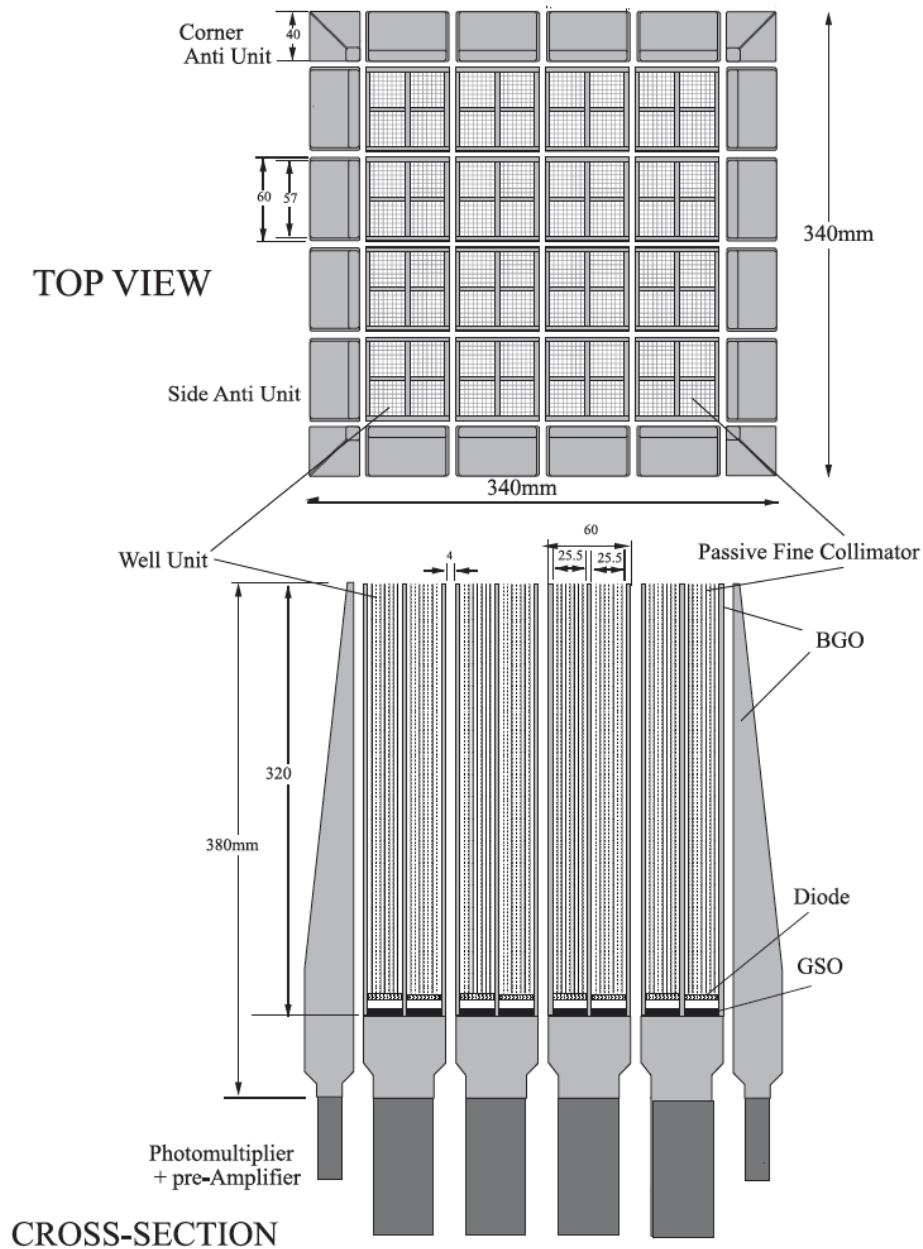


Figure 2.10. Schematic drawing of the HXD. [?]

number of CCD rows at the bottom of the image and reads out the data in a 1-dimensional manner. This increases the time resolution of the data to 7.8125 ms, and data taken in this mode usually avoids most occurrences of photon pile-up.

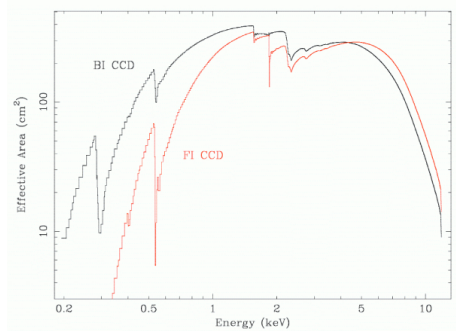


Figure 2.11. XIS effective area for a single XRT showing Image courtesy NASA.

In normal mode, photon pileup can occur for bright sources. To reduce this effect, burst and window options may be used. In burst mode, all the pixels are read out every 8 seconds but with an arbitrarily specified exposure time. This time can be chosen in steps of 1/32 seconds. This introduces a dead time consisting of the remainder of each 8 second period that is not used for exposure, but can reduce the effects of pile up. This mode is frequently used for extended bright sources because the full CCD is read out. For bright point sources, windowed options can be used to further reduce pile up. For these modes, only a specified portion, or window, of the CCD is read out. This window can be limited to 256, 128, or 64 rows of pixels (1/4, 1/8 or 1/16 window size) and can be located at a specified location on the CCD chip to capture the source. The exposure time is dependent on the size of the window used and is 2 s, 1 s, or 0.5 s for 1/4, 1/8 and 1/16 window size, respectively. If further reduction of pile up is required, the burst and window modes can be used simultaneously.

Editing Modes

XIS editing modes refer to the way in which X-ray events are sent to the Suzaku telemetry. The four available editing modes for observations are 5×5 , 3×3 , 2×2 , and timing mode (see Figure 2.12). The first three are used in normal clocking

mode, while timing mode is used in P-sum clocking mode. The editing modes can be explained as follows:

- 5×5 Mode: Pulse height information from the 25 pixels ($5 \text{ pixels} \times 5 \text{ pixels}$) around the center of the event is sent to telemetry.
- 3×3 Mode: Pulse height information from the 9 pixels ($3 \text{ pixels} \times 3 \text{ pixels}$) around the center of the event are sent to the telemetry. In addition a logical bit determined by the pulse height of the 16 pixels surrounding the 3×3 block is sent. This bit is set to true if the pulse height exceeds a threshold. The total pulse height of the pixels that do not exceed the threshold is also sent.
- 2×2 mode: Pulse heights information from a block of 4 pixels are sent to telemetry. These pixels are selected from a "cross" of 5 pixels centered on the event. The selected pixels are the event center, the second highest pulse in the cross, and the third or fourth highest pixel in the cross. In addition, a logical bit is sent indicating which of the eight adjacent pixels is above a threshold.
- Timing mode: Pulse height information and event grades are output to telemetry. Each row read out in P-sum mode is searched for events. The events are graded based on patterns and if an event is over a threshold, up to 3 adjacent pixels are summed to find the pulse height.

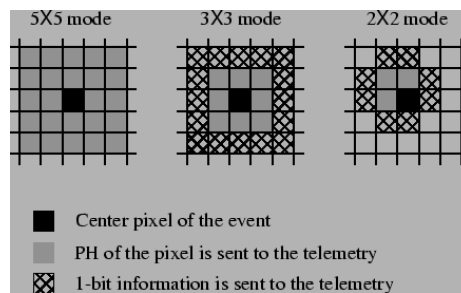


Figure 2.12. Illustration of the XIS 5×5 , 3×3 , and 2×2 editing modes. Image courtesy NASA.

XIS Initial Processing

Suzaku data is archived and accessible from the Data ARchives and Transmission System (DARTS). Downloaded data from a given observation contain unfiltered events files, cleaned events, and data output products from the analysis pipeline. The unfiltered events files are the telemetry data converted into the “Flexible Image Transport System” (FITS) format. This is a standard astronomical data format. The cleaned events have been processed through standard cuts, and are similar to the PPS data from *XMM-Newton*. Finally, the output products contain automatically generated GIF images from the data, as well as light curves and spectra. The output products are useful for a quick look at the data, but are not recommended for publication. It is recommended that analysts begin with the unfiltered events files in order to utilize the most up to date calibration and analysis tools. Data reduction and analysis for *Suzaku* is performed using the HEASoft package, a software package that includes tools for manipulating FITS files and calibration information for multiple high energy astrophysics missions.

Event Filtering

The unfiltered data can be processed through the recommended filtering criteria by accessing the housekeeping and attitude information that is contained in the “make filter file.” The standard filtering criteria make cuts on the event grade, the location of *Suzaku* in its orbit, and the relative angle between the target and the Earth’s limb. The event grades that are best calibrated and recommended for use are ASCA grades 0, 2-4, and 6 which contain mostly single and double pixel events and exclude events that are likely not triggered by X-rays. The standard filtering criteria excludes times when *Suzaku* is passing through the South Atlantic Anomaly (SAA), when high particle flux makes the data from the instruments unusable. In addition, it is recommended to exclude data until 500 s after *Suzaku* exits the SAA as the instrument background takes some time to stabilize. Finally, the filtering criteria based on the

angle between the target and the Earth's limb are included to reduce contamination from the Earth's atmosphere. The target is required to be at least 5° in elevation away from the limb at all times, and 20° away from the Earth limb if it is illuminated by daylight. These cuts reduce the effect of X-rays scattered from the Earth's atmosphere which can contaminate the data in the area of the nitrogen and oxygen lines.

Data Product Extraction

The filtered event files can now be used to generate data products using the FTOOLS package that is included in HEASoft. Similar to PN data from *XMM-Newton*, the first step is to use the FTOOL *xselect* to extract an image and select source and background regions. Again, the source region is chosen in order to include the majority of events that originated from the target, while the background region is chosen to be far from the source region. The regions that were created are then used to extract light curves and spectra from the source and background regions for further analysis. Similar to *XMM-Newton*, RMFs and ARFs are created that contain information about the instruments' response.

2.2.3 HXD Data Analysis

Event Filtering and Data Product Extraction

HXD events are filtered using similar criteria to those used for the XIS data, excluding the daytime Earth limb elevation requirement, as the scattering effects do not reach into the HXD energy range. Because the HXD consists of two types of detectors, an additional step is required to separate the data from the PIN and the GSO detectors. The task *xselect* is used to filter events based on the detector type and write the events to two new files. These files may then be analyzed for timing and spectral analysis. The following discussion pertains to HXD/PIN data analysis, the instrument used in this dissertation.

Because the HXD/PIN is a non-imaging instrument, the method for subtracting background differs from the previously discussed X-ray instrumentation. Two types of background must be accounted for: non X-ray background events (NXB) and cosmic X-ray background events (CXB). The HXD instrument team provides a NXB file containing the information necessary to subtract these events for each observation, but the CXB background must be modeled by the analyst to be taken into account. The model suggested by the HXD team is based on the results from HEAO-1, a previous high energy observatory [20]. This model is used to estimate the CXB by convolving the model with a flat response file for the PIN provided by the HXD team.

To perform timing analysis, the analyst must account for the instrument’s dead time. This is done using “pseudo” events that are generated by the HXD electronics at a regular rate. The expected rate is 4 counts/ second for these “pseudo” events. A light curve is extracted from the data containing only events that are tagged as “pseudo” events with the same temporal binning as the light curve extracted for the source. Each time bin can be corrected for dead time by the “pseudo” event rate by 4 and scaling the source light curve rate by this factor.

Spectral analysis for the PIN data is performed in XSPEC, similar to other instruments, with the exception of using the background models for NXB and CXB rather than background data extracted from regions within an image. Further details of the analysis procedures for *Suzaku* data can be found in Chapter 5. These data as well as data from *XMM-Newton* can then be combined with data from other wavelengths for detailed broadband investigations. In particular, this work has focused on combining X-ray data with VHE γ -ray data for detailed studies of TeV blazars.

3. Gamma-ray Astronomy

3.1 Imaging Atmospheric Cherenkov Technique

Above certain energies it becomes prohibitive to detect gamma-rays from space-based observatories due to the size and weight restrictions imposed by the vehicles used to launch these observatories. At higher energies, an alternative to detecting gamma rays is the imaging atmospheric Cherenkov technique (IACT). This technique indirectly detects gamma rays by looking for the interactions they undergo in the upper atmosphere.

As noted in the previous section, gamma rays are unable to penetrate to ground level for direct measurement by telescopes. However, if a photon has sufficient energy, it may be indirectly detected by observing the effects of its short lived journey through the upper atmosphere. If the photon has energy greater than $2m_e c^2$ (about 1 MeV) and passes in the field of a nucleus, pair production is possible. It is necessary for the interaction to take place in the presence of matter because both the initial energy and momentum of the photon must be conserved. The nucleus must be present to absorb some of the photons initial momentum. For gamma rays with energy $E \gg 1$ MeV, pair production can lead to electromagnetic showers in the upper atmosphere.

Electromagnetic showers may also be caused by the isotropic flux of high energy hadronic cosmic rays that also bombard the Earth's upper atmosphere. Cosmic rays interact with air molecules in the atmosphere and can also initiate electromagnetic showers similar to those from high energy photons. The characteristics of electromagnetic showers will be discussed in the next section, followed by a discussion of the Cherenkov light that they may produce and an outline of the tools necessary to detect and characterize these showers using the imaging atmospheric Cherenkov technique.

3.1.1 Electromagnetic Showers

γ -ray Initiated Electromagnetic Showers

If a photon of sufficient energy pair produces in the upper atmosphere, the resulting electron positron pair will each produce high energy photons through bremsstrahlung radiation. These photons will in turn pair produce and the process continues repeatedly, with a similar radiation length for each process. As the shower develops, the energy continues to be divided among the produced photons and particles, until the maximum amount of particles in the shower is reached when the average energy per particle drops to a point where ionization losses become more important than radiation via bremsstrahlung. As the shower develops, some transverse scattering takes place due to Coulomb interactions of the produced electron/positron pairs, resulting in a narrow band of particles surrounding the shower axis. The total number of particles in the shower, as well as the height at which the shower maximum takes place is dependent on the energy of the primary γ -ray incident on the upper atmosphere as well as the depth of the first interaction. See Figure 3.1 for a simple model of a γ -ray initiated shower.

Hadronic Electromagnetic Showers

Most of the electromagnetic showers that occur in the atmosphere are the result of the isotropic cosmic rays (hadrons) incident on the upper atmosphere. The cosmic rays produce hadronic showers through strong inelastic scattering from nuclei in the atmosphere. When these interactions occur, a shower of particles and radiation is produced similar to the γ -ray induced showers. The contents of these showers are different, however. The first interaction of the incident cosmic ray produces mostly charged and neutral pions, although kaons and other light particles may also be produced. The pions that are created decay through the following processes with lifetimes, τ :

$$\begin{aligned}\pi^+ &\rightarrow \mu^+ + \nu, \quad \tau = 2.6 \times 10^{-8} \text{ s} \\ \pi^- &\rightarrow \mu^- + \bar{\nu}, \quad \tau = 2.6 \times 10^{-8} \text{ s} \\ \pi^0 &\rightarrow \gamma + \gamma, \quad \tau = 8.4 \times 10^{-17} \text{ s}.\end{aligned}$$

About 1/3 of the pions are neutral pions (π^0) which, as shown above, decay rapidly into two photons. These photons can initiate electromagnetic showers in the same way as the γ -ray induced showers discussed above. The remaining charged pions decay mostly into muons which can in turn either penetrate to ground level or further decay into electrons and neutrinos. The pions may also interact with more nuclei within the atmosphere creating further hadronic showers within the original shower. The possible occurrence of multiple showers within the original shower, as well as the larger variety of possible shower products leads to larger transverse extension within hadronic electromagnetic showers as opposed to showers initiated by γ -ray primaries. Figure 3.2 shows a simulation of electromagnetic showers induced by γ -rays and cosmic rays.

3.1.2 Cherenkov Radiation from Electromagnetic Showers

If the initiator of an electromagnetic shower in the upper atmosphere has enough energy, the electron positron pairs created during the pair production process can travel faster than the speed of light in the atmosphere. That is,

$$v > \frac{c}{n}. \quad (3.1)$$

If this condition is met, the charged pairs will produce Cherenkov radiation. Cherenkov radiation is emitted when a charged particle travels through a dielectric medium with a speed greater than the speed of light in that medium.

When a charged particle travels through a dielectric medium, it momentarily polarizes the material nearby its path as it attracts charges within the nuclei of the dielectric material. After the particle passes, the polarization at that location is relaxed and replaced by a polarization at the particle's new location. When a particle

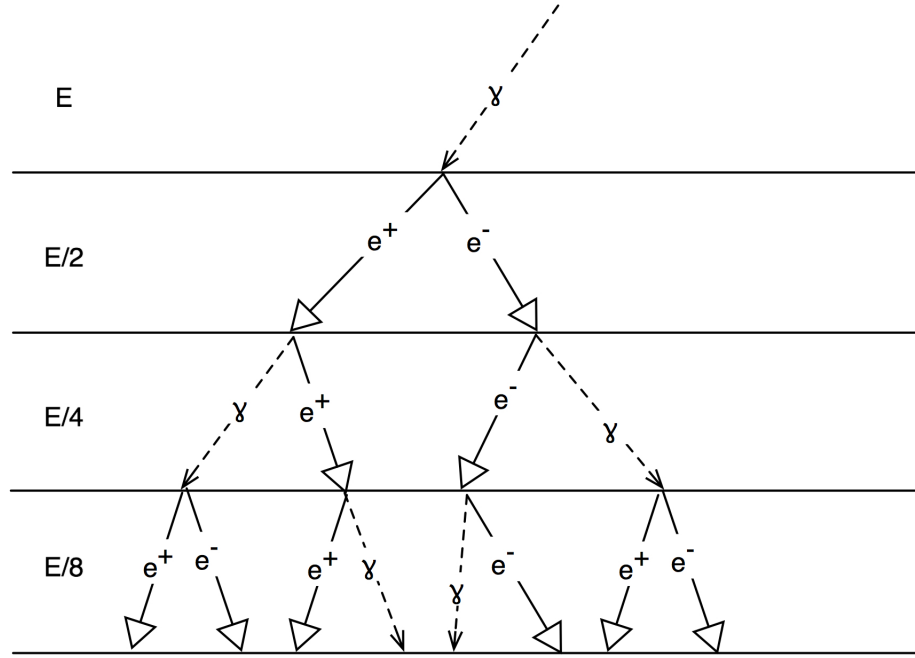


Figure 3.1. A simple model of an electromagnetic shower in the upper atmosphere initiated by a photon with energy E . The energy per particle or photon is shown for each level on the left. Adapted from [65], Figure 4.17.

travels subluminally, the polarization fields cancel resulting in no radiation. However, if the particle is traveling superluminally within the medium, the polarization fields interfere constructively and result in coherent radiation being emitted at the Cherenkov angle, θ_c , to the particle's path determined by the particle's speed and the refractive index of the dielectric medium. This relation given by:

$$\theta_c = \cos^{-1} \frac{1}{\beta n}, \quad (3.2)$$

where βc is the particle's velocity and n is the index of refraction of the dielectric medium. This has a maximum at $\beta_{max} = 1$. Using the minimum Cherenkov angle, $\theta_c = 0$, Equation 3.2 shows that the minimum velocity for a particle to emit Cherenkov radiation corresponds to $\beta_{min} = \frac{1}{n}$ for a dielectric medium with index of refraction n . This yields a minimum particle energy of:

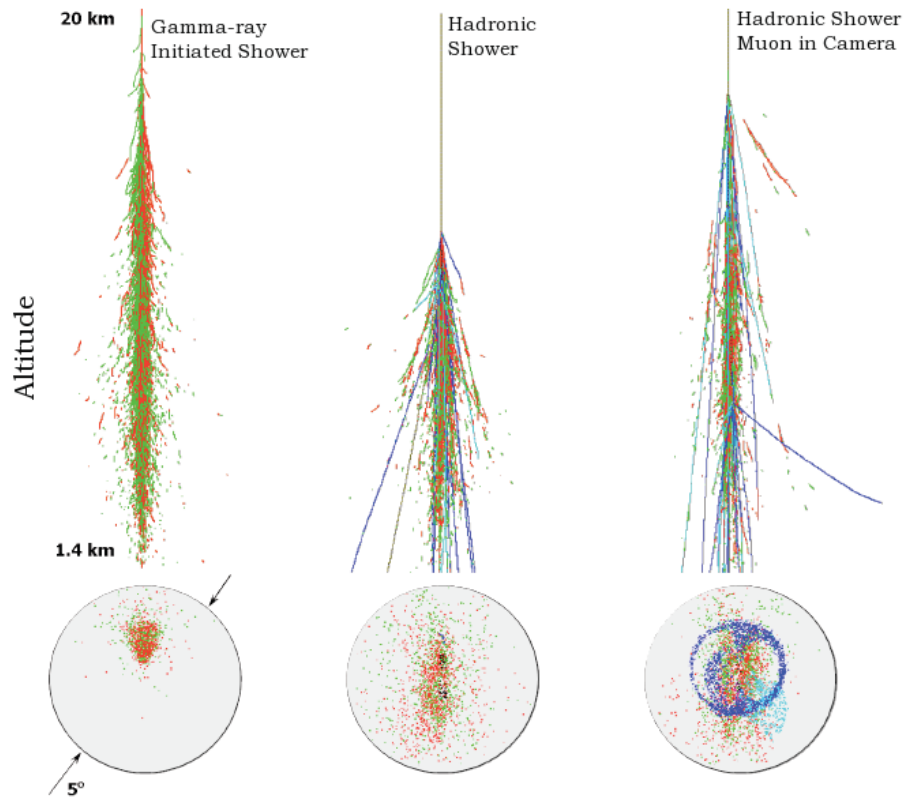


Figure 3.2. Simulations showing a air shower simulations and simulated Cherenkov telescope images for a γ -ray initiated electromagnetic shower, a hadronic shower, and a hadronic shower with a muon ring in the camera. Note the additional transverse components in the hadronic showers and the difference in images produced in the camera plane. Adapted from [73]; simulations courtesy Glenn Sembroski, Purdue University.

$$E_{min} = \frac{m_0 c^2}{\sqrt{1 - \beta_{min}^2}}, \quad (3.3)$$

for a particle of rest mass m_0 .

The index of refraction for the atmosphere (at sea level) is approximately $n = 1.0003$. This yields a minimum energy for an electron to emit Cherenkov radiation of about 21 MeV and a maximum Cherenkov angle of 1.4° . Particles interacting higher

in the atmosphere where the air is less dense and the index of refraction is lower will have a smaller maximum Cherenkov angle.

The number of photons emitted per unit path length per unit wavelength interval for Cherenkov radiation is proportional to $1/\lambda^2$ [56]. However, shorter wavelength photons are absorbed by various processes in the atmosphere, resulting in a peak of the Cherenkov spectrum at ground level in the ultra-violet and blue portions of the spectrum. The instruments designed for measuring these photons must use detectors that are sensitive in this range.

The total amount of Cherenkov light produced by an electromagnetic shower is proportional to the total number of particles in the shower. In turn, the number of particles in the shower is proportional to the initial energy of the primary particle/photon that initiated the shower, so Cherenkov light may be used to measure the initial energy of these primaries.

3.1.3 Imaging Atmospheric Cherenkov Telescopes

Imaging Cherenkov Telescopes

Knowledge of Cherenkov radiation has existed since being described by Cherenkov [31] and explained in theory by Frank and Tamm [43] in 1937. Their work led to their receiving the Nobel Prize in 1958. Cherenkov radiation from electromagnetic showers in the atmosphere was later theorized to be detectable, and in 1953, the first successful observations were taken using a PMT [48]. The first detection of an astronomical gamma-ray source did not occur until 1989. This detection was of the Crab Nebula and was carried out by the Whipple Collaboration using the imaging atmospheric Cherenkov technique (See Figure 3.3) [93]. Since this first detection in 1989, many γ -ray sources have been detected, of both galactic and extra-galactic origin. Several other experiments have adopted the imaging technique to separate the electromagnetic showers caused by incident γ -rays from those showers caused by cosmic rays.

There are a number of requirements for a good imaging atmospheric Cherenkov telescope (IACT), mostly constrained by the characteristics of the electromagnetic showers they are designed to detect. A detailed description of these requirements can be found in an early review by Weekes [94]. IACTs must first be excellent light detectors. For example, an air shower initiated by a 300 GeV γ -ray would result in a Cherenkov light flash would be distributed over an area of about 100m from the shower axis at ground level. The photon density would only be about 7 photons m^{-2} [65]. The telescopes should also be placed at high altitude to bring them closer to the location of the electromagnetic showers' maximum, where most of the Cherenkov light is produced.

As discussed in Section 3.1.2, the light from Cherenkov showers peaks in the UV and blue portion of the spectrum. Using detectors with good response in these wavelengths is therefore important to optimize the sensitivity of the IACTs. PMTs with bi-alkali photocathodes have been found to work well for this application. In addition, the imaging technique for capturing γ -ray showers also depends on the detector having good angular resolution. This can be achieved by using a large number of small diameter PMTs and packing them as close together as possible in the focal plane of the telescope, known as the camera. The camera must have a large enough field of view to capture full images of the electromagnetic showers. These showers are on the order of 1° in angular extent, placing a minimum on the size of the camera. However, showers whose axes intersect with the ground at larger distances from the telescope will be further from the center of the field of view of the camera than those near the telescope, requiring a larger field of view to fully capture the image.

In the example 300 GeV γ -ray shower discussed above, the duration of the Cherenkov light flash would only be about 2ns. Due to the short duration of the flash, the detectors used in the telescopes must have fast response times, and the telescope systems must use fast triggering systems and electronics to record the signals from the detectors. PMTs again fulfill these requirements for the detectors. In order to separate

out these quick flashes from fluctuations in the night sky background and possible signals from muons which can travel to ground level from the showers, it is useful to have multiple telescopes separated by some distance on the ground.

Calibration is also a critical component of IACTs because they use many PMTs spread across the camera plane. This provides good angular resolution, but careful calibration is necessary so that there is uniform response to the incident light across the camera plane. The total Cherenkov light of each shower measured by an IACT may be used to estimate the energy of the primary incident γ -ray, but because different PMTs measure the light from different parts of the electromagnetic shower (see Figure 3.3), they must be cross calibrated in order to make a meaningful measurement of the total shower light.

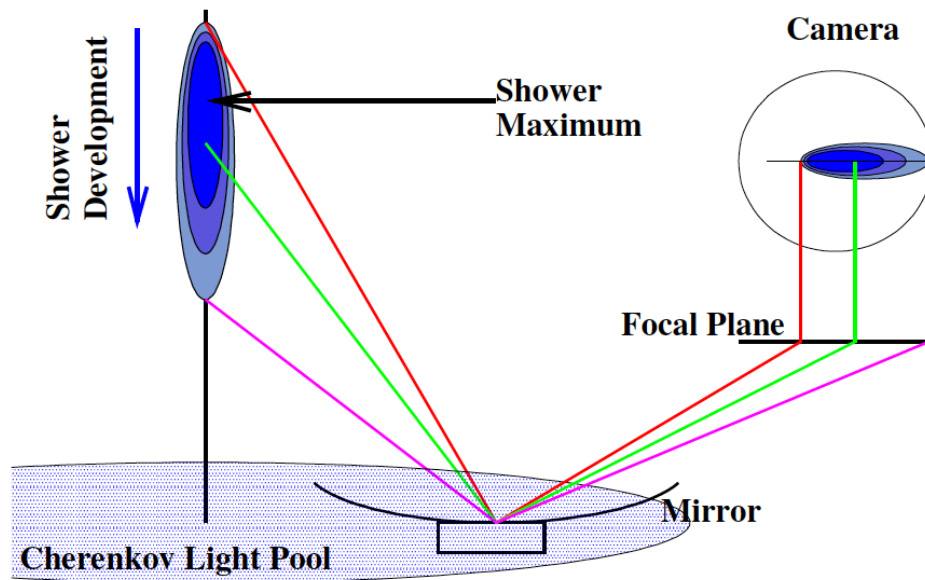


Figure 3.3. An illustration of the imaging of an electromagnetic shower in the focal plane of an imaging Cherenkov telescope that is located within the Cherenkov light pool of the electromagnetic shower. Image from [33].

The Imaging Cherenkov Technique

Once shower images have been collected and stored by the telescope systems, there still remains the difficult task of extracting γ -ray initiated showers from the large background of cosmic ray showers. This task in part is enabled by the different intrinsic structure of γ -ray and hadronic showers as discussed in Section 3.1.1. Using IACTs as described above, the Cherenkov light, emitted in a narrow cone along a shower's axis, can be imaged in the camera plane. The location where the shower axis intersects with the ground, known as the shower core, is usually large, meaning the images captured in the camera are generally elliptical in shape. A number of differences in the shapes and orientations of these ellipses can be used to help separate cosmic ray showers from γ -ray showers.

In general, γ -ray initiated showers are uniformly distributed along the shower axis and have relatively little transverse distribution. Due to this shower shape, γ -ray showers as imaged in an IACT camera generally produce narrow, symmetric ellipses. Cosmic ray showers, however, have more transverse components and may develop additional hadronic showers initiated within the original shower. These features lead images of cosmic ray showers to be less compact and less symmetric in shape than γ -ray showers (See Figure 3.2). The imaging technique exploits these differences by first fitting an ellipse to each image in the camera and then placing cuts on different parameters of these ellipses. This technique was developed by Hillas and the parameters used are commonly known as Hillas parameters [54]. The shape of each ellipse can be used to help exclude the broader, less symmetric cosmic ray showers. In addition, the semi-major axis of the ellipse fit to each imaged Cherenkov shower points in the direction of the primary particle. Because cosmic rays are isotropic in nature, while γ -rays should originate at the observed source, this can cut out additional background cosmic ray showers.

The end goal of this technique is to reconstruct the direction and energy of the primary γ -rays by examining the candidate γ -ray initiated showers remaining after

the image cuts discussed above. The incident direction of the candidate γ -ray showers can be determined from the shower orientation, while the primary's energy can be estimated by using simulations to produce tables of energy values, known as look-up tables, based on each image's size and distance parameters. For single telescope systems, the position of the incident γ -ray is not directly measured, but is estimated based on simulated γ -ray images. Stereoscopic, or multi-telescope, arrays enable the background to be further reduced by placing coincidence requirements on events occurring at multiple telescopes. In addition, the energy resolution of stereoscopic systems is improved by unambiguously determining the position of the shower core by geometric arguments. The semi-major axes of the ellipses fit in each telescope camera will point in the direction of a shower's core location. By intersecting the axes from multiple telescopes, the shower core location can be determined (See figure 3.4).

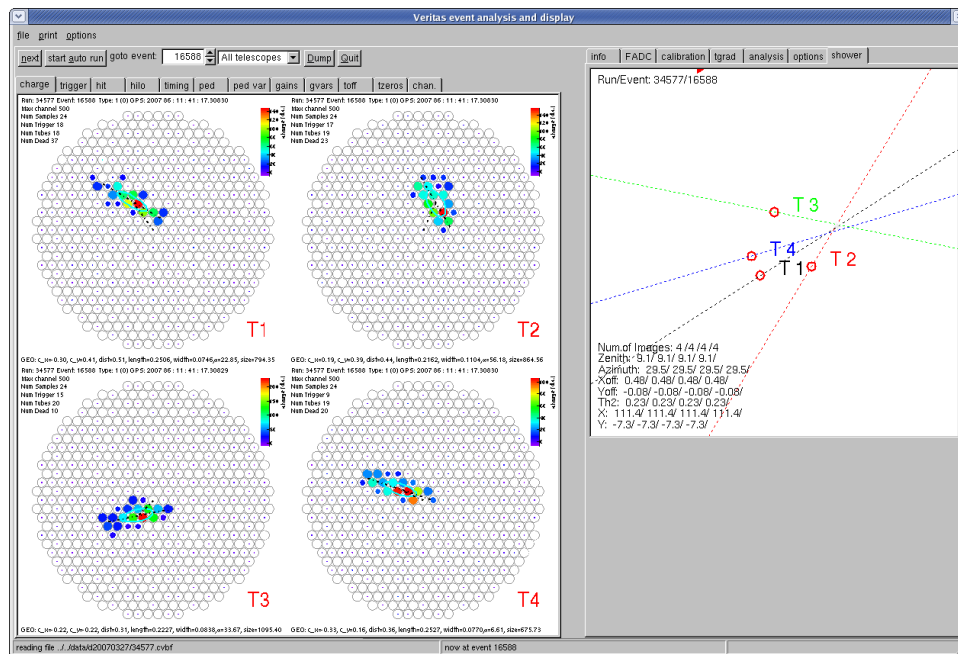


Figure 3.4. An example of a γ -ray event triggered in all four telescopes of the VERITAS array. The semi-major axes of each ellipse are extended and intersect at the shower core location. Archival VERITAS image.

3.2 VERITAS



Figure 3.5. The VERITAS experiment located at the Fred Lawrence Whipple Observatory near Tucson, AZ. Archival image courtesy the VERITAS collaboration.

3.2.1 VERITAS Hardware

Optics and Camera

VERITAS consists of four telescopes with a Davies-Cotton configuration consisting of a segmented mirror system mounted on a support structure of spherical shape with a radius of curvature of 12 m [37]. This design allows for a lighter operating weight than use of a single solid mirror as well as reduced initial and maintenance costs. Each telescope has 350 hexagonal glass mirror facets. The hexagonal shape is chosen to reduce the gaps between mirrors when mounted on the optical support structure. Each facet has spherical curvature with a radius of 24 m. The facets are coated on their front surfaces with a reflective aluminum coating at an on-site mirror facility. In addition, the mirror surfaces are anodized to increase the lifetime of the mirrors as they are continuously exposed to environmental effects at the observatory site. The reflectivity of the mirrors is optimized to match the wavelengths of Cherenkov light typically produced in electromagnetic showers. A detailed description of the VERITAS mirrors can be found in [84].

The mirrors are fastened to the optical support structure via mirror mounts that allow for adjustment of each facet to optimize alignment. When optimally aligned, the facets should function as a single spherical mirror with a radius of curvature of 12 m. It is also important to reduce the point spread function of the optical system in order to form good images of the Cherenkov light from electromagnetic showers. Ideally, the light from a point source should be contained within a single pixel on the VERITAS camera. The alignment of the individual mirrors is an important factor that effects the point spread function of each telescope. To optimize the alignment of the VERITAS mirrors, a system was developed using raster scans across a bright point source to check each mirror facet for misalignment [72]. Using this method, the telescope scans across the location of a bright star which can be considered a point source at infinite distance. A CCD camera placed at the focal plane measures the light from each individual facet during the scan, providing a measurement of the misalignment angle for each facet. This misalignment can then be removed by adjusting the mounting screws on the individual facets. In addition, the optical support structure flexes differently at different elevations, so the alignment measurements are taken at typical observation elevations to minimize this effect on misalignment.

The VERITAS cameras are located at the end of four steel support beams at the focal point 12 m from the mirror surfaces (see Figure 3.6). Each camera consists of 499 PMTs tightly packed and covering a field of view of 3.5° (See Figure 3.8(a)). To reduce the light lost between PMTs, a set of reflective “light cones” are placed directly in front of the PMTs. The light cones are essentially reflective wells over each PMT that work to funnel the light that would have passed between them onto the face of a PMT (See Figure 3.8(b)). In addition, the light cones reduce the viewing angle of each PMT to cover only the mirrors of each telescope, reducing the detection of light from other angles.

The primary detectors used for VERITAS are PMTs. They provide a fast response time and high gain for detecting the brief, faint flashes of Cherenkov light emitted by electromagnetic showers. The PMTs used for VERITAS are Photonis

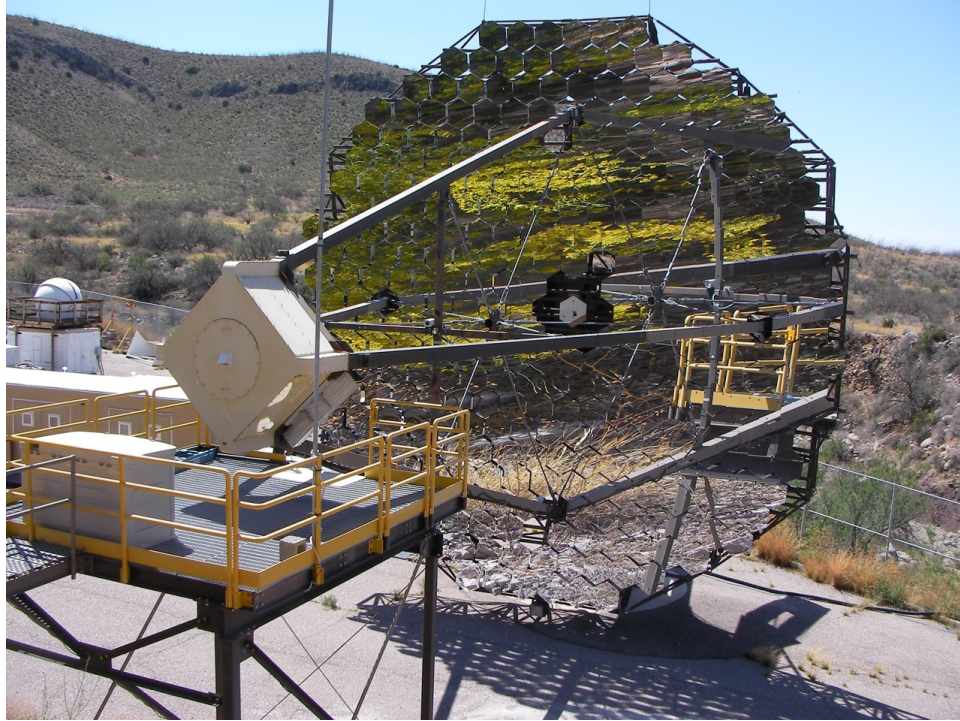


Figure 3.6. An image of VERITAS telescope 1 showing the 12 m optical support structure with 350 mirror facets and the camera box at the 12m focal point of the optics. (As of the time of writing, telescope 1 has been moved from the location pictured here to a location providing more uniform separation between the telescopes in the array.)

model XP2970/02. These phototubes are 28mm in diameter, use bi-alkali photocathodes and have 10 stages of dynodes. The size of the tubes allows for arrangement in the camera plane with an angular distance of 0.15° between PMT centers.

An important characteristic of the PMTs to be used is the quantum efficiency, or the probability that a photo-electron will be released if the photo-cathode is struck by a photon. It is important for VERITAS to have PMTs with high quantum efficiency peaking near the characteristic wavelength of Cherenkov radiation. Typical quantum efficiencies for VERITAS PMTs are currently near 25% in this important region. A plot showing the dependence of quantum efficiency on wavelength is shown in Figure

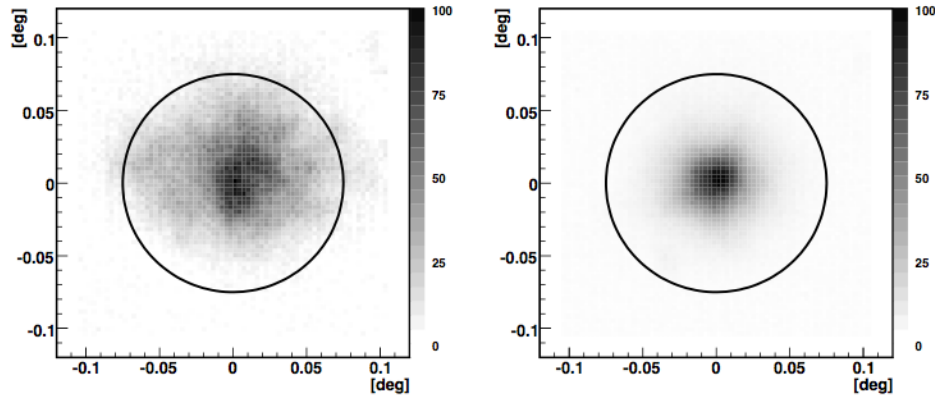
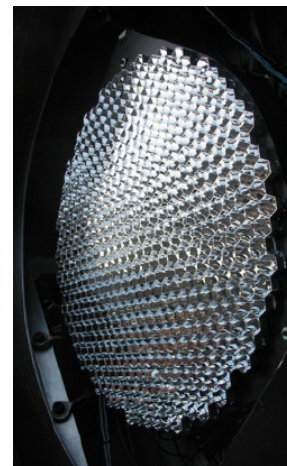


Figure 3.7. The PSF of a VERITAS telescope before (left) and after (right) mirror alignment. The circle indicates the size of a PMT. Plot taken from [72].



(a)



(b)

Figure 3.8. Images of a VERITAS camera without the light cones mounted (a) and the light cones that are mounted to the front of the camera to reduce light lost between pixels and light not coming from the mirrors (b). Archival images courtesy of the VERITAS collaboration.

3.12. The gain of a PMT is the ratio of the anode current from a cathode photocurrent to the photocurrent at the cathode:

$$gain = \frac{I_{anode}}{I_{photo}} . \quad (3.4)$$

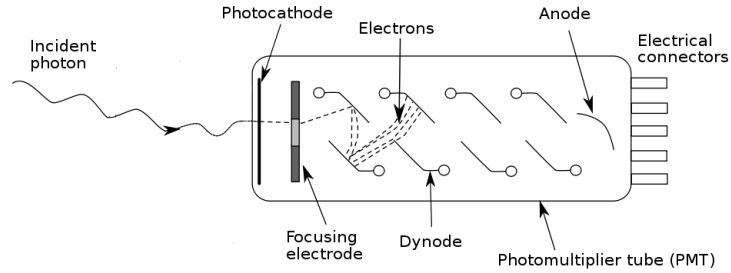


Figure 3.9. A schematic diagram of a typical PMT.

VERITAS operates with a nominal gain of 2×10^5 .

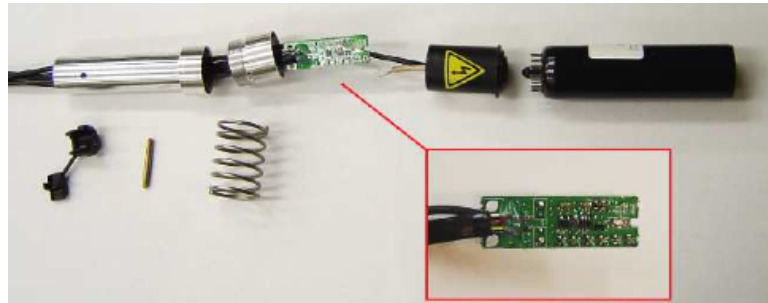


Figure 3.10. An image of a pixel from the VERITAS camera before assembly. The inset shows a close up of the preamplifier board. Image from [76].

Preamplifiers

Even with the large gain at the PMTs, the signal output of each PMT is still very weak. In addition, the signals from each PMT must travel through 50m of coaxial cable to reach the data acquisition and trigger electronics. These electronics systems are located in the electronics trailers adjacent to each telescope. In order to improve the signal to noise ratio at the trigger electronics, the output of each PMT is amplified before traveling through the signal cables. This is performed with custom built preamplifier boards located at each pixel. The preamplifiers have a bandwidth

of 300 MHz, allowing the preservation of pulse shapes from the fast Cherenkov light flashes which have typical pulse rise times of 2.5 ns. The preamplifiers operate with a gain factor of 6.6 which, combined with the gain from the PMTs, results in a 2.4 mV pulse height for a single photoelectron at the data acquisition and trigger electronics [76].

At the preamplifiers, the signals from the PMTs are AC coupled to remove the steady bias current that is primarily caused by the night sky brightness. At the data acquisition electronics, a “pedestal” current is added to the signal to allow any negative fluctuations from the night sky background to be measured. In addition, the preamplifiers provide a direct DC measurement of the currents in the PMTs to the current monitoring system discussed below.

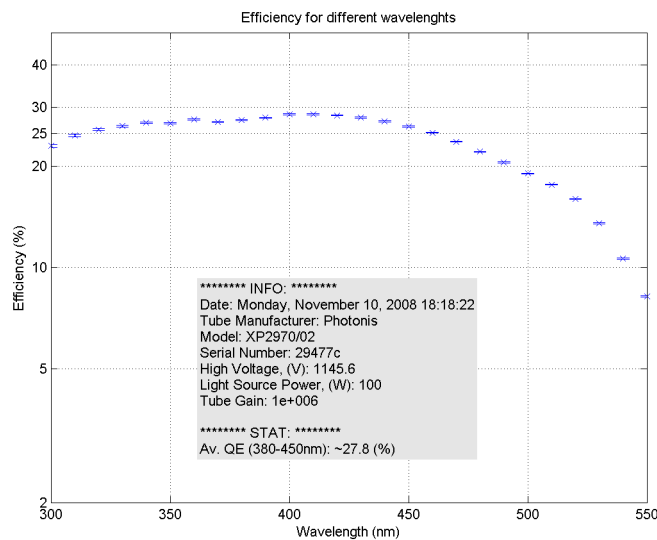


Figure 3.11. A plot quantum efficiency of a Photonis PMT over several wavelengths. Image Credit: Ben Zitzer.

High Voltage and Current Monitoring System

The PMTs require a stable high voltage to operate properly. To provide this, a multi-channel commercial power supply system manufactured by CAEN is used.

This system allows for the voltage at each PMT to be individually adjusted with 1 volt precision. The voltages must be adjusted at each PMT to provide approximately equivalent gains across the camera. This also allows suppression of PMTs if unusually high currents are detected.

The power supply system is controlled through a program that allows for automatic and manual manipulation of the high voltages in each camera. The program reads voltage settings for all pixels of all cameras from the VERITAS database at start up. These voltages are optimized to flat-field the cameras and are adjusted periodically using laser calibration data.

The lifetime of a PMT is determined among other factors by the amount of current that passes through it. An abnormally large amount of current passing through a PMT in a short amount of time can also cause permanent damage. During an observing session, if the current in a PMT passes certain limits, the voltage will be lowered (suppressed) in that PMT to avoid damage. High currents due to bright stars in the field of view occur frequently. If unusually high currents are detected in several PMTs across a camera, the high voltage control program automatically reduces the voltage for the entire camera. This protects the cameras from bright light directed at the cameras from passing cars or other sources. Individual pixels can also be manually suppressed by observers. The high voltage program records the anode currents and high voltage values for each pixel to the VERITAS database for use in offline analysis.

The PMT anode currents are measured and provided to the high voltage control program by a separate program known as the current monitor. This program communicates with a custom electronics system in the camera that reads the DC anode currents provided by the preamplifiers as well as data from environmental sensors which measure temperature and humidity in the camera box. These data are used to allow for automatic and manual safety precautions to be taken. The DC current data is provided to the high voltage software, and pixels with currents over a preset limit currents are automatically suppressed. The environmental data is passed on to

programs that are monitored by the observers to ensure that the operating conditions are safe for the camera electronics.

Trigger system

In designing a trigger system for IACTs it is important to optimize both the time that the array is able to take data and the low energy sensitivity of the array. Reading out an array event takes a finite amount of time, during which new events cannot be recorded, resulting in dead-time. A trigger system must be able to improve the efficiency of the array by rejecting events that are the result of night sky background fluctuations and muons impacting near the telescopes. In addition, the trigger system should allow the array to operate with as low an energy threshold as is possible, without being overwhelmed by triggers from night sky fluctuations. The trigger system developed for VERITAS relies on three levels of trigger criteria to attempt to optimize the event readout process.

Level 1 Trigger: The level 1 (L1) trigger operates on the level of individual pixels within each camera. The signals from the PMTs are passed through constant fraction discriminators (CFDs) with programmable thresholds. CFDs are used rather than simple threshold discriminators to provide uniform timing information in the signals from the PMTs which is essential for the coincidence requirements applied later in the trigger system. Simple threshold discriminators suffer from a phenomenon known as “slew time” or “walk” where pulses of different amplitude will result in triggers with different timing. The CFDs were designed specifically for the VERITAS system and are described in detail in [53].

In summary, the amplified signals from each PMT are split into three paths. The first component passes through a programmable threshold discriminator (TD). This generates a signal if the input signal exceeds the threshold. The remaining two components are passed through a zero crossing discriminator (ZCD) with one component inverted and delayed and the other component attenuated. The ZCD selects the time

where the sum of these two components reaches zero, which is independent of the amplitude of the individual pulse. This time is the CFD trigger time. An additional circuit, the rate feedback loop, helps to reduce timing jitter by adding a rate dependent DC offset to the ZCD. The outputs of the ZCD and the TD are passed through a flip-flop which then sends the full CFD trigger on to the level 2 trigger. The VERITAS CFDs are nominally operated with a trigger threshold of 50 mV and an output signal width of 10-12 ns.

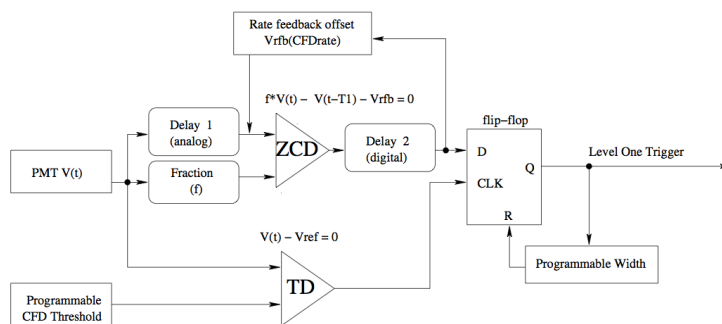


Figure 3.12. A block diagram of the CFDs used for the VERITAS Level 1 trigger. Image taken from [53].

Level 2 Trigger: The level 2 (L2) trigger operates on the camera level at each telescope. It acts as a pattern selection trigger (PST) that looks for programmable patterns in the L1 triggers that are compatible with γ -ray like events [24]. Currently the system uses the criteria of three adjacent pixels with L1 triggers within a coincidence interval of 10-12 ns. This triggering criteria helps to eliminate triggers from night sky noise and after-pulsing of PMTs which should be randomly oriented in the camera.

The PST takes as input L1 CFD signals from each pixel (excluding some outer pixels) and groups them into 19 overlapping regions of 59 pixels. If the L1 trigger signals match both the multiplicity and coincidence requirements described above, the

patterns of the triggered pixels are captured and sent to pattern selection modules for analysis. 19 pattern selection modules with programmable pixel pattern look up tables are used to analyze each of the 19 regions. If a pattern is found that matches a pattern in memory, a telescope level (L2) trigger is sent to the level 3 trigger.

Level 3 Trigger: The level 3 (L3) trigger operates on the array level and uses multiplicity and coincidence requirements to select L2 triggers that are compatible with a simultaneous observation of a γ -ray like electromagnetic shower by a programmable number of telescopes in the array. Most background events due to night sky fluctuations are removed by the first two trigger levels, but background events due to muons that reach ground level can only be removed by requiring an event to have been observed by multiple telescopes. The Cherenkov light from a muon traveling to ground level will rarely trigger two telescopes due to their physical separation, so the L3 trigger requirement will essentially remove muon events that pass the L1 and L2 triggers.

Because the primary function of the L3 trigger involves multiple telescope coincidences, programmable from 10 – 250 nanoseconds, the L2 signals must be managed in a way that preserves the timing information of each trigger signal. The L3 trigger system is centrally located and receives the L2 signals from each telescope via a fiber optic link using digital asynchronous transceivers (DATs) which can transmit and receive the trigger pulses, event numbers, and event type flags asynchronously on 11 channels with nanosecond accuracy with no addition of dead-time to the system.

For the L3 trigger system to determine relative timing of events at each telescope, delays must be accounted for in the L2 triggers from each telescope. These delays arise from two primary factors: different signal cable lengths between each telescope and the central L3 system and relative delays in arrival time of the Cherenkov light at each telescope due to the pointing and physical location of the telescopes. The relative delay due to cable length is constant, but the delay due to shower arrival time is dependent on the pointing of the telescopes. To correct the variable delay,

the telescope pointing information (stored to the VERITAS database by the tracking system) for each telescope is updated every 5 seconds and used to calculate the delay. Once all relative delays are accounted for, events that fall within the programmable coincidence window with the required number of telescopes are triggered as L3 events, and a logic pulse from the L3 system is sent to the data acquisition system, discussed below.

Data Acquisition System

The VERITAS data acquisition system consists of 3 levels of hardware and software systems that merge information from the individual pixels into telescope level events and finally into array level event data that is stored to an archive system. During observing, the signals from the PMTs are input directly into FADC boards in each telescope's electronics trailer. Here, the signals are split, with one branch sent to the L1 trigger system and the other the other branch passing through the FADCs to be digitized. The signals are converted to FADC traces which are stored in a memory buffer with a capacity of 32 μ s. When an L3 trigger signal is received, the FADCs stop recording events and read out a preset portion of the buffer, determined by the delay of the L3 signal from the L2 trigger at each telescope. This portion of the buffer contains the information from the event that initiated the trigger.

The acquisition of the FADC traces is managed by a VME data acquisition system (VDAQ). During data read-out, the VME crates that manage the FADCs send a BUSY flag that prevents further L3 triggers until the event is read out. The clocking for event readout is managed by clock trigger boards (CTB) on each of four VME crates that manage the FADCs and a master CTB and a GPS clock that are handled by an auxiliary crate. This allows synchronization of the time stamps on events over the entire system. In addition, the VDAQ receives and records a unique event number for each event and the type of trigger. All of this information is passed along in the form of event fragments to the next level of data acquisition.

The event fragments are passed from VDAQ to the event builder, a program that combines the fragments into telescope level events. Event builder is a software level data acquisition program. The input VDAQ event fragments are parsed to find event fragments with matching unique event numbers. After all the fragments with a given unique event number are gathered and stored in memory, the event builder combines them into a single telescope level event. These events are then written to a local disk and also sent to the next data acquisition level, the harvester.

The harvester gathers the individual telescope level events and combines them with information from the L3 trigger to form array level events. The array level events are stored in a custom binary format known as VERITAS bank format (VBF). After the completion of a data run, all information is stored in a VBF, compressed, and transferred to both local and remote archive systems for subsequent analysis.

VERITAS Observers interact with the data acquisition and trigger systems through a graphical interface on a central control computer known as “array control.” This system allows observers to easily start, initialize and stop all levels of the VERITAS trigger and DAQ systems. The observers set the observation target, observing mode, and data run parameters through array control, and the system communicates with L3, event builder and harvester to initiate and terminate individual data runs throughout an observing session. Array control also provides real time diagnostic information to the observers so they can monitor the quality of the data being taken.

3.2.2 VERITAS Data Analysis

Data Storage

Data from VERITAS is stored in a proprietary data format known as VERITAS bank format (VBF). These data files contain the information stored for each event recorded by the array including the trigger information. The data files are then archived remotely for access by members of the VERITAS collaboration for analysis.

Calibration Calculations - “VEGAS Stage 1”

The first step of analyzing VERITAS data is to remove all hardware dependencies from the measured values. These hardware dependencies include the gain of individual PMTs, different travel time for signals from each PMT to reach the FADCs, and night sky background (NSB) fluctuations that may differ at each pixel. The first step is to calculate several calibration parameters that are discussed below. In addition to these calibration calculations, information about the status of the array during observations is read from the database during the first stage of analysis. This information includes the telescope pointings, data run type, pixel status, weather and other important information. This information is stored resulting data file for use by later stages.

Pedestal Calculations: The main source of noise in the PMTs when Cherenkov light is not present is fluctuations in the night sky background. The NSB produces a current through the PMTs with positive and negative fluctuations. These fluctuations are summed in the FADC traces, making it important to measure the fluctuations that occur for each run in order to correctly measure the charge deposited and the significance of this above the NSB.

However, the output from the PMTs is AC coupled, meaning no positive voltage fluctuations can be digitized. In order to make a measurement of all fluctuations, an artificial injected value, corresponding to approximately 16 digital counts, is added to the PMT output allowing for fluctuations above and below the AC coupled mean to be measured. This offset is known as the “pedestal,” and fluctuations about its value will be due to the NSB.

In order to analyze the data and extract the value and significance of the charge deposited due only to Cherenkov light, the pedestal values for each pixel (“mean pedestal”) and a measure of the fluctuations in these values (“pedvars”) must be determined. To measure the mean pedestal and the pedvars, the telescopes are artificially triggered at a regular rate of 1 - 3 Hz during data taking to measure the brightness of each pixel in the absence of Cherenkov light. During the calibration

calculation stage of analysis, the FADC traces from pedestal events during each data run are used to calculate the mean charge at each pixel due to the pedestal. The pedvar of a pixel is the width of the distribution of pedestal measurements for that pixel. For an example of typical pedestal and pedvar values, see Figure 3.13.

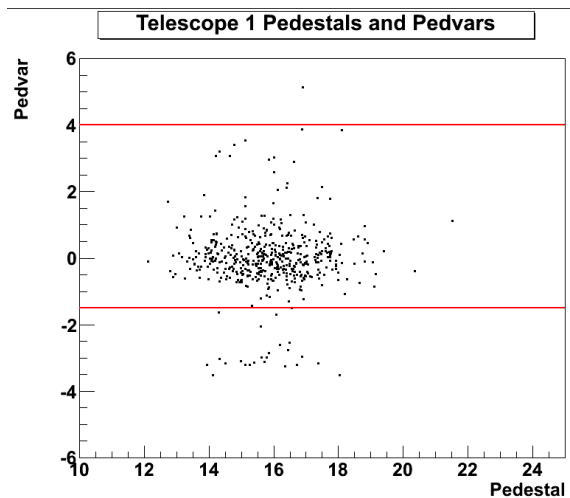


Figure 3.13. A plot of the mean pedestal value vs. the pedvars for a single telescope.

FADC Timing Calibration: The arrival times of signals detected by the PMTs and measured by the FADC traces are another critical calibration component. The arrival time of signals from each PMT (even if every PMT is simultaneously illuminated) will differ from pixel to pixel depending on time delay in the signal cables, high voltage settings, and electronic delays within the FADCs. The arrival time differences that are due to hardware, known as T_{offset} , can be removed by using the laser runs taken each night. The laser run illuminates every pixel in the camera uniformly and at a set rate.

The arrival time of a signal at each pixel is known as T_{zero} . T_{event} is defined as the average T_{zero} of each pixel in a camera:

$$T_{event} = \frac{1}{n} \sum_{i=1}^n (T_{zero})_i , \quad (3.5)$$

where n is the number of pixels in the camera and $(T_{zero})_i$ the arrival time for each pixel.

T_{offset} is calculated for each pixel using the average difference between T_{zero} and T_{event} for a large number of events. So, for each pixel:

$$T_{offset} = \frac{1}{m} \sum_{i=1}^m (T_{zero} - T_{event}) , \quad (3.6)$$

where m is the number of events used for the calculation. The T_{offset} values for each pixel are calculated each night from the laser run and are later subtracted from the arrival times of the data to obtain the actual arrival time of Cherenkov light. Figure 3.14 shows a distribution of T_{offset} values for each pixel in a single telescope.

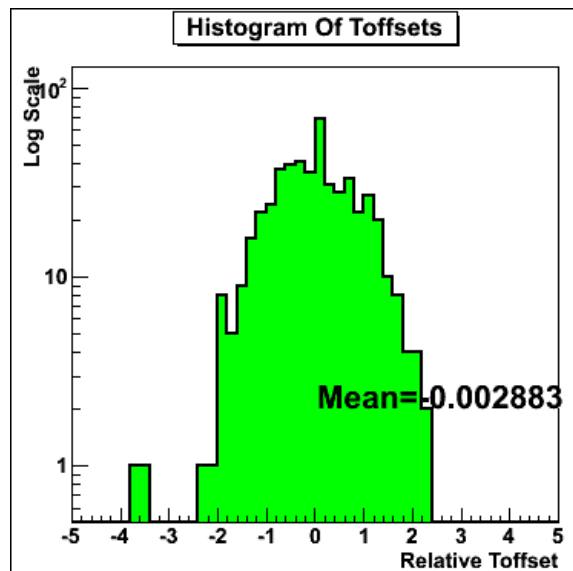


Figure 3.14. A plot of the distribution of T_{offset} values for all the pixels in a single telescope. The y-axis shows the log of the number of pixels and the x-axis shows the T_{offset} value in ns.

Relative Gain Calculation: One critical requirement of the imaging Cherenkov technique is to make a calibrated measurement of the number of Cherenkov photons in an electromagnetic shower. This value is proportional to the energy of the primary initiator of the shower. In an ideal system, the amount of charge measured by the

FADCs would be proportional to the number of photons detected at each pixel. Ideally the response of each pixel to a given number of photons would be uniform across the camera. However, due to difference at each PMT, relative gain must be taken into account to provide a calibrated measurement.

Each observing season, the voltages for each PMT are adjusted to attempt to reach the same response for each pixel for the same number of incident photons. There are variations in these values on a night-to-night basis, however, so it is necessary to take nightly measurements to adjust the relative gains and flat field the camera. This process again uses the laser runs taken each night where each pixel is illuminated by an equal amount of light.

The relative gain for an individual channel is calculated in a similar way as the T_{offset} value discussed above. First the average charge for an event across all pixels in the camera is calculated. Then the ratio of the charge in each pixel to the average is calculated. The average of this ratio for each pixel over many events give the relative gain for that pixel. Figure 3.15 shows a distribution of relative gain values for a single telescope. The distribution is centered around 1, meaning that the average charge for each pixel is close to the average charge per pixel over the entire camera. The narrower the distribution, the more uniform the gain calibration is for the camera.

Pixel Status Determination The next calibration task is to remove those pixels that have been determined to be "bad." These bad pixels may be the result of malfunctioning PMTs or pixels that are turned off. Also, during the course of a run, the high voltage may be automatically suppressed for pixels due to bright stars in the field of view. These bad pixels must be removed before image parameterization. The VERITAS database is accessed to check for pixel information and the signals from each PMT are analyzed to search for characteristics of bad pixels as discussed below.

The high voltage system stores the voltage values for each pixel during the course of a run to the database for later access. During analysis these values are read out to determine which pixels are off or suppressed during a run. To check for other pixels

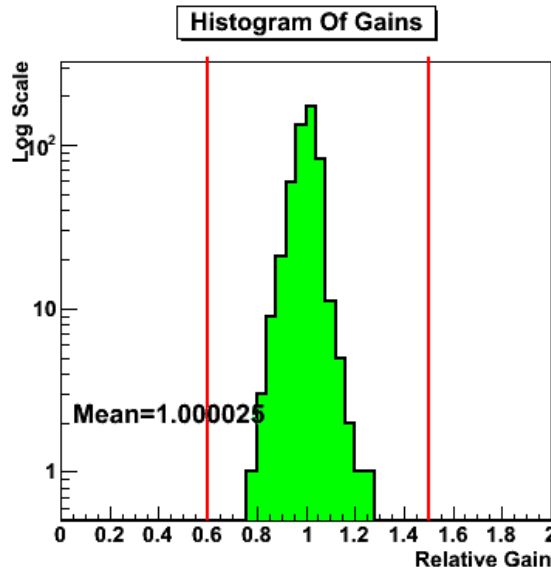


Figure 3.15. A plot of the distribution of relative gain values for all the pixels in a single telescope. The y-axis shows the log of the number of pixels and the x-axis shows the relative gain value.

that may not be reported by the database, the pedvars of each pixel are analyzed for behavior characteristic of bad pixels. A pixel with a pedvar close to zero could be the result of a malfunctioning PMT or the high voltage being turned off. Alternatively, a pixel with a much larger than average pedvar is noisy and may be the result of a PMT malfunctioning or the high voltage system not automatically suppressing a pixel with a star in the field of view. To identify pixels that may meet either of these criteria, a new quantity, the "relative pedvar" is calculated. This is defined for each pixel in the camera as:

$$Relative\ pedvar = \frac{pedvar - pedvar_{avg}}{\sigma_{pedvar}}, \quad (3.7)$$

where $pedvar_{avg}$ is the average pedvar for the camera. This value is used to allow for cuts to be made on the pedvars independent of the slight offsets that may exist in each camera. Figure 3.16 shows a distribution of relative pedvars for a single telescope. The pixels outside of the cuts indicated by the red vertical lines are removed from further analysis.

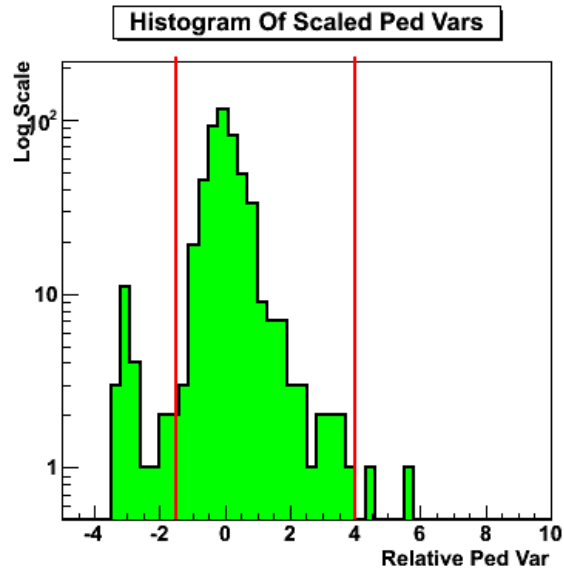


Figure 3.16. A plot of the distribution of relative pedvars for all the pixels in a single telescope. The y-axis shows the log of the number of pixels and the x-axis shows the relative pedvar value. The window of allowed relative pedvar values from -1.5 to 4 is shown.

Calibration Application and Image Parameterization - “VEGAS Stage 2”

The calibration calculations made using each data run and the laser run of the night during the first stage of analysis are stored and passed on for the next stage of analysis. In this stage, the calibration parameters are applied to the raw data to remove (as much as possible) hardware dependence for further analysis. In addition, parameterization of the shower images is performed at this stage and passed on to the later stages of analysis.

Image Cleaning: Once the calibration is applied to the FADC trace data, pixels that are likely to be part of an image of Cherenkov light are located through a procedure known as image cleaning. In this process, pixels with an integrated charge from the FADC traces greater than 5 times the pedvar value for that pixel are identified as “Picture Pixels.” In addition, “Boundary Pixels” are selected as those pixels adjacent to an Picture Pixel having an integrated charge greater than 2.5 times their

pedvar value. Pixels identified as Picture Pixels but having no adjacent Boundary Pixels or Picture Pixels are removed as they are likely the result of noise. After this selection, only data from Picture and Boundary pixels are kept and identified as images of Cherenkov light.

Image Parameterization: Once cleaned Cherenkov images are identified, they are parameterized using methods suggested by Hillas [54]. The first and second order moments for each image are calculated using the coordinates of each pixel relative to the center of the field of view and the signal in each pixel. The image centroid can be found using the first order moments, and the second order moments may be used to find the width and length parameters. These parameters and others are described in Table 3.1 and illustrated in Figure 3.17. A full description of the moment fitting procedure can be found in the appendix of [82].

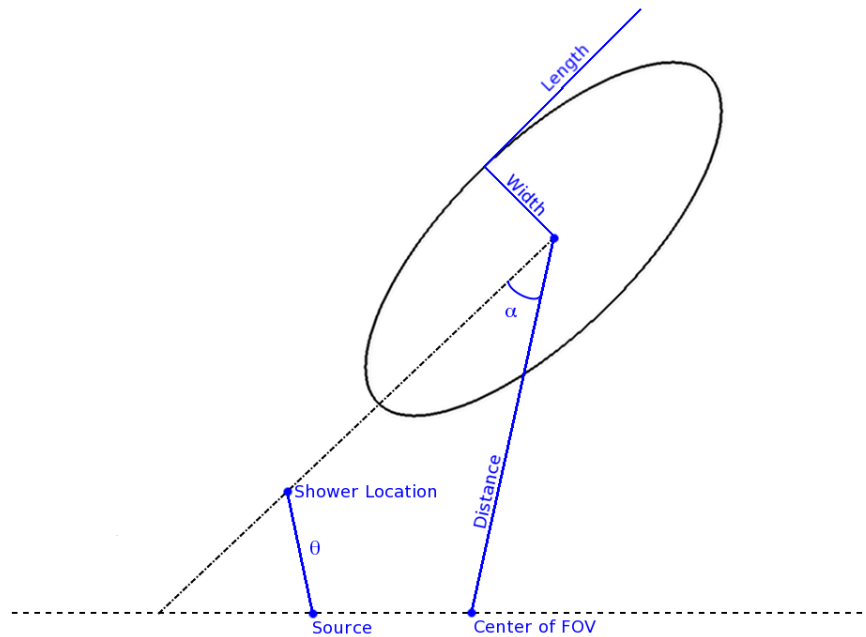


Figure 3.17. An illustration of some of the Hillas parameters used for analysis.

Table 3.1
Image parameters as currently calculated for VERITAS analysis.

Original Hillas Parameters

Parameter	Definition
Distance	Distance from the center of the field of view to the centroid of the image ellipse. This is used to cut on events near the edge of the camera where the signal becomes attenuated.
Length	RMS spread of light along the major axis of the image ellipse. This can indicate the extent of the shower along the shower axis.
Width	RMS spread of light along the minor axis of the image ellipse. This can indicate the transverse size of the shower.
Frac3	Percentage of the total signal of each image contained within the 3 tubes with the highest signal.
Azwidth	RMS spread of light perpendicular to the line connecting center of the field of view to the centroid of the image ellipse.
Miss	Perpendicular distance between the center of the field of view and the major axis of the image ellipse.

Additional Parameters

Parameter	Definition
Size	This is the sum of the digital counts in all the Image tubes. This value is proportional to the amount of light captured in the image.
N_{tubes}	The number of pixels included in an image.
Length/Size	The ratio of the parameters length and size which are described above.
Alpha	The angle between the major axis of the image ellipse and a line drawn from the centroid of the image ellipse to center of the field of view.
θ	The angular distance between the reconstructed shower location in the field of view and the assumed source location.

Quality Selection and Shower Reconstruction - “VEGAS Stage 4.2”

Because the Cherenkov images produced in the telescope cameras are indirect measurements of the primary particle/photon that initiated those showers, it is necessary to first reconstruct the parameters of the showers that caused the images, and then use those reconstructions to estimate qualities of the primary initiators of those showers.

Quality Selection: Before the reconstruction process takes place, some of the parameters found in the previous analysis stage are used to perform quality selection on the Cherenkov light images found during the previous analysis stage. The quality selection is performed to filter out events that may result in inaccurate calculations in the shower reconstruction analysis. For standard analysis procedures, the parameters N_{tubes} , *Size* and *Distance* are used for the quality selection (see Table 3.1 for definitions). A minimum of 5 pixels is required for an image to be included in shower reconstruction because if the number of pixels in an image is small it is more difficult to constrain the shape of the image. Faint images are also removed by a minimum cut on the *Size* of the image. The standard *Size* cut is 400 digital counts, but optimization procedures have found that different values for the *Size* cut can increase sensitivity to sources with harder or softer spectra. Finally, images that appear near the edge of the camera may be inaccurately measured or may not fully be contained by the camera’s field of view. A maximum cut of 1.43° on *Distance* is made to ensure that the shower images are fully contained within the camera.

Shower Source Reconstruction: Reconstruction of the shower source location in the field of view of the camera is necessary to image the locations of each shower initiator and to eventually produce γ -ray images of the sky. When imaging a shower with multiple telescopes, the location of the shower source in the field of view of the camera can be found using simple geometric arguments. The semi-major axes of a shower’s images produced in each telescope’s camera will intersect near the loca-

tion of the shower source in the field of view of the camera. The source location for each shower is calculated by minimizing the perpendicular distance to each image's semi-major axis, weighted by the Size parameter of each image.

Shower Core Reconstruction The location where the axis of the electromagnetic shower intersects with the ground is known as the shower core. This distance between this location and the telescope that images the shower has a strong influence on the image in the camera. This influence becomes important when using qualities of the image to estimate the energy of the initiator of the shower. The use of multiple telescopes makes it possible to measure the location of the shower core in ground coordinates using geometric arguments, similar to those used to determine the shower source in the field of view of the cameras.

A histogram of shower core locations in ground coordinates is shown in Figure 3.18.

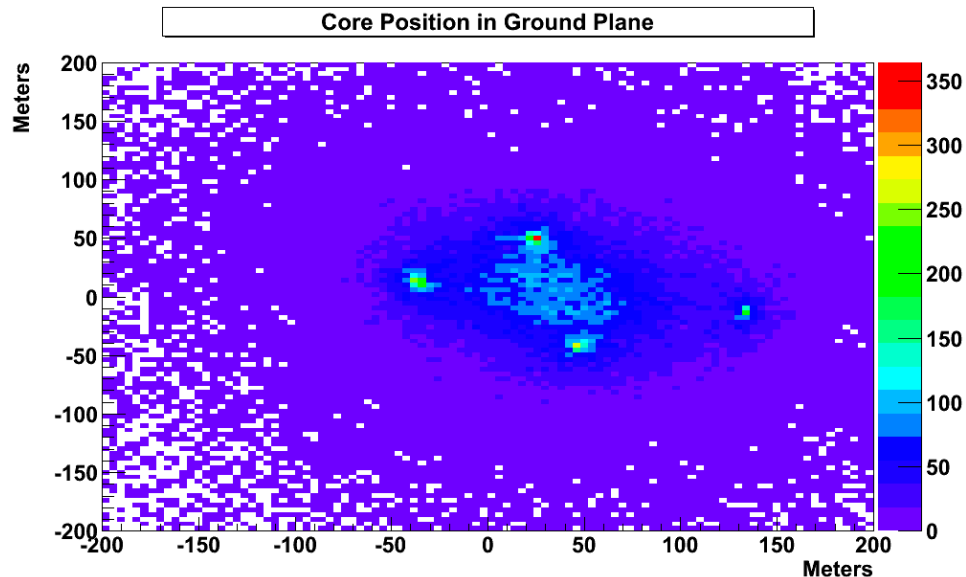


Figure 3.18. A plot of shower core locations shown in ground coordinates.

Shower Parameterization Through this stage of analysis, the shower events retained are still overwhelmingly composed ($> 99\%$) of cosmic ray events. The separation of γ -ray induced showers from cosmic rays is performed in VEGAS by analyzing event parameters at the shower level (including images from all telescopes participating in an event). The quantities used for this separation technique are known as “Mean Scaled Parameters” and was first suggested by Daum et al. [36]. For this technique, simulations of γ -ray showers and the detectors are used to form lookup tables that contain expected values for the telescope level parameters Length and Width based on the impact distance (distance from shower core to the telescope) and Size parameters. These lookup tables are calculated for each telescope with several values of zenith angle, azimuth angle, telescope pointing offset from the source position, and the night sky background noise level.

The lookup tables are used to scale the calculated Length and Width parameter at each telescope using the values expected for a measured impact distance and Size. Then an average of the scaled parameters found at each telescope is taken according to the formula:

$$MSP = \frac{1}{N} \sum_{i=1}^N \frac{p_i}{\bar{p}_{sim}(Size, r)}, \quad (3.8)$$

where N is the number of telescopes participating in an event, i indicates the telescope involved, p_i is the parameter being used in the scaled calculation (Width or Length, here), and \bar{p}_{sim} is the average simulated parameter for the corresponding Size and impact distance r . It is important to note that only the telescopes that are involved in the event are used in the calculation, so the sum will not necessarily begin with telescope 1.

Because the simulated showers are γ -ray initiated, γ -ray events in real data should have Mean Scaled Parameters around 1. Because cosmic ray showers are less compact than γ -ray initiated showers, they will tend to have larger Mean Scaled Parameters. An upper cut is therefore placed on the Mean Scaled Parameters to exclude events that are likely to be cosmic-ray showers. The technique of Mean Scaled Parame-

ters provides a very effective tool for rejecting cosmic ray initiated events while still retaining many γ -ray events.

In addition to the Mean Scaled Parameters, another shower level parameter, θ^2 is calculated based on the shower source direction in the field of view of the camera. θ^2 is defined as the square of the angular offset between the shower source position and the anticipate source position in the field of view of the camera. An excess of events with small values of θ^2 is indicative of a γ -ray source at the anticipated source location.

Shower Energy Reconstruction: Once shower images are selected using the quality selection discussed above, an energy is estimated for each telescope image in an event. This procedure is done using lookup tables prepared similarly to those used for the Mean Scaled Parameters. A lookup table is selected based on the observing conditions, and the energy for each telescope image is determined by the value in the lookup table based on the image Size and the impact distance for that telescope. The energy of the shower is calculated by taking the average of the individual telescope energies weighted by the Size of each telescope image.

Shower Level Cuts - “VEGAS Stage 5”

After the quality selection, shower reconstruction, and shower parameterization procedures are performed in VEGAS Stage 4.2, cuts may be made to remove as many cosmic ray events as possible from the data. These cuts are performed in VEGAS Stage 5 and are generally optimized on data taken on the Crab Nebula.

Results Extraction - “VEGAS Stage 6”

Background Selection Methods: Even after cuts are performed on the Mean Scaled Parameters to exclude the majority of cosmic ray events, many cosmic ray events that are similar to γ -ray events survive through to the final stages of analysis.

Some sort of measurement of this background must be taken to account for these events in the final analysis and calculate the statistical significance of detected γ -ray sources. Two strategies, discussed in detail in [6], are used in VEGAS analysis. These procedures are known as the “ring background model” and the “reflected region background model.” The two models are based on different initial assumptions and therefore are useful for different strategies.

The ring background model is independent of the pointing of the telescopes and source position. As such, this model is ideal for searching sky survey data for sources of unknown location. This model is also used for generating two dimensional sky maps, as the signal in several bins distributed throughout the field of view can be analyzed. The ring background method takes a measurement of background from an annulus (or ring) around a chosen “source” location. The annulus has an inner radius large enough to exclude contamination from the potential source and any region the annulus crosses that contains a known γ -ray source or bright star must be excluded from the calculation. In addition, the event rate is dependent on the distance from the center of the camera’s field of view. Because the annulus covers an area of the camera at many different offsets from the center of the field of view, a correction to the event rate, known as acceptance must be applied to the data.

The reflected region background model (sometimes known as wobble) takes an alternative approach to background estimation. This model assumes an azimuthal symmetry in cosmic ray event rate at a given distance from the center of the field of view of the camera. To obtain both source and background measurements, the source is observed at a set offset from the center of the field of view of the camera. A region of a certain radius around the source is chosen as the “source” region. Background regions are then chosen at the same offset and distance from the source region. In order to improve the statistical significance of the background rate measurement, it is advantageous to use as many background regions as possible. Similar to the ring background method, any background regions that coincide with known γ -ray sources or bright stars are excluded from the analysis. The reflected region background

model analysis requires a corresponding observing strategy known as “Wobble Mode” where the source is observed at a given offset to the center of the field of view. To avoid systematic errors, the offset direction changes between data in a cyclic pattern between North, South, East and West. The reflected region background model is best suited to point-like sources with limited extension. For the VERITAS analysis using the VEGAS package, the reflected region background model is used for spectral analysis.

Background Subtraction and Source Detection: Once a background selection method is selected, the background can be determined and subtracted from the source region in order to estimate the number of excess γ -rays, if any, that are detected. The statistical significance of any detection must also be appropriately estimated. To properly subtract the background from the source region, the relative exposures of the background and source regions must be accounted for. The parameter α accounts for the relative exposure of the regions due to differences in area and observing time. The number of excess γ -rays can then be estimated using the formula:

$$N_{excess} = N_{on} - \alpha N_{off} , \quad (3.9)$$

where N_{on} is the number of counts in the selected source region and N_{off} is the number of counts in the selected background region(s).

The α parameter is calculated differently for the reflected region (wobble) background model and the ring background model. For wobble analysis, α is the ratio of the areas of the source region to the background regions. Because the individual background regions have the same area as the source region, this reduces to:

$$\alpha_{wob} = \frac{1}{N_{BG}} , \quad (3.10)$$

where N_{BG} is the number of background regions used.

For the ring background model, α is found by first integrating the acceptance ($Acc(r)$) over the area of both the source and background regions and taking the ratio of these quantities:

$$\alpha_{rbm} = \frac{\int_{srcreg} Acc(r) dA}{\int_{bgreg} Acc(r) dA} . \quad (3.11)$$

Once α is calculated, the excess in γ rays can be estimated using Equation 3.9. To determine the statistical significance of this excess, N_{ON} , N_{OFF} , and α can be combined using Equation 3.12, known as the Generalized Li & Ma significance. Analysis methods for detection results are discussed in detail in [64].

$$\begin{aligned} Significance = \sqrt{2} \left\{ N_{on} \ln \left[\frac{1 + \alpha}{\alpha} \left(\frac{N_{on}}{N_{on} + N_{off}} \right) \right] \right. \\ \left. + N_{off} \ln \left[(1 + \alpha) \left(\frac{N_{off}}{N_{on} + N_{off}} \right) \right] \right\}^{1/2} . \quad (3.12) \end{aligned}$$

The background rate can be found in this way:

$$Rate_{bg} = \frac{\alpha N_{off}}{T} , \quad (3.13)$$

where T is the dead-time corrected observing time.

Finally, the γ -ray rate from the source region and its significance can be found:

$$Rate_{\gamma} = \frac{N_{on} - \alpha N_{off}}{T} \pm \frac{\sqrt{N_{on} + \alpha^2 N_{off}}}{T} . \quad (3.14)$$

Effective Areas: To obtain flux measurements for spectral analysis and light curve generation, it is necessary to understand the effective collection area of the VERITAS system. The telescopes detect γ -rays indirectly by imaging the Cherenkov light that is produced by electromagnetic showers they initiate in the upper atmosphere. The telescopes are able to detect γ -rays with large impact parameters. That is, the axis of the gamma ray shower need not pass through the optical reflectors on a telescope in order to be detected. Because of this indirect method for detecting

γ -rays, the collection area of the telescopes for γ -rays is not simply the sum of the areas of the optical reflectors. The effective collection area (EA) of the array is found using Monte Carlo simulations of gamma ray showers and simulations of detector responses.

The effective area of the system is dependent on the energy of the primary that initiated the shower, zenith angle, night sky noise, offset of the γ -ray source from the center of the field of view, and the cuts that are made on the data. A set of simulated γ -ray showers is generated covering multiple zenith angles and falling over an area on the ground much larger than the area the telescopes are able to cover. These simulated showers are then passed through a simulation of the detector to produce simulated data files as measured by the telescopes. The simulations are then analyzed through the early stages of VEGAS where noise and pedestals are added to emulate real data, and finally the showers are processed through the reconstruction stages of analysis. The showers that pass through all cuts are then used to calculate the collection area of the array as discussed below.

The first calculation is to find the true effective area of the telescopes in the following manner.

$$A_{eff,i} = \frac{N_{cut,i}}{N_i} \times ShowerArea , \quad (3.15)$$

where $A_{eff,i}$ is the true effective area of the telescopes for showers in energy bin E_i , N_i is the total number of simulated showers in that energy bin, $N_{cut,i}$ is the number of events from the simulations in energy bin E_i that passed all the cuts, and $ShowerArea$ is the total area over which the showers fell.

This value of true effective area gives the collection area for the telescopes if the system were able to perfectly resolve the energy of each incident shower. However, because the system has a finite energy resolution, the reconstructed energies of each simulated shower may not match the true energy of that shower. This results in a shift of $N_{cut,i}$. In order to take this into account a “modified effective area” \tilde{A}_{eff} is calculated by taking into account the distribution of simulated showers into reconstructed energies that differ from their true energies.

During analysis, the energies are binned using bins with a minimum width determined by the energy resolution of the system. The modified effective area, \tilde{A}_{eff} , can be calculated by examining how many showers with true energies in bin E_i are placed in reconstructed energy bin \tilde{E}_j after passing through analysis. In addition, a term known as the energy bias, defined as the mean fractional error in reconstructed energy, is calculated for the simulations. This term helps to determine a “safe energy range” to be used for spectral analysis where the energy estimation is considered reliable.

Spectral Analysis: The energies of each shower have already been estimated in previous stages of the analysis. In order to produce a spectrum of the source, the showers with the ON and OFF regions are each binned according to their energies. After binning, the differential flux in each energy bin can be calculated as:

$$\frac{dN}{dE_i} = \frac{1}{\Delta t \Delta E_i} \left\{ \sum_{j=1}^{N_{ON,i}} \frac{1}{\tilde{A}_{eff}(E_j, \theta_j)} - \alpha \sum_{k=1}^{N_{OFF,i}} \frac{1}{\tilde{A}_{eff}(E_k, \theta_k)} \right\}, \quad (3.16)$$

where ΔE_i is the energy bin width, Δt is the live time for the spectral analysis, N_{ON} is the number of γ -ray events detected in the ON regions, N_{OFF} is the number of γ -ray events detected in the off regions, and α is the ratio of the exposures in the of ON and OFF regions. The modified effective area is used for the calculation to take into account the finite energy resolution of the system and is calculated as discussed above.

Finally, a routine is used to fit the data with a model, usually a simple power law of the form:

$$\frac{dN}{dE} = F_0 \times 10^{-12} \times \left(\frac{E}{1 \text{ TeV}} \right)^{-\alpha} \text{ photons cm}^{-2} \text{ s TeV}^{-1}, \quad (3.17)$$

where F_0 is the normalization at 1 TeV and α is the power law spectral index.

Timing Analysis: Light curves may be produced from the data after the spectral analysis has been performed. The spectral index determined from the fit to the

corresponding data is assumed to be constant, and the effective collection areas are used in conjunction with the excess counts to determine the spectral normalization. An energy threshold must be specified to calculate the integral flux for each time bin.

Further details of specific VEGAS analysis procedures are provided in the following chapters which discuss the use of VHE γ -ray data in conjunction with X-ray data to perform detailed studies of the broadband emission of TeV blazars. In addition, Appendix A describes an analysis optimization script and general analysis procedures that were developed during this thesis work.

4. A Multiwavelength Study of the Blazar Markarian 421

Published in ApJ [3]

4.1 Introduction

Blazars, a sub-class of active galactic nuclei (AGN), are some of the most intriguing sources in the high-energy sky. Their rapid variability and the non-thermal nature of their emission, presenting a continuum across nearly the entire electromagnetic spectrum, imply that the observed photons originated within highly relativistic jets oriented very close to the observer's line of sight [92]. Therefore, blazars are excellent laboratories for studying the physical processes within the jets of AGN. They were among the first sources to be detected at TeV energies and today there are more than 21 known TeV blazars. Blazars are subdivided into three classes: flat spectrum radio quasars, low-frequency-peaked BL Lacs and high-frequency-peaked BL Lacs (HBLs).

Various models have been proposed to account for the broad-band spectral energy distributions (SED)s observed in HBLs, which typically display a characteristic double peak when plotted as νF_ν against ν , with peaks occurring at keV and TeV energies. The models are generally divided into two classes: leptonic and hadronic. Both leptonic and hadronic models attribute the peak at keV energies to synchrotron radiation from relativistic electrons (and positrons) within the jet, but they differ on the origin of the TeV peak. The leptonic models advocate the inverse Compton scattering mechanism, utilizing synchrotron self Compton (SSC) interactions and/or inverse Compton interactions with an external photon field, to explain the TeV emission (e.g., [38, 68, 69, 88]). The hadronic models, however, account for the TeV emission by π^0 or charged pion decay with subsequent synchrotron and/or Compton emis-

sion from decay products, or synchrotron radiation from ultra-relativistic protons (e.g., [5, 67, 78]).

Observationally, HBLs are known to undergo both major outbursts on long time scales and rapid flares on short time scales, most prominently at keV and TeV energies. During some outbursts, both of the SED peaks have been observed to shift towards higher energies in a generally correlated manner (e.g., [19]). The correlation of the variabilities at keV and TeV energies (or lack thereof) during such outbursts has aided in refining the emission models. In addition, rapid, sub-hour flaring is interesting as it provides direct constraints on the size of the emission region. These rapid flares also present an observational challenge to multiwavelength studies, as truly simultaneous data must be used in order to develop a reliable characterization of the broadband behavior of these objects.

Markarian 421 (Mrk421; 1101+384), at a redshift of $z = 0.031$, was the first blazar, as well as the first extragalactic source, to be detected at TeV energies [80] and has since remained one of the most active TeV gamma-ray blazars. It belongs to the HBL class and has been known to demonstrate rapid, sub-hour, flaring behavior at keV and TeV energies during the course of an outburst (e.g., [35, 45]) indicating very compact emission regions. Many extensive multiwavelength campaigns studying Markarian 421 have been undertaken at keV and TeV energies during outbursts, but the degree of simultaneity of the multiwavelength coverage varies and is often not adequate to account for the most rapid variability of the source. Due to these considerations, one must exercise caution in the interpretation of some of the results from these campaigns.

In this work, we report on results from a target-of-opportunity (ToO) program on TeV gamma-ray blazars that makes use of a unique combination of capabilities provided by the *XMM-Newton* satellite and several ground-based imaging atmospheric Cerenkov Telescopes (IACT)s to obtain truly simultaneous coverage at optical, X-ray and TeV gamma-ray wavelengths. Unlike other satellites frequently used for multiwavelength campaigns, *XMM-Newton's* highly elliptical orbit allows for long ob-

servations that are not frequently interrupted by earth occultation. In addition to its X-ray instruments, *XMM-Newton* carries an optical telescope co-aligned with the X-ray telescopes and can thus provide simultaneous coverage in the optical/UV band. While our primary emphasis is on the X-ray and TeV bands, the optical/UV coverage helps to constrain the overall SED shape.

4.2 Observations and Data Reduction

Our ToO program was first triggered in April 2006 by a major outburst from the TeV gamma-ray blazar Markarian 421 as detected by regular monitoring at TeV energies by the *Whipple* 10m telescope. Because of *XMM-Newton* visibility constraints, the coordinated multiwavelength observations did not take place until after the peak of the outburst as indicated by the overall monitoring campaign. The program was triggered again in May 2008 by another major outburst from Markarian 421 detected at TeV energies. However, we once again captured only the decaying portion of the outburst. However, taken together, the two campaigns have produced a significant amount of simultaneous optical, X-ray and TeV gamma-ray data on the source.

4.2.1 XMM-Newton Observations

The X-ray and optical observations were taken by the *XMM-Newton* satellite's EPIC-pn (EPN) detector [90], covering a spectral range of approximately 0.5 - 10 keV, and the Optical Monitor (OM, [70]), capable of covering the range between 170 and 650 nm (7.3 eV and 1.9 eV). The metal oxide semiconductor (MOS) detectors were also operated during some of the observations, but the data were not used here. During both observations, the EPN was operated in fast timing mode to minimize photon pileup at the expense of imaging capability along the direction of event readout. The thin optical filter was in place for both observations. The 2006 and 2008 observations produced EPN exposures of approximately 42 ks and 43 ks, respectively. Due to the brightness of the source, during the first half of the 2008

observations both the EPN and MOS detectors entered into counting mode, resulting in a loss of frames. In an attempt to avoid further frame losses, the MOS detectors were shut down to provide more bandwidth for telemetry to the EPN detector. As a result of the detector being in counting mode, the first half of the EPN observation suffers from telemetry gaps which can be accounted for and corrected as explained below.

In parallel with the EPN observations, a series of exposures was taken utilizing the OM. The 2006 and 2008 observations produced 15 and 10 exposures, respectively, with total exposure times of 32.5 ks and 22.0 ks. For all exposures, the OM was in imaging mode with the UVM2 filter (200 - 300 nm) in place. Table 4.1 summarizes these observations.

The 2006 EPN data were initially processed using XMMSAS v7.0 [44]. Standard XMM-Newton data analysis procedures were followed to filter and reduce the data, generate the various lightcurves, extract the source and background spectrum, and generate the RMF and ARF files for subsequent spectral analyses. In summary, the event list was examined to check for periods of soft proton flaring, where background event rates are higher than 0.4 cts/sec (for events with energies $E > 10$ keV). In addition, “bad events” were removed including events which were close to CCD gaps or bad pixels, and only single and double photon events were included ($PATTERN \leq 4$). A one dimensional histogram of counts was produced to determine the position of the source. Based on the histogram, we chose columns 30-45 (in RAWX) for the source region and columns 1-15 and 57-64 for the background region. These regions were used to extract source and background spectra.

The 2008 EPN data were processed similarly, using the same filtering criteria, but with XMMSAS v8.0. In this case the source region was determined to be in columns 31-45 and the background regions were taken to be columns 1-19 and 57-63. It should be noted that a new SAS task, *epiclccorr*, was used to correct for the effects of deadtime, telemetry saturation, and frame dropouts in producing the light curves from the 2006 and 2008 data.

The OM data were analyzed with the standard SAS task *omichain*, which produces images and source lists for all OM exposures present in any given observation. The 2006 OM observations presented here are a combination of 15 exposures with 2000 s and 2500 s integration times while the 2008 data comes from 10 exposures each with a duration of 2200 s.

Table 4.1
Summary of Markarian 421 *XMM-Newton* Observations.

Obs. ID	Start Time	PN Exposure (ks)	Avg. PN Rate (cts s ⁻¹)	Avg. OM Rate (cts s ⁻¹)
0302180101	2006 Apr 29 20:44UT	41.9	336.30 ± 0.09	13.5±0.2
0502030101	2008 May 07 01:34UT	43.2	411.31 ± 0.12	35.82 ± 0.03

4.2.2 TeV Gamma-Ray Observations

Three ground-based IACT facilities were utilized to observe the source at TeV energies during the *XMM-Newton* observations. These IACTs detect gamma-rays by imaging the flashes of Cerenkov light emitted by gamma-ray induced electromagnetic showers within the atmosphere. The *Major Atmospheric Gamma Imaging Cerenkov* (MAGIC) telescope provided 14 ks of coverage during the first part of the 2006 *XMM-Newton* observation, and the *Whipple* 10m telescope provided 12 ks of coverage during the latter part of the 2006 observation. The geographic separation of the experiments allowed for extended, simultaneous coverage during the *XMM-Newton* observation. During the 2008 *XMM-Newton* observation, only the *Very Energetic Radiation Imaging Telescope Array System* (VERITAS) was used, providing 9 ks of TeV coverage.

Whipple Data

The *Whipple* 10m IACT [58] focuses Cerenkov light on a camera composed of 499 photo multiplier tubes (PMTs). The energy threshold for the *Whipple* 10m is near 400 GeV. There are two modes used for taking data. During the 2006 observation, two hours of data were taken in TRACKING mode, where the source is centered in the camera, and two hours of data were taken in ON/OFF mode, where half of the data runs are offset from the source by 30 minutes in right ascension to provide an independent measurement of background events (primarily cosmic-rays). The runs each had a duration of 28 minutes, and the total time on source for the *Whipple* 10m telescope was 3 hours on 2006 April 30 from 4:37 UT to 8:05 UT. The observations were taken with a source elevation range of 45 – 79, with an average elevation of 64 and during favorable weather conditions.

Whipple data reduction involves two stages, image cleaning and image parameterization. In the cleaning stage, the data are flat-fielded using a run during which a nitrogen arc lamp is pulsed to illuminate the camera's pixels. Any differences between night-sky background between ON and OFF runs is also accounted for at this stage. In addition, pixels that make up shower images are selected and the remaining background pixels are then removed prior to image parameterization [79]. During the image parameterization stage, each Cerenkov image in the telescope's camera is characterized by an ellipse, using a moment analysis of the recorded signal amplitudes in each pixel. Each shower is characterized by the major axis (*length*), minor axis (*width*), the angle between the major axis of an image's ellipse and a line from the centroid of the ellipse to the source position (α), the length of this line (*distance*), and the overall signal of the shower (*size*). These are known as Hillas parameters and they allow for the removal of the primary source of background, cosmic rays, by exploiting the intrinsic differences in the development of hadronic cosmic ray and gamma-ray showers [54]. These differences result in different distributions of light at ground level and cuts can be used to select events most likely to be gamma-rays. Standard

cuts were made on the Hillas parameters, as shown in Table 4.2, to reject as many background events as possible while still retaining many gamma-ray candidates.

The runs taken in ON/OFF mode obtain a direct measurement of background from the off-source runs, while in TRACKING mode a “tracking ratio” is used to estimate the background. Gamma-ray events should have a small α parameter if the source is centered in the field of view, so events with large values for α can be used to estimate the background if the ratio between background rates at small and large values of α is known in the absence of a source. This “tracking ratio” used here was found by taking observations of blank sky fields with no detected TeV gamma-ray sources throughout the 2005 – 2006 observing season. It is defined as the ratio of the integrated number of events between $\alpha = 0 - 15$ and those between $\alpha = 20 - 65$. Once it is calculated, the tracking ratio is used to estimate background rates for all TRACKING observations.

Table 4.2
Whipple Event Selection Parameters

Parameter	Values for Cuts
Trigger level	> 30 digital counts
Shape cuts	$0.05^\circ < \text{width} < 0.12^\circ$ $0.13^\circ < \text{length} < 0.25^\circ$
Muon cut	$\text{length/size} < 0.0004^\circ \text{dc}^{-1}$
Distance cut	$0.4^\circ < \text{distance} < 1.0^\circ$
Orientation cut	$\alpha < 15^\circ$

MAGIC Data

MAGIC is the largest single dish Cerenkov telescope in operation [17, 34]. A 17 m tessellated reflector focuses the light from air showers on a camera composed of 576

PMTs. For high elevation angle observations, the MAGIC trigger threshold currently reaches down to 50 – 60 GeV [10].

The measurements reported in this article were conducted from 2006 April 29 21:32 UT to 2006 April 30 00:59 UT at elevation angles spanning $49^\circ - 81^\circ$. MAGIC observed the source employing the so-called *wobble* mode [40], during which the telescope alternates between tracking two (or more) opposing sky directions, each 0.4° off-source, for 20 minutes each [13]. After removing events not containing sufficient information for further analysis (see Table 4.3 top), events from accidental triggers, triggers from nearby muons, and data affected by adverse meteorological conditions, 2.8 hours out of the 3.8 hours of data were used for further analysis.

The data were processed using the analysis and reconstruction software package for MAGIC data [26]. A description of the different analysis steps can be found in [49], [10] and [25]. For this analysis, the signal was extracted using a spline algorithm. After calibration, the shower images were cleaned of background noise by requiring a minimum photoelectron signal in the pixels as well as temporal coincidence with adjacent pixels (time image cleaning, see [13]). The recorded events are characterized by several image parameters based on the shower light distribution (amongst them the previously mentioned Hillas parameters) and on the temporal shower development in the camera plane (*slope*, see [13]). True gamma-ray events coming from the observed source are extracted from the hadronic background by cuts in this image parameter space, using the separation cuts listed at the bottom of Table 4.3. Events originating from the source are selected by a cut on θ^2 (where θ is the angular distance between the expected source position and the reconstructed gamma-ray arrival direction). Gamma-ray events are then separated from background events by a *size* dependent parabolic cut in $width \times length \times \pi$ [83].

The Markarian 421 observations presented here are among the first data taken by MAGIC after major hardware updates in April 2006. Due to these changes, a thorough examination of the data was undertaken to ensure its reliability. Despite the hardware changes, all MAGIC subsystems were working as expected with the

exception of an unstable trigger behavior for some PMTs, leading to an early signal arrival time for those affected. A careful study of the systematics in the low energy region has been conducted, leading to the decision of raising the energy threshold to 250 GeV [13].

Table 4.3
MAGIC Cuts. Leakage parameter is defined as the ratio of the signal in the outer pixels of the camera to the total signal.

Parameter	Values for Cuts
Number of shower islands	< 3
Number of used pixels	> 5
Leakage	< 0.3
Gamma/Hadron Separation Cuts:	
θ^2	< 0.046
Area	$< 0.265 \times (1 - 0.0803 \times (\log_{10}(size) - 5.77)^2)$
Standard time cuts	$slope > (distance - 0.5) \times 7.2$

VERITAS Data

VERITAS is an array of four 12 m diameter IACTs each focusing light on a camera consisting of 499 PMTs. Utilizing multiple telescopes provides a stereoscopic view of showers, making it possible to significantly reduce muon events. This substantially improves the low energy performance of the detector since images produced from nearby muons are otherwise virtually indistinguishable from images produced by low-energy gamma-rays. Therefore the array allows for a lower energy threshold than possible with a single telescope of the same size operating alone. For *VERITAS* this threshold is near 275 GeV. In addition, stereoscopic observations facilitate a much

improved determination of the core position of showers and thus provide improved energy resolution and background rejection.

During the 2008 observation, *VERITAS* took data on Markarian 421 while operating in *wobble* mode, with an offset angle of 0.5. To provide background estimations using this observation mode, we follow the reflected-region model [18] where one collection region is placed at the source position and others of equal size are placed at equal offsets from the center of the field of view and used for background measurements. *VERITAS* observed Markarian 421 for 2.5 hours on 2008 May 07 from 3:59 UT to 6:28 UT using a series of 20 minute runs, with an effective exposure time of 129.7 minutes. The observations were taken as the source elevation ranged from 79 to 55. Data quality checks confirmed good weather during the observations.

The *VERITAS* data from 2008 was analyzed with Veritas Gamma-ray Analysis Suite (VEGAS), the standard *VERITAS* analysis package [32]. The shower images were first corrected for relative gains and cleaned to remove isolated pixels. The images were then parameterized in a similar manner as for *Whipple* analysis. Initial quality cuts were made on the images' *size*, pixel count and *distance*. For this analysis, events that survived the initial cuts but only contained data from the two telescopes with the smallest physical separation were removed. This smaller separation distance results in a greater number of muons surviving the initial cuts, and in addition these events can distort the calculation of impact distance due to the relatively small distance between the telescopes. After stereoscopic reconstruction and calculation of each event's impact distance (distance from the shower core to the telescope), the events were parameterized using the quantities mean scaled width (MSW) and mean scaled length (MSL) [36, 62]. These parameters are found by scaling the width and length parameters for a given telescope by the average expected values from simulations given an impact distance and size and then finding the average for all telescopes involved in an event. Cuts on MSW and MSL were made to separate gamma-ray events from cosmic-ray events. Table 4.4 details the cuts that are discussed above. A summary of all TeV gamma-ray data is shown in Table 4.5.

Table 4.4
VERITAS Cuts

Parameter	Values for Cuts
<i>Size</i>	> 400 digital counts
Pixels	≥ 5
<i>Distance</i>	≤ 1.43
Mean Scaled Width	$0.05 < \text{MSW} < 1.16$
Mean Scaled Length	$0.05 < \text{MSL} < 1.36$

Table 4.5
Gamma-ray data run information. Some data were removed due to adverse meteorological conditions.

Facility/Date	Time	Wobble Direction	Significance (σ)
MAGIC			
2006 Apr 29	21:29 UT	0.40+000	12.0
	21:49 UT	0.40+180	9.3
	22:41 UT	0.40+180	5.0
	22:51 UT	0.40+000	7.6
	23:11 UT	0.40+180	8.4
	23:31 UT	0.40+000	8.9
	23:52 UT	0.40+180	6.6
2006 Apr 30	00:12 UT	0.40+000	6.0
	00:32 UT	0.40+180	5.9
	00:53 UT	0.40+000	4.4
		TOTAL	23.7
WHIPPLE			
2006 Apr 30	04:37 UT	TRACKING	4.9
	05:05 UT	TRACKING	5.4
	05:39 UT	TRACKING	6.6
	06:07 UT	TRACKING	3.7
	06:37 UT	ON/OFF	4.8
	07:37 UT	ON/OFF	5.3
		TOTAL	12.5
VERITAS			
2008 May 07	03:59 UT	0.5 N	15.5
	04:21 UT	0.5 S	15.4
	04:43 UT	0.5 E	16.9
	05:04 UT	0.5 W	13.5
	05:26 UT	0.5 N	15.2
	05:47 UT	0.5 S	14.6
	06:08 UT	0.5 E	13.7
		TOTAL	39.6

4.3 Results

4.3.1 Time Averaged TeV Gamma-Ray Spectra

We followed the procedures from [75] in constructing a spectrum based on the *Whipple* data. This method depends on separate energy estimates for both on-source and off-source runs, so the runs taken in the TRACKING mode were matched to contemporaneous OFF runs taken at similar elevation angles. The selected matched runs were taken within two days of the Markarian 421 observations and at elevation angles within 1° of the corresponding TRACKING runs. The energy spectrum was fit using a simple power law:

$$\frac{dN}{dE} = F_0 \cdot 10^{-11} \cdot \left(\frac{E}{1 \text{ TeV}} \right)^{-\alpha} \cdot \frac{\text{photons}}{\text{TeV cm}^2 \text{ s}}. \quad (4.1)$$

The best-fit parameters were $\alpha = 2.23 \pm 0.38$ and $F_0 = 2.65 \pm 0.77$, yielding a $\chi^2/\text{d.o.f.}$ of 0.17/3 ($P = 98.2\%$). Uncertainties are statistical only.

The *MAGIC* spectrum was derived on the same data basis as the light curve but a somewhat looser area cut was applied. This cut yielded a constant cut efficiency as a function of energy of 90% for Monte Carlo simulated gamma-ray events, increasing the gamma-ray event statistics at the threshold [11]. The energies of the gamma events were reconstructed using a random forest regression method [8,23] trained with Monte Carlo events. The *MAGIC* spectrum was modeled similarly to the *Whipple* spectrum, finding best fit parameters of $\alpha = 2.28 \pm 0.09$ and $F_0 = 2.49 \pm 0.17$, yielding a $\chi^2/\text{d.o.f.}$ of 2.04/4 ($P = 72.9\%$). All the stated uncertainties for MAGIC are purely statistical. The energy scale is known with an uncertainty of $\pm 16\%$, the flux normalization within a systematic error of 11% (not including the energy scale error), and the fitted power law slope has a systematic uncertainty of ± 0.2 [10].

For the MAGIC analysis, an additional systematic uncertainty is provided to account for possible effects arising from the hardware instability mentioned above. These effects consist of a moderate loss of low-energy showers as well as a minor additional uncertainty in the image parameter calculation for showers of higher energy.

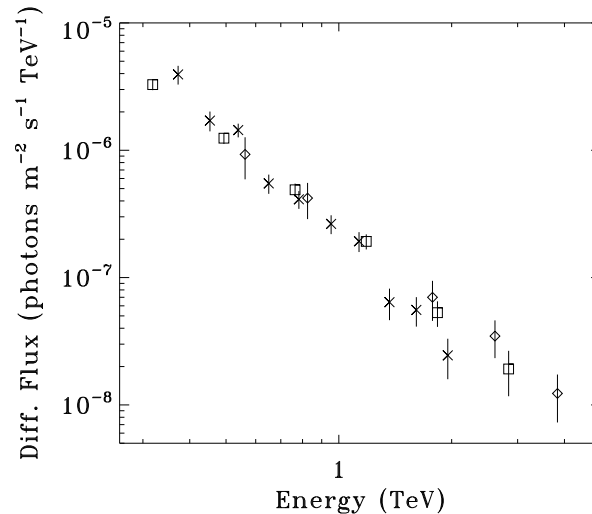


Figure 4.1. TeV spectral analysis results, showing the data obtained with *MAGIC* (squares, $\alpha = 2.28 \pm 0.09$ and $F_0 = 2.49 \pm 0.17$), *Whipple* (diamonds, $\alpha = 2.23 \pm 0.38$ and $F_0 = 2.65 \pm 0.77$) and *VERITAS* (crosses, $\alpha = 2.91 \pm 0.13$ and $F_0 = 2.01 \pm 0.15$).

The effect on the differential flux level is estimated to be 10% from 250 GeV to 400 GeV and 3% for higher energies [13].

The spectral analysis for the *VERITAS* data was performed using the VEGAS analysis package [32], with the same model for background estimates as used for the light curve. The spectrum was again fit with a simple power law model, giving best fit parameters of $\alpha = 2.91 \pm 0.13$ and $F_0 = 2.01 \pm 0.15$, yielding a $\chi^2/\text{d.o.f.}$ of 9.66/8 ($P = 29.0\%$). Again, stated uncertainties are statistical only. The results from the spectral fits for all TeV data can be seen in Figure 4.1.

4.3.2 Spectral Energy Distribution and Modeling

The X-ray spectrum was initially fit using XSPEC 12. The data were fit with a power law modified by interstellar absorption, yielding a value for the photon index of $\alpha = 2.258 \pm 0.002$ and 2.153 ± 0.002 for the data obtained simultaneously with the 2006 *MAGIC* and *Whipple* 10m observations, respectively. For X-ray data taken

during the 2008 *VERITAS* observations, a photon index of $\alpha = 2.519 \pm 0.010$ was found. The hydrogen column density was left as a free parameter for all fits, finding values of $3.16 \times 10^{20} \text{cm}^{-2}$, $2.25 \times 10^{20} \text{cm}^{-2}$ and $4.51 \times 10^{20} \text{cm}^{-2}$ for the data obtained simultaneously with the *MAGIC*, *Whipple* 10m and *VERITAS* observations, respectively. Using these results, the spectrum was unfolded and de-absorbed to derive the intrinsic X-ray spectrum of Markarian 421. Only statistical errors were taken into account here. In addition, the count rates found for the OM exposures were converted to flux using the standard conversion factor¹ and an average point was determined for each time interval. In addition, using the ultraviolet extinction law from [28], the absolute extinction for the UVM2 band was calculated to be $A(\text{UVM2}) = 0.13$, allowing for de-reddening of the OM data using a correction factor of 1.13.

Figure 4.2 shows the broadband SEDs corresponding to the three epochs of TeV gamma-ray observations. It is important to note that within each epoch the multi-wavelength data are genuinely simultaneous. Spectral variability is observed between epochs.

Modeling of the SEDs was carried out using a leptonic model that is described in more detail in [21]. In this model, the spectral distribution of injected electrons is described by a power law with low and high energy cutoffs of γ_{min} and γ_{max} , respectively. The emitting region is assumed to be in a state of temporary equilibrium and of spherical shape, with radius R , and moves out along the jet at relativistic speed $v/c = (1 - 1/\Gamma^2)^{1/2}$, where Γ is the bulk Lorentz factor. As the emitting region moves along the jet, particles cool due to radiative losses and may escape from the region. The timescale of these escapes is factored into the model as $t_{esc} = \eta R/c$, with $\eta \geq 1$. The radiative processes considered include synchrotron radiation, SSC, and inverse Compton scattering of external photons. However, we found that a model with a negligible contribution from external photons (i.e., a pure SSC model) provides a good match to the SEDs during both observations. In addition, the SED matches have been absorbed with the extragalactic background light model discussed in [42].

¹See: <http://heasarc.nasa.gov/docs/xmm/sas/USG/node135.html>

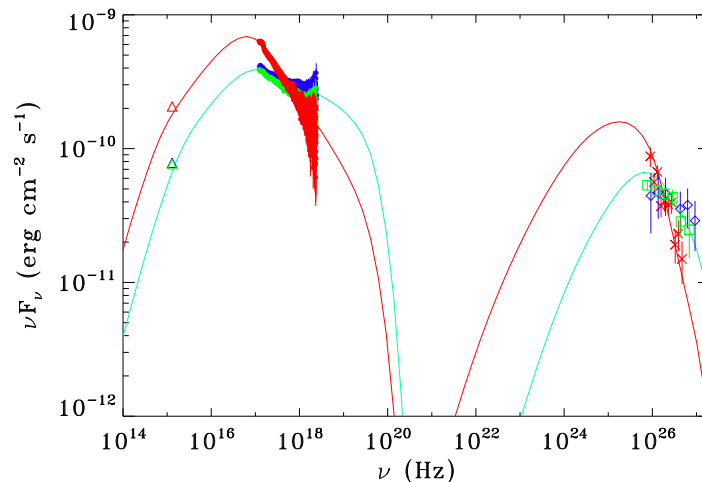


Figure 4.2. Spectral energy distribution with the SSC model for the 2006 (teal blue) and 2008 (red) data. The data from *XMM-Newton OM*, *XMM-Newton EPN*, *MAGIC*, *Whipple* and *VERITAS* are shown with triangles, filled circles, squares, diamonds, and crosses, respectively, with data taken during the *MAGIC*, *Whipple* and *VERITAS* observation times shown in green, blue and red. Error bars for the XMM-Newton OM data and much of the XMM-Newton EPN data are smaller than the data points.

The values for the model parameters were varied until a good match was found for the 2006 and 2008 SEDs. The parameters for these models are shown in Table 4.6. The models are also shown in Figure 4.2.

4.3.3 Cross-Band Correlation

The TeV gamma-ray, X-ray and optical light curves are shown in Figure 4.3 with $1\text{-}\sigma$ uncertainties. The X-ray lightcurve was initially binned using a time interval of 500 seconds, while the bins for the TeV gamma-ray lightcurves were primarily determined by the standard length of data runs for the respective telescopes. The *Whipple* 10m, *MAGIC*, and *VERITAS* data are in 28-minute, 22-minute and 20-

Table 4.6
SED Model Parameters

Parameter	2006 Apr 29-30 Value	2008 May 7 Value
γ_{min} :	8.0×10^4	4.0×10^4
γ_{max} :	2.0×10^6	1.0×10^6
injection electron spectral index:	2.30	3.01
Escape time parameter ($t_{esc} = \eta R/c$)	$\eta_{esc} = 350$	$\eta_{esc} = 50$
Magnetic field at z_0 [G]:	0.031	0.2
Bulk Lorentz factor:	$\Gamma = 80$	$\Gamma = 50$
Blob radius [cm]	5.0×10^{15}	2.9×10^{15}
Observing angle [degrees]	$\theta_{obs} = 0.72$	$\theta_{obs} = 1.2$
L_e (jet)	$3.60 \times 10^{43} \text{ erg s}^{-1}$	$2.11 \times 10^{43} \text{ erg s}^{-1}$
L_B (jet)	$5.77 \times 10^{41} \text{ erg s}^{-1}$	$3.15 \times 10^{42} \text{ erg s}^{-1}$
L_B/L_e	1.6×10^{-2}	1.50×10^{-1}

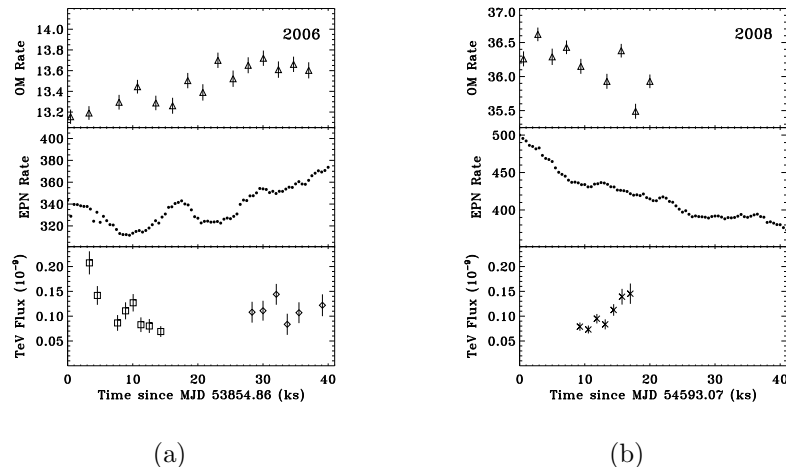


Figure 4.3. Plot of light curves from (a) 2006 observations and (b) 2008 observations. *XMM-Newton* OM data (200-300nm) is shown with triangles in units of cts s^{-1} . *XMM-Newton* EPN data (0.5 - 10.0 keV) is shown with filled circles in units of cts s^{-1} . Error bars for the EPN data are smaller than the data points. The data from *MAGIC*, *Whipple* and *VERITAS* are shown with squares, diamonds, and crosses, respectively in units of $\text{photons cm}^{-1} \text{s}^{-2}$ (above 250 GeV). Note that the EPN and OM scales differ on the 2006 and 2008 panels.

minute bins, respectively. To provide a direct comparison between the results obtained with different TeV gamma-ray experiments, we show the gamma-ray fluxes above a common energy threshold (250 GeV). To reach this threshold for the *Whipple* 10m, the flux was extrapolated from the power law spectrum fit to the data. In addition, contemporaneous data taken on the Crab Nebula, a standard candle for TeV gamma-ray experiments, were studied to assess systematic uncertainty in the flux calibration of the TeV gamma-ray data. The systematic uncertainty in flux calibration between the *MAGIC* and *VERITAS* experiments was estimated to be on the order of 10% with *MAGIC* systematically measuring a lower flux than *VERITAS*. The systematic uncertainty in the *Whipple* 10m and *VERITAS* flux calibration was found to be on the order of 40% with the *Whipple* 10m systematically measuring a higher flux than *VERITAS*. These systematic uncertainties are not included in the data.

The error bars on the TeV gamma-ray data are relatively large, so in order to quantify the variability, we first tested the points by fitting a constant flux value to the data. The resulting fit had a χ^2_ν of 3.92 for 20 degrees of freedom. Similarly, the MAGIC data alone were fit to a constant, with a χ^2_ν of 5.22 for 6 degrees of freedom. This inconsistency of the data with fits to a constant indicates significant variability in the TeV gamma-ray band. Markarian 421 also varied significantly at X-ray energies during the 2006 observation, with the count rate initially decreasing during the course of the *MAGIC* observation and slowly increasing during the *Whipple* observation. Though both showed significant variability, the X-ray and TeV gamma-ray data from 2006 do not appear to be correlated. During the portion of the 2006 *XMM-Newton* observation where there is no corresponding TeV gamma-ray data, there appears to be a rapid X-ray flare, examined in more detail in Section 4.3.4. During the 2008 observation, the X-ray count rate decreases throughout the *XMM-Newton* observation. The rates from the OM aboard *XMM-Newton* during both observations appears to roughly follow the trend of the X-ray rates, with a significantly higher rate during the 2008 observation. There appears to be no correlation between the TeV gamma-ray and optical variations, most notably during the first half of the 2006 observation, where the OM rate increases as the TeV gamma-ray rate decreases.

To examine the X-ray/TeV gamma-ray correlation more quantitatively, we show in Figure 4.4 the measured TeV gamma-ray flux and X-ray count rates. The X-ray data were rebinned to match the resolution of the corresponding TeV gamma-ray data. Evidence of a correlation between the X-ray and TeV gamma-ray data is not found with a Pearson's r calculated as -0.04. To compare to previous work, the best fit correlation between the X-ray and TeV gamma-ray bands found in [19], a long term monitoring campaign that took place during 2003-2004, is plotted in Figure 4.4 (dotted line). In order to carefully compare this previous result to our results, the PIMMS tool² was used to convert the *RXTE* count rates to *XMM-Newton* count rates, taking into account energy range, spectral shape and hydrogen column density.

²See: <http://heasarc.gsfc.nasa.gov/Tools/w3pimms.html>

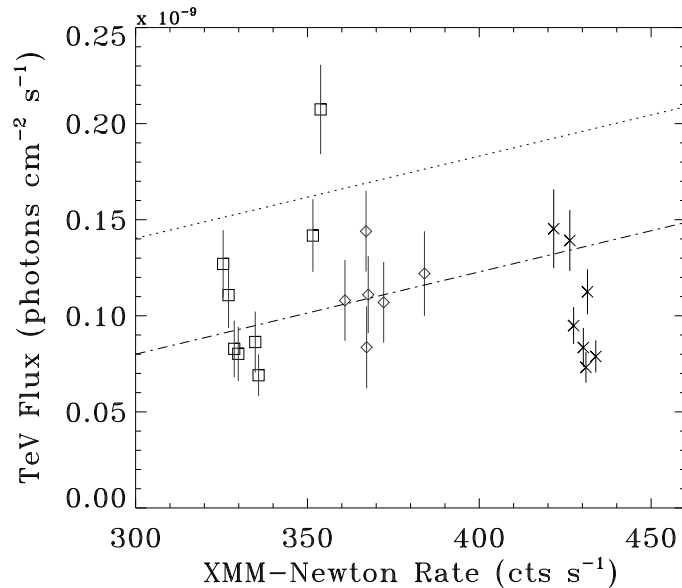


Figure 4.4. Plot of simultaneous *XMM-Newton* EPN (0.5 - 10 keV) and TeV data to search for correlation between the two bands. MAGIC data points are designated by squares, *Whipple* points by diamonds, and *VERITAS* points by crosses. All *XMM-Newton* data used for this plot was analyzed with XMMSAS version 8.0.0 to maintain consistency. The dotted line is the X-ray/TeV gamma-ray correlation best fit from [19] converted to the appropriate units. The dot-dashed line has the same slope but is scaled to the average of our *Whipple* 10m results.

To more directly compare our data to [19], we scaled the correlation to match our *Whipple* 10m points in Figure 4.4 (dot-dashed line). The overall normalization shift could be a reflection of hysteresis on long timescales. Although the scatter in the TeV gamma-ray points are large, the *VERITAS* points are systematically below the scaled correlation. This effect is made worse by the fact that the *Whipple* 10m points are known to be systematically higher than the *VERITAS* points (by 40%).

4.3.4 Spectral Hysteresis

We also examined the spectral evolution of the X-ray data to determine if any hysteresis was present during the observations indicating a dependence of the system on previous states. The data were divided into three energy bands in order to calculate hardness ratios: 0.5 - 1 keV, 1 - 3 keV, and 3 - 10 keV. These bands were chosen such that each band contains a roughly equal number of counts. Figure 4.3.4 shows the evolution of the hardness ratios versus intensity (in terms of count rates) through the flare seen in the 2006 data (which peaks near 17-18 ks into the observation; see Figure 4.3). Spectral hysteresis is clearly seen during this rapid flare. Clockwise patterns indicate a lag in the response of lower-energy photons with respect to that of higher-energy photons. Similar patterns have been seen previously (e.g., [27]), though counter-clockwise patterns have been observed as well [35]. Different hysteresis patterns indicate a complex mechanism that may differ between outbursts.

No rapid flares were observed during the 2008 observation. Examination of the entire 2008 observation did not reveal any overall spectral hysteresis pattern occurring on the order of several hours. Similarly, no overall hysteresis was found when considering the entire 2006 observation.

4.4 Discussion

This work provides the results from a ToO campaign with the primary focus of studying the rapid flaring activity of blazars on sub-hour timescales both at X-ray and TeV gamma-ray energies. In addition, these observations expand the pool of truly simultaneous, multiwavelength observations of blazars, essential for the study of correlations during rapid flares. The rapid flares are expected to be correlated at both X-ray and TeV gamma-ray energies in the SSC scenario, as all photons are expected to originate from the same population of electrons. Examination of the observed SEDs can provide additional constraints on model parameters and reveal what factors strongly affect each flare's spectral profile.

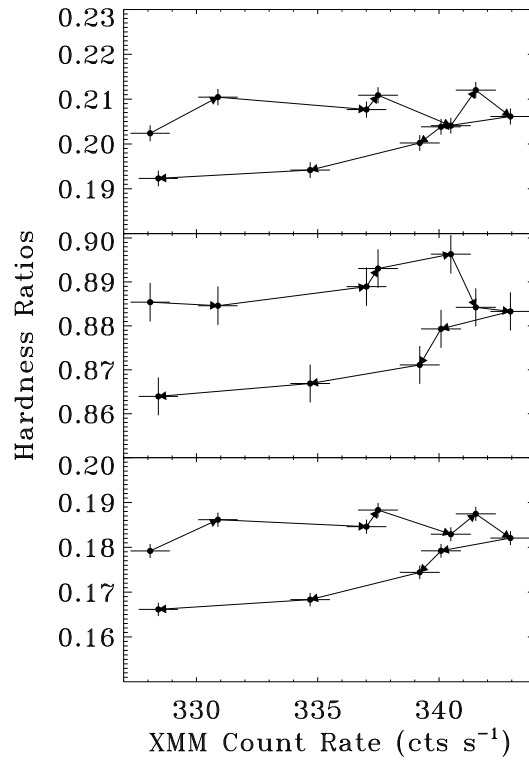


Figure 4.5. Hardness ratio vs intensity plots to study spectral hysteresis during the increase in activity centered around 17 ks into the 2006 *XMM-Newton* observation. Three bands are used for this analysis. The upper panel uses $(3-10 \text{ keV})/(1-3 \text{ keV})$ for the hardness ratio, the middle panel uses $(1-3 \text{ keV})/(0.5-1 \text{ keV})$, and the bottom panel uses $(3-10 \text{ keV})/(0.5-1 \text{ keV})$. The arrows indicate the progression of time. Clockwise hysteresis is present in all three panels, indicating a lag in the lower energy bands.

We also searched for hysteresis patterns in the X-ray data to provide further information about the outbursts. Hysteresis was observed during one rapid flare in the X-ray data from the 2006 observation. No rapid flares occurred during the 2008 observation. Spectral hysteresis has been commonly observed in blazars, but the phenomenon is not yet understood completely. In [59], a simple model is used to produce spectral hysteresis patterns that may be observed during the course of a flare. In this model, the behavior is characterized by the relationship between three timescales associated with the duration of the flare variability (t_{var}), synchrotron cooling (t_{cool}) and particle acceleration (t_{acc}). The relationship between these timescales result in four possible cases that are discussed in detail. The clockwise hysteresis found in the X-ray data, indicating a lag at lower energies in the X-ray band, coupled with the essentially symmetric shape of the flare in the X-ray light curve seems to indicate that the case with $t_{cool} \gg t_{var} \gg t_{acc}$ is most relevant to this observation. The lag in the low energy photons is a result of the inverse relationship between t_{cool} and the energy of the cooling particles. Although we observed clockwise patterns in one of the observations, other patterns have been observed and may indicate physical differences between individual flares and outbursts.

The average rate from the *XMM-Newton* PN detector during the 2008 observation was about 20% higher than the rates measured during the 2006 observation. In addition, examination of the OM data in the UV band shows that the count rate more than doubles between the 2006 and 2008 observation. During this interval, the X-ray rate also increases, though less dramatically. The UV rate also appears to vary in step with the X-ray rate within the individual observations. This apparent correlation in the data may point to a link between the emission mechanisms at the two wavelengths.

The SED fits show a steeper spectrum for the 2008 observation than for the 2006 observation, particularly at X-ray energies. This is intriguing as previous investigations have observed spectral hardening with increased flux (e.g., [96]). In addition, both peaks in the SED show a slight shift to lower energies during the 2008 observa-

tion where previous investigation has shown a shift to higher energies with increased luminosity (e.g., [19]). Figure 4.2 shows that the one-zone SSC model fits both the 2006 and 2008 data quite well.

The variability observed during the 2006 outburst in the simultaneous observations at both X-ray and TeV gamma-ray energies should be enough to provide useful information about a correlation, if any, between the two energy bands. In addition, the observations from 2008 during a separate outburst, provide an extended picture for investigating possible correlations between these two bands. Historically, multiwavelength monitoring campaigns have observed correlation between the X-ray and TeV gamma-ray emission in Markarian 421, though the data sets are not comprised entirely of strictly simultaneous multiwavelength data (e.g., [19, 41]). Surprisingly, both the 2006 data alone and the entire 2006/2008 data set show no obvious correlation, with a Pearson's r of -0.04, though the SSC model fits the SEDs well (see Figure 4.2 and Figure 4.4). This is challenging, because the simplest SSC picture, where flaring activity is dominated by an increasing number of ultrarelativistic electrons, predicts a strong, positive correlation between X-ray and TeV gamma-ray observations. Alternatively, a scenario similar to that discussed in [7], another campaign focusing on simultaneous observations of an HBL, is a possibility, with electrons at different energy ranges within the same population accounting for the X-ray and TeV gamma-ray photons. Other scenarios that could explain the observed variability patterns include the possibility of an inhomogeneous emission region or hadronic origin of the TeV emission. However, Markarian 421 is clearly behaving very differently here from what is usually reported of the source (e.g., [19]), where the X-ray and TeV gamma-ray variabilities are seen to be strongly correlated. Such personality makes it difficult to generalize the results to other blazars.

Acknowledgments. The *VERITAS* research was supported by grants from the U.S. Department of Energy, the U.S. National Science Foundation and the Smithsonian Institution, by NSERC in Canada, by Science Foundation Ireland and by STFC in the U.K.. We acknowledge the excellent work of the technical support staff at the FLWO

and the collaborating institutions in the construction and operation of the instrument. D.G. and W.C. wish to acknowledge support by NASA through grants NNX06AB96G, NNX08AD76G, and NNX08AX53G. The *MAGIC* collaboration thanks the Instituto de Astrofísica de Canarias for the excellent working conditions at the Observatorio del Roque de los Muchachos in La Palma. The support of the German BMBF and MPG, the Italian INFN, and Spanish MCINN is gratefully acknowledged. This work was also supported by ETH Research Grant TH 34/043, by the Polish MNiSzW Grant N N203 390834, and by the YIP of the Helmholtz Gemeinschaft.

5. Spectral Energy Distribution of Markarian 501: Quiescent State vs. Extreme Outburst

In preparation, [2]

5.1 Introduction

The very high energy (VHE; $E > 100$ GeV) blazar Markarian 501 has a well studied history of extreme spectral variability and is an excellent laboratory for studying the physical processes within the jets of active galactic nuclei. However, there are few detailed multi-wavelength studies of Markarian 501 during its quiescent state, due to its low luminosity. A short term multi-wavelength study of Markarian 501 was coordinated in March 2009 focused around a multi-day observation with the Suzaku X-ray satellite and including data from VERITAS, MAGIC, and Fermi-LAT with the goal of providing a well sampled multi-wavelength baseline measurement of Markarian 501 in the quiescent state. The results of these quiescent state observations are then compared to the historically extreme outburst of April 16, 1997 with the goal of examining variability of the spectral energy distribution between the two states. The derived broadband spectral energy distribution shows the characteristic double-peaked profile. We find that the X-ray peak shifts by over two orders of magnitude in photon energy between the two flux states while the TeV peak appears to vary little.

Blazars, a sub-class of active galactic nuclei (AGN), are the dominant extragalactic source class in γ -rays. They have been observed to show rapid variability and non-thermal spectra, presenting a broad continuum across nearly the entire electromagnetic spectrum. This implies that the observed photons originated within highly relativistic jets oriented very close to the observers line of sight [92]. The orientation results in Doppler beaming that boosts the intensity and frequency of the observed jet

emission, often overwhelming all other emission from the source. Therefore, blazars make excellent laboratories for studying the physical processes within the jets of AGN. They were among the first sources to be detected in the VHE band and as of 2010 there are 28 known VHE γ -ray blazars¹. Markarian 501 (Mrk 501; 1652+398), at a redshift of $z=0.034$ was the second blazar to be detected at TeV energies [81].

The spectral energy distribution (SED) of Mrk 501 characteristically shows a double peaked profile. These peaks occur at keV and TeV energies when plotted as $\nu F\nu$ vs ν . This structure is common among all VHE γ -ray blazars, and several models have been developed to account for the double peaked structure. These models attribute the peak at keV energies to synchrotron radiation from relativistic electrons and positrons within the blazar jets. The models differ in accounting for the source of the TeV peak. The models are generally divided into two classes: leptonic and hadronic, named for their attributed source for the TeV peak. The leptonic models advocate inverse Compton scattering to TeV energies of either the synchrotron photons from within the jet or an external photon field (e.g., [38, 68, 69, 88]). The hadronic models, however, account for the TeV emission by π_0 or charged pion decay with subsequent synchrotron and/or Compton emission from decay products, or synchrotron radiation from ultra-relativistic protons (e.g., [5, 67, 78]).

Observationally, Mrk 501 has been known to undergo both major outbursts on long time scales and rapid flares on short time scales, most prominently at keV and TeV energies (e.g., [30, 77, 95]). During these outbursts, both of the SED peaks have been observed to shift towards higher energies. During the most extreme cases, the keV peak has been observed above 200 keV. Historically, the SED has been measured in the VHE band primarily during outbursts, due to the lower sensitivity of the previous generations of instruments. This work attempts to provide state of the art short-term multi-wavelength measurements of the quiescent state of Mrk 501 with broad spectral coverage in the critical keV and TeV energy bands. These measurements are then compared to an extreme outburst of the source that was observed in 1997 [30, 77].

¹<http://tevcat.uchicago.edu/>

5.2 Data Selection and Analysis

5.2.1 Suzaku: X-ray

The Suzaku X-ray observatory, a collaborative project between institutions in the United States and Japan, is an excellent tool for studying the broadband spectral energy distribution (SED) of sources such as Mrk 501 due to its broad energy range (0.2 - 600 keV). Suzaku has two operating instruments for studying X-ray emission: the X-ray imaging spectrometer (XIS, [63]) and the hard X-ray detector (HXD, [91]). A third instrument, the X-ray Spectrometer malfunctioned after launch and is no longer operational.

The XIS instrument consists of four X-ray telescopes with imaging CCD cameras in their focal plane. Three of the CCDs are front illuminated, and one CCD is back illuminated to provide extended sensitivity to soft X-rays. The combined energy range of these CCDs is 0.2 - 12.0 keV. The HXD is a non-imaging instrument that expands the energy sensitivity of Suzaku to the 10 - 600 keV band by using two types of detectors. Silicon PIN diodes provide sensitivity in the range 10 - 70 keV, and GSO scintillators placed behind the PIN diodes provide sensitivity in the range 40 - 600 keV. One limitation of Suzaku with respect to attaining simultaneous multi-wavelength observations is that it resides in a low earth orbit, so observations are subject to frequent earth occultations, limiting continuous temporal coverage.

Observations of Mrk 501 were carried out with the Suzaku X-ray satellite from 2009-03-23 UT 18:39 to 2009-03-25 UT 07:59 (sequence number 703046010). After good time interval selection and dead time correction, a total of approximately 72 ks of live time remained for the XIS and 61 ks for the HXD. To reduce the occurrence of photon pile up in the XIS, a common problem when dealing with bright X-ray point sources, the following precautions were taken. The XIS observations were carried out in 1/4 window mode and Suzaku was operated with a pointing nominally centered on the HXD field of view. In addition, HXD nominal pointing increases the effective area of the HXD instrument. The resulting XIS count rates are well below the threshold

where pile up becomes a significant issue. Even with the HXD nominal pointing, there was no significant detection in the GSO scintillators, so the maximum useful energy for these observations using only the HXD/PIN detector was around 70 keV.

The raw XIS data were reprocessed following the guidelines from the Suzaku team² using Suzaku software version 12.0. The events were graded and only those with ASCA grades 0, 2, 3, 4 and 6 were included in further analysis. In addition, the data was screened to exclude times when the Suzaku spacecraft was passing through the South Atlantic Anomaly, including a 436 seconds buffer to allow the instrument's background to settle. Additional cuts were made requiring the data used to be taken at least 5° in elevation above the Earth's limb and at least 20° above the Earth's daytime limb. These cuts help reduce contamination from the Earth's atmosphere.

Source events were extracted from a circular region with a radius of 1.92' centered on Mrk 501. Background events were extracted from a circular region with the same radius located far from the source in each XIS detector. The redistribution matrix file (RMF) and ancillary response files (ARF) were generated for each XIS using the analysis tools included in the Suzaku analysis package.

The HXD data was also reprocessed from the raw files, following the guidelines provided by the Suzaku team.³ The data were filtered with similar criteria as the XIS data with a slightly longer settling time of 500 s required since passage through the South Atlantic Anomaly. In addition, the only elevation requirement was for data to be taken at least 5° above the Earth's limb.

Because the HXD is a non-imaging instrument, the cosmic X-ray background (CXB) and instrumental non X-ray background (NXB) must be accounted for in different ways than the XIS. The time-variable non X-ray background has been modeled and provided by the HXD team. The cosmic X-ray background is not included in this model and must be accounted for separately as the CXB flux is about 5% of the background for PIN observations. The model suggested by the HXD team is based

²<http://heasarc.gsfc.nasa.gov/docs/suzaku/analysis/abc/node9.html>

³http://heasarc.gsfc.nasa.gov/docs/suzaku/analysis/hxd_repro.html

on results from HEAO-1 and modified for input to XSPEC that reproduces the PIN background with an HXD nominal pointing [20]. The model is shown in Equation 5.1.

$$\frac{dF}{dE} = 8.0 \times 10^{-4} \left(\frac{E}{1 \text{ keV}} \right)^{-1.29} \times \exp \left(\frac{-E}{40 \text{ keV}} \right) \text{ photons cm}^{-2}\text{s}^{-1} \text{ FOV}^{-1} \text{ keV}^{-1} \quad (5.1)$$

The CXB background model was added to the NXB background model and used to subtract background events in XSPEC during spectral analysis of the PIN data.

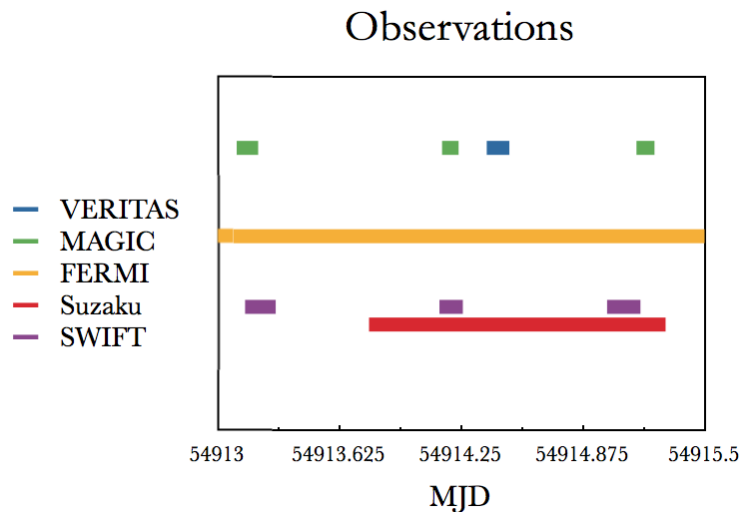


Figure 5.1. Time coverages of Mrk 501 by the instruments involved in the multi-wavelength campaign. Data gaps due to orbital constraints are not indicated.

5.2.2 VERITAS: VHE γ -ray

The Very Energetic Radiation Imaging Telescope Array System (VERITAS) is an array of four imaging air Cherenkov telescopes (IACTs) located at the Fred Lawrence Whipple Observatory in southern Arizona (31°40' 30"N, 110°57' 07"W) at an altitude of 1280m. These telescopes detect the Cherenkov light emitted by extensive air

showers that are initiated in the upper atmosphere by γ -rays and cosmic rays using imaging cameras consisting of 499 PMTs located in the focal plane of each telescope. VERITAS is sensitive in the range of approximately 100 GeV – 30 TeV. Images of the extensive air showers captured by each telescope can be combined to reconstruct the direction and energy of the shower initiator using *Monte Carlo* simulations of showers and the response of the array. The telescopes typically operate in “wobble mode,” where the location of the object to be observed is offset from the center of the field of view by 0.5° , allowing for simultaneous background measurements. The offset direction alternates between N, S, E and W for each data run (typically lasting 20 minutes) to reduce systematic effects from the offset.

The VERITAS data was analyzed using the standard VEGAS analysis package. Images of the Cherenkov light produced by the extensive air showers are parameterized, and standard quality cuts are placed on the data to ensure that the shower reconstruction procedure can be performed reliably. Separation of showers initiated by γ -ray photons from hadronic showers initiated by cosmic rays is performed with the aid of lookup tables generated similarly to the method used for the energy estimate. The lookup tables are calculated for each telescope with several values of zenith angle, azimuth angle, and the night sky background noise level. The observed parameters *length* and *width* are scaled by the corresponding parameters in the lookup tables and averaged among the telescopes to find the “mean scaled parameters” in the method first suggested by [36]. Standard cuts for γ /hadron separation (optimized on Crab data) are placed on the mean scaled parameters of the shower images to exclude most hadronic showers while still retaining a large number of γ -ray initiated showers.

To perform a background subtraction of the surviving cosmic-ray events, an estimation of these background counts is made using the “reflected region” background model. Events within a squared angular distance of $\theta^2 < 0.0169$ of the anticipated source location are considered ON events. Background measurements (OFF events) are taken from regions of the same size and at the same angular distance from the center of the field of view. For this analysis, 9 background regions were used. The

excess number of events from the anticipated source location is taken by subtracting the number of OFF events (scaled by the relative exposure) from the ON events. Statistical significances are calculated using the methods of [64]. More details of VERITAS, the calibration and analysis techniques can be found in [4].

On March 24 2009 (MJD 54914), VERITAS took data on Mrk 501 while operating in *wobble* mode, with an offset angle of 0.5° . VERITAS observed Mrk 501 for 2.6 hours from 9:11 UT to 11:58 UT using a series of 20 minute runs, with a live time of 2.4 hours. The data were processed using standard VERITAS analysis cuts, and the total significance for this observation was 12.7σ with an average significance per run of 3.8σ .

5.2.3 MAGIC: VHE γ -ray

MAGIC is a system of two Imaging Atmospheric Cherenkov Telescopes (IACTs) for very high energy gamma-ray astronomy located on the Canary Island of La Palma (2200m above sea level, $28^\circ 45' \text{N}$, $17^\circ 54' \text{W}$). At the time of the observation, MAGIC-II, the new second telescope of the current array system, was still in its commissioning phase so that Mrk 501 was observed by MAGIC-I in stand-alone mode.

MAGIC-I has a 17 m diameter tessellated reflector dish and a hexagonally-shaped camera with a Field of View (FoV) of 3.5° mean angular diameter. The camera comprises 576 high-sensitivity photomultiplier tubes (PMTs) of variable diameter (0.1° in the inner part and 0.2° in the outer part). The trigger threshold of MAGIC at low zenith angles is between 50 and 60 GeV with the standard trigger configuration (which was the one used in this campaign). The accessible energy range extends up to tens of TeV with a typical energy resolution of 20% to 30%, depending on the zenith angle and energy. Further details, telescope parameters, and performance information can be found in [10].

The MAGIC data for this campaign were recorded on the night of March 23, 2009 (MJD 54913), between 3:50 UT – 5:10 UT. The observations were performed in the

so-called “wobble” mode [36]. The zenith angle of the observations ranges from 15° to 30° . The recorded data fulfill the standard quality requirements during all the observation time, so that none of the runs have been removed from the data sample. The total live time is 1.27 h.

The data were analyzed using the MAGIC standard calibration and analysis [10]. The analysis is based on image parameters [12, 54] and the random forest (RF, [9]) method, which are used to define the so-called hadronness of each event. The cut in Hadronness for background rejection was chosen using *Monte Carlo* data, setting a cut efficiency for gamma rays of 70%. Three background (OFF) sky regions are used for the residual background estimation. They are chosen symmetrically to the ON-source region with respect to the camera center. The excess of events from the source was extracted from the distribution of the ALPHA parameter, which is related to the image orientation on the camera [54]. The final cut on —ALPHA— was also chosen using *Monte Carlo* gammas imposing again a cut efficiency of 70%. With these loose cuts, suitable for the spectrum calculation, the significance of the excess is of 2.2 sigma whereas applying hard cuts in the optimal energy range for signal detection, the significance is 9.7 sigma.

The energies of the gamma-ray candidates were also estimated using the RF method [9]. A minimum cut of 100 photoelectrons was applied on the SIZE image parameter, resulting in an energy threshold for the analysis of 100 GeV (defined as the peak position of the distribution of the reconstructed energy parameter for simulated gammas after the cut).

5.2.4 Fermi: γ -ray ($20 \text{ MeV} < E < 300 \text{ GeV}$)

The Fermi/LAT is an instrument to perform γ -ray astronomy above 20 MeV. The instrument is an array of 4×4 identical towers, each one consisting of a tracker (where the photons get pair-converted) and a calorimeter (where the energy of the pair-converted photons is measured). The entire instrument is covered with an an-

ticoincidence detector to reject charged-particle background. The LAT has a large peak effective area (0.8 m^2 for 1 GeV photons), an energy resolution typically better than 10%, and a field of view (FoV) of about 2.4 sr with an angular resolution (68% containment angle) better than 1 degree for energies above 1 GeV. Further details on the description of LAT can be found in [16]

The analysis was performed with the ScienceTools software package version v9r15p2, which is available from HEASARC. Only events having the highest probability of being photons, those in the “diffuse” class, were used. The LAT data were extracted from a circular region of 10° radius centered at the location of Mrk 501. The spectral fit was performed using photon energies greater than 0.3 GeV in order to minimize systematics, and a cut on the zenith angle ($> 105^\circ$) was also applied to reduce contamination from the Earth albedo γ -rays, which are produced by cosmic rays interacting with the upper atmosphere.

The background model used to extract the gamma-ray signal includes a Galactic diffuse emission component and an isotropic component⁴. The isotropic component includes contributions from the extragalactic diffuse emission as well as from residual charged particle backgrounds. The spectral shape of the isotropic component was derived from residual high latitude events after the Galactic contribution had been modeled. To further reduce systematic uncertainties in the analysis, the normalization and spectral parameters in the background model were allowed to vary freely during the spectral point fitting. The spectral fluxes were determined with the post-launch instrument response functions P6_V3_DIFFUSE using an unbinned maximum likelihood method [71].

⁴<http://fermi.gsfc.nasa.gov/ssc/data/access/lat/BackgroundModels.html>

5.2.5 Results

Light Curves

Light curves were produced in the passing band of each instrument involved in the campaign (except the LAT which did not have enough statistics for a meaningful light curve) to understand the flux levels and variability of Mrk 501 during the course of this campaign. The resulting multi-wavelength light curves with best fit values for constant flux are shown in Figure 5.2.

Light curves produced from the XIS and HXD/PIN Suzaku data are shown in the top two panels of Figure 5.2. Individual light curves for each of the XIS detectors were created and then summed to gain an understanding of the variability in the 0.6 - 10.0 keV range. The best fit constant value for the summed XIS light curve found a value of 16.14 cts s^{-1} with a χ^2 of 4207 for 26 degrees of freedom. The poor fit to a constant corresponds to the moderate variability that is visible by inspection in the XIS count rate. The HXD/PIN light curve was also fit to a constant of 0.11 cts s^{-1} with a χ^2 of 43.7 for 26 degrees of freedom, again indicating variability.

In the VHE γ -ray band, the source appears to be in a “quiet” state when compared to a contemporaneous long term study of the source’s broadband behavior [1,46]. The light curves produced from the VERITAS and MAGIC data used 20 minute time bins and are plotted in the bottom panel of Figure 5.2. To produce light curves, the spectral slope from the corresponding data is assumed, and the effective collection areas were used with the excess counts to determine the spectral normalization. An energy threshold of 300 GeV was then used to calculate the integral flux for each bin. A constant flux value was fit to the data, finding a best fit value of $3.08 \times 10^{-11} \text{ photons cm}^{-2} \text{ s}^{-1}$ with $\chi^2 = 9.96$ for 11 degrees of freedom, indicating that the source does not show large scale variability in VHE γ -rays during these observations.

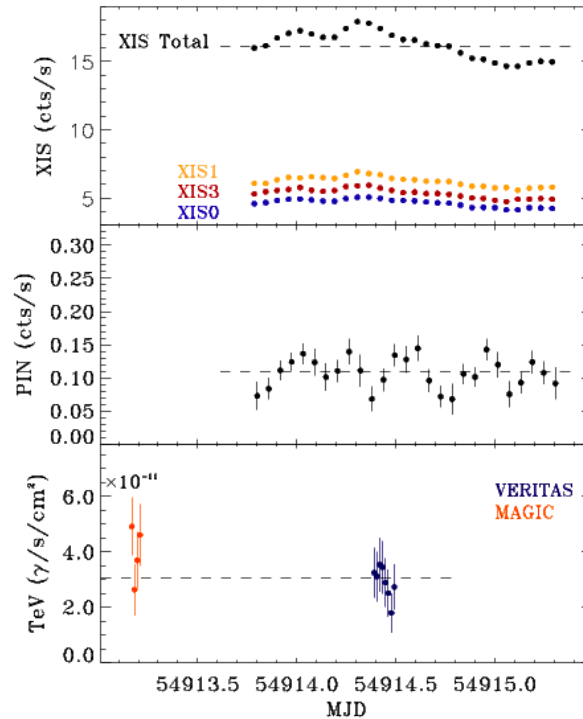


Figure 5.2. Light curves of Mrk 501 in the passing band of Suzaku/HXD, Suzaku/XIS, MAGIC and VERITAS.

Spectral Analysis

The spectral results for the observations taken during this campaign when Mrk 501 was in the quiescent or low flux state are shown in Figure 5.5 along with archival data from [77] and [30] taken when Mrk 501 was in a high flux state.

The data from all Suzaku instruments were fit jointly in XSPEC 12 [15]. A cross-normalization parameter was introduced to account for the calibration differences between the individual XIS detectors and the HXD/PIN. A broken power law modified by interstellar absorption with a fixed column density $n_H = 1.73 \times 10^{20}$ [89] was fit to the data, finding power law indices $\Gamma_1 = 2.133 \pm 0.003$, $\Gamma_2 = 2.375 \pm 0.009$, and a break energy of $E_{break} = 3.21 \pm 0.07$ keV. After the fitting procedure, the cross-normalization factors for the XIS1 and XIS3 detectors relative to the XIS0 detector are compatible with previous calibration measurements of the Crab nebula flux [86].

A fixed normalization factor of 1.18 was introduced between the HXD/PIN and XIS0 as specified by the Suzaku team for HXD nominal pointings [66]. The resulting fit, with $\chi_{red}^2 = 1.33$ for 1511 degrees of freedom, is plotted in Figure 5.3. After a good fit was found, the result was unfolded through the instrument response and de-absorbed to derive the intrinsic X-ray spectrum shown in Figure 5.5.

The Fermi/LAT spectral measurement shown in the broadband SED in Figure 5.5 was derived using a time interval of 7 days centered at the Suzaku observing time window – from MJD 54911 up to MJD 54918. Mrk 501 is detected with a Test Statistic (TS) value of 47 (~ 7 sigma). The spectrum can be fit with a single power law function with photon flux $F(> 0.3 \text{ GeV}) = (1.7 \pm 0.9) \times 10^{-8} \text{ photons cm}^{-2} \text{ s}^{-1}$ and differential photon spectral index $\Gamma_{LAT} = -1.7 \pm 0.3$. The number of photons (predicted by the model) for the entire spectrum is 12, out of which 9 are in the energy range 0.3-3 GeV, 2 in the energy range 3-30 GeV and 1 in the energy range 30-300 GeV. In order to increase the simultaneity of the reported SED, we also performed the analysis of the LAT data over a period of 3 days centered at the Suzaku observations, namely the time interval from MJD 54913 to MJD 54916. For such a short time interval the detection has a TS value of 10 (~ 3), and significantly larger error bars in the power law parameters: $F(> 0.3 \text{ GeV}) = (1.8 \pm 1.3) \times 10^{-8} \text{ photons cm}^{-2} \text{ s}^{-1}$, $\Gamma_{LAT} = -1.9 \pm 0.5$. Since the two spectral shapes are compatible within errors and there is no indication of flux variability during this time, in the SED plot in Figure 5.5 it was decided to use the spectrum derived with the 7-day time interval.

For the VERITAS spectral analysis, the spectrum was unfolded using effective collection areas for the array that were calculated using *Monte Carlo* simulations of extensive air showers passed through the analysis chain with a configuration corresponding to the data-taking conditions and applied γ /hadron selection cuts. The unfolding process takes into account the energy resolution of the array and potential energy bias. The effective areas are then used for each reconstructed event to calcu-

late the differential photon flux. The VHE γ -ray differential spectral points were fit with a simple power law of the form:

$$\frac{dN}{dE} = F_0 \times 10^{-12} \times \left(\frac{E}{1 \text{ TeV}} \right)^{-\alpha} \text{ photons cm}^{-2} \text{ s}^{-1} \text{ TeV}^{-1} . \quad (5.2)$$

For the VERITAS analysis, best-fit parameters of $\alpha = 2.72 \pm 0.15$ and $F_0 = 5.78 \pm 0.83$ were found. Quoted uncertainties are statistical only.

For the MAGIC analysis, the derived spectrum was unfolded to correct for the effects of the limited energy resolution of the detector [8] and of possible bias. The flux of Mrk 501 was on the order of 30% of the flux of the Crab Nebula during the observation. It was possible to obtain a significant gamma excess in four energy bins and compute the energy spectrum (SED) shown in Figure 5.5. Given the limited number of spectral points, the only conclusion that can be drawn with the MAGIC points alone is that the results are compatible with a simple power law function finding $\alpha = -2.67 + -0.21$.

After the completion of spectral analysis for the instruments used in this campaign, a simple synchrotron self-Compton (SSC) model⁵ was used to match the results with an emission scenario for illustrative purposes. This model assumes a spherical emission region of radius R with the emission Doppler-boosted by the factor:

$$D = [\Gamma(1 - \beta \cos \theta)]^{-1} , \quad (5.3)$$

where the blob is moving with Lorentz factor Γ towards the observer, β gives the bulk velocity of the plasma in terms of the speed of light, and θ is the angle between the jet axis and the line of sight in the observer frame. The emission region contains an isotropic non-thermal electron population and randomly oriented magnetic field, measured by B . The electron spectrum is assumed to be in the form of a broken power law with index p_1 between γ_{min} and γ_b and index p_2 between γ_b and γ_{max} . The code uses two models for gamma-ray absorption by the extragalactic background light [42, 60]. After computing the synchrotron and Inverse Compton emission, the

⁵The SSC code is available at <http://jelley.wustl.edu/multiwave>

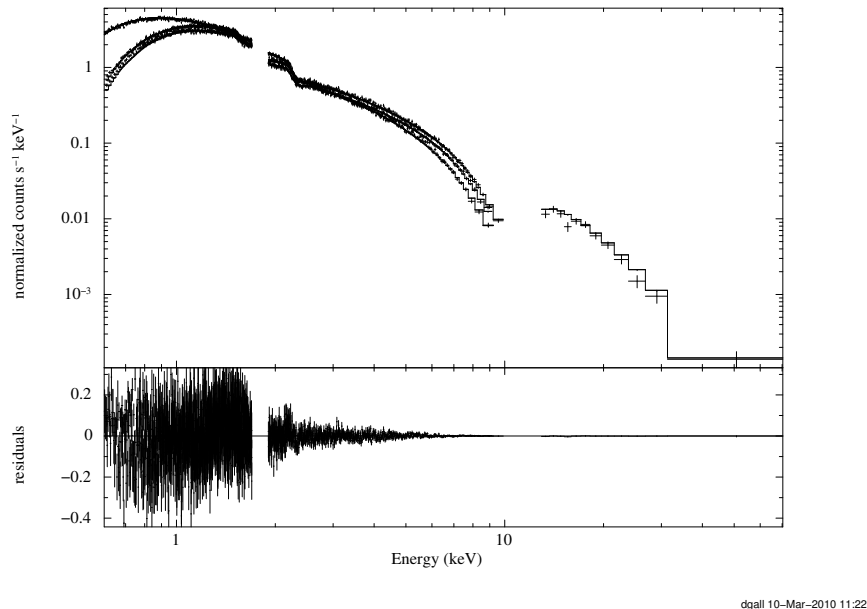


Figure 5.3. Observed X-ray spectrum of Mrk 501. They were made from the XIS and HXD/PIN data separately. The solid histogram shows the best fits to the data with a broken power-law model (see text). The bottom panel shows the residuals of the fit.

code corrects the photon spectrum that is produced for synchrotron self absorption and internal absorption due to pair production processes. The model does not evolve the electron spectrum self-consistently.

The parameters for the models used in this work for the 1997 high flux state and the 2009 low flux state are given in Table 5.1 along with model parameters from other works for comparison. The models are primarily included to illustrate the changes in overall SED shape indicate by the data; the matches to the data are not unique.

5.2.6 Discussion

This data set provides a high quality sampling of the broadband SED of Mrk 501 in the quiescent state, and it allows comparisons to be made over a broad energy range with the extreme outburst observed in 1997. In choosing the values for the SED model parameters, we attempted to be consistent with previous works in choosing

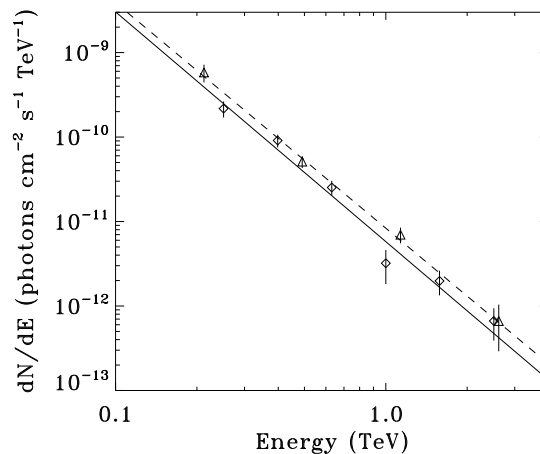


Figure 5.4. VHE spectrum from VERITAS (diamonds) and MAGIC (triangles), including the best fits power law models. VERITAS model shown with solid line, and MAGIC model shown with dashed line. The slopes of the power law models agree well, with a slight normalization offset, corresponding to the moderately higher TeV flux levels during the MAGIC observation.

Table 5.1
SED Model Comparisons

Data Set	γ_{min}	γ_{max}	γ_{break}	p_1	p_2	B (G)	R (cm)	D
Albert et al. (2007, Low flux)	1	5×10^6	10^5	2	3.2	0.31	1×10^{15}	25
Anderhub et al. (2009, Low flux)	1	1×10^7	6×10^4	2	3.9	0.313	1.03×10^{15}	20
Petry et al. (2000, Low flux)	500	3×10^7	-	2.4	-	0.05	3×10^{15}	30
Pian et al. (1998, Low flux)	3×10^3	6×10^5	-	2	-	0.8	5×10^{15}	15
Pian et al. (1998, High flux)	4×10^5	3×10^6	-	1	-	0.8	5×10^{15}	15
Sambruna et al. (2000, Low flux)	1	3.9×10^6	-	-	-	0.03	4×10^{16}	25
This work, 2009 Low flux state	1	3×10^6	7×10^4	1.4	3.6	0.34	1×10^{15}	20
This work, 1997 High flux state ^a	1	3×10^6	3×10^5	1.6	2.6	0.23	1×10^{15}	20

^aData from Pian et al. (1998)

γ_{min} , γ_{max} , B, R, and D while still matching the data (see Table 5.1). In addition, when applying the models to the data from the two states, we attempted to limit the differences to the electron spectral indices and break energy (γ_b), similar to [77] and [14], with a small shift in B included to provide a better match to the data. The

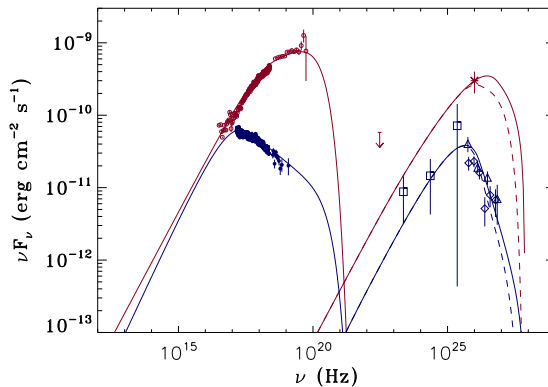


Figure 5.5. Spectral energy distributions of Mrk 501 in the quiescent state (in blue) and in an extreme outburst (in red). The former were made from data obtained in the present campaign with Suzaku (filled circles), Fermi (squares), VERITAS (diamonds), and MAGIC (triangles). The latter were taken from [77], with X-ray data from BeppoSAX (open circles), GeV gamma-ray upper limit from EGRET, and TeV γ -ray data from Whipple (star). Corresponding fits for each year are shown. The solid lines show the SSC fit, dotted lines take EBL absorption into account. The TeV data points are not EBL corrected.

resulting SSC models can reproduce the measured spectra from the keV to the TeV range for both the quiescent state and the 1997 outburst.

The main difference between the SED models matched to the data from the outburst and the quiescent state is in the spectrum of the electron population, implying that this may be the primary explanation for the dramatic shift in the peak frequency. Specifically, γ_b and the power law spectral index above the break appear to drive the changes. The SSC model matches indicate that during the high flux state the break energy is shifted an order of magnitude higher and that past the break energy the spectrum is significantly harder than in the low flux state. Again, it is important to note that the match of these models to the data is not unique due to the number of free parameters.

The X-ray data do not allow us to measure the location of the low energy SED peaks directly, but they can be used to place limits on the peak energies. From the X-

ray data points alone, the keV peak must be above 227 keV (5.49×10^{19} Hz) during the 1997 outburst and below 0.6 keV (1.45×10^{17} Hz) during the quiescent state. This means that with a change in flux of around one order of magnitude between the quiescent state and the 1997 outburst, the keV peak of the SED shifts in frequency by more than 2 orders of magnitude.

Contrasting this large shift, the TeV peak of the SED does not seem to shift in location as dramatically between the two states. The SED peak at TeV energies is better constrained with the 2009 data than that from 1997, but the SED models applied to the data imply that even with a dramatic shift in flux at TeV energies, the peak energy in the TeV range is stable compared to that in the keV range. This may be due to Klein-Nishina (KN) effects which reduce the cross section for scattering when dealing with electrons of high energy. To examine the possible KN effects, which become important above $h\nu \sim m_e c^2$ in the electron rest frame, we examined the energies of typical electrons from the model distributions.

From the 1997 SED model, the peak attributed to synchrotron radiation is located at 3.59×10^{19} Hz. The peak energy of the emission in the jet frame, taking the Doppler factor of 20 into account, is $E_{peak} \approx 7.42$ keV. From [85], it can be shown that for synchrotron radiation:

$$\gamma_e^2 \approx \frac{8E_{peak}m_e c}{3\pi q B \hbar}, \quad (5.4)$$

where γ_e is the characteristic Lorentz factor of the electrons contributing to the bulk of the X-ray emission and E_{peak} is the peak energy of the synchrotron model. This yields a value of $\gamma_e = 1.5 \times 10^6 (B/0.23 \text{ G})^{-1/2} (D/20)^{-1/2}$ for the 1997 outburst. For the 2009 model, the synchrotron emission model peaks at 2.24×10^{17} Hz, giving a peak energy in the jet frame of $E_{peak} \approx 46.27$ eV. This yields a value of $\gamma_e = 1.0 \times 10^5 (B/0.34 \text{ G})^{-1/2} (D/20)^{-1/2}$ for the 2009 measurements.

Using these electron energies, we can examine the importance of KN effects during the course of the two measurements. For the 1997 outburst, $\gamma_e h\nu_{peak} \approx 1.11 \times 10^4$ MeV, well above the electron rest mass energy of 0.511 MeV placing this model

scenario in the extreme KN range. For the 2009 quiescent state model, $\gamma_e h\nu_{peak} \approx 4.6$ MeV, moderately above the KN limit. The extreme energies involved during the 1997 outburst may indicate that the emission is piling up in the TeV range due to the reduced KN cross section.

The SED models also allow us to examine the characteristic cooling timescales of the synchrotron and inverse Compton processes that are assumed to be the sources of the keV and TeV emission, respectively. The synchrotron cooling timescale is shown by [85] to be:

$$\tau_{syn} \approx \frac{6\pi m_e c}{\sigma_T \gamma_e B^2}, \quad (5.5)$$

where σ_T is the Thompson cross section, U_B is the magnetic energy density, and γ_e is the characteristic Lorentz factor of the electrons contributing to the bulk of the X-ray emission. This timescale was calculated for both model scenarios using the electron energies discussed above.

The inverse Compton cooling timescale was also calculated for the models, fully taking into account KN effects using the method discussed in [22]. As discussed above, models for both sets of observations indicate that KN effects are present, so these effects were carefully included in the calculation. Using the parameters for the 1997 model, the synchrotron cooling timescale is comparable to the SSC cooling timescale. However, for the quiescent state model from 2009, the timescale for inverse Compton cooling is two orders of magnitude shorter than the synchrotron cooling timescale, indicating that for this model scenario radiative cooling is dominated by the SSC process. This may be a signature of the reduced KN cross section for scattering at higher energies. The cooling timescales are shown in Table 5.2 for comparison. In addition, all of the timescales calculated were comparable or less than the light crossing time for the modeled blobs, indicating that light travel time effects may dominate the light curve profiles.

Further intense multi-wavelength observations of the source, in conjunction with long term monitoring campaigns will continue to be important to understand the

Table 5.2
Cooling Timescales

Model	τ_{syn} (s)	τ_{SSC} (s)
2009 Low flux state	6.7×10^4	4.6×10^2
1997 High flux state	9.8×10^3	3.7×10^3

broad band nature of Markarian 501 and to shed light on the blazar phenomenon in general.

Acknowledgments. We would like to thank Elena Pian for providing the Bepposax data. This work was supported in part by NASA through grants NNX08AZ98G and NNX08AX53G. This research has made use of data obtained from the Suzaku satellite, a collaborative mission between the space agencies of Japan (JAXA) and the USA (NASA). The VERITAS research is supported by grants from the U.S. Department of Energy, the U.S. National Science Foundation and the Smithsonian Institution, by NSERC in Canada, by Science Foundation Ireland and by STFC in the UK. We acknowledge the excellent work of the technical support staff at the FLWO and the collaborating institutions in the construction and operation of the instrument.

6. Summary and Future Work

The understanding of the the broadband nature of the emission from AGN is an important problem in astrophysics. Obtaining high quality multi-wavelength data, ideally simultaneous, is critical to putting meaningful constraints on the emission models that are currently used to explain the observed emission.

The study performed on Markarian 421 provided a new set of strictly simultaneous multi-wavelength data to investigate possible correlations between the X-ray and VHE γ -ray emission. The results are more reliable than those based on non-simultaneous observations. The possible correlation between X-ray and UV data, as well as the lack of correlation between X-ray and TeV data is intriguing, and is a potential area for further investigation. It will be important for future studies to obtain larger quantities of data with a larger dynamical range to continue to gain more insight into the nature of any correlations that may be present.

Our investigation of the quiescent state of Markarian 501 will provide a well sampled baseline for future observations, and when combined with observations of the source during outburst, could provide insight into the emission mechanism through multi-wavelength correlation searches and examining the changes observed in the broadband SED.

Future

New VHE γ -ray blazars continue to be discovered, now aided by discoveries by the Fermi γ -ray space telescope at lower energies. It will be important to expand the number of source that can be observed and studied in depth at multiple wavelengths. The personality demonstrated by the two sources studied here indicate that observations of many targets must be undertaken in order to more deeply understand

blazars in general. With over 800 blazars detected by Fermi, population studies of these sources are now possible.

These new targets must be observed simultaneously at multiple wavelengths to continue to place constraints on the emission models and to attempt to understand the nature of blazars in general. In addition to the use of current X-ray satellites and the Fermi γ -ray satellite, a new generation of IACTs will increase our sensitivity to the emission from these distant sources. The next generation of IACTs is currently under development through two collaborations, AGIS, primarily based in North America, and CTA, mostly consisting of European collaborators. These experiments, when completed, will improve on the sensitivity of current IACTs by an order of magnitude, allowing them to participate in detailed variability and spectral studies of blazars too weak for the current generation.

LIST OF REFERENCES

LIST OF REFERENCES

- [1] Abdo et al., 2010, in preparation
- [2] Acciari, V. A., et al., 2010, in preparation
- [3] Acciari, V. A., et al., 2009, ApJ, 703, 169
- [4] Acciari, V. A., et al., 2008, ApJ, 679, 1427
- [5] Aharonian, F. A. 2000, NewA, 5, 377
- [6] Aharonian, F. A., et al., 2006, A&A, 457, 899
- [7] Aharonian, F. A., et al. 2009 ApJ, 696, L150
- [8] Albert, J., et al. (MAGIC collab) 2007, Nucl. Instrum. Methods Phys. Res. A583, 494
- [9] Albert, J., et al. (MAGIC Collab.) 2008, Nucl. Instr. Meth., A558, 424
- [10] Albert, J., et al. (MAGIC collab) 2008, ApJ, 674, 1037
- [11] Albert, J., et al. (MAGIC collab) 2009, A&A, 493, 467
- [12] Aliu, E., et al. (MAGIC collab), 2009, Astropart. Phys. 30, 293
- [13] Anderhub, H., et al. (MAGIC collab) 2009, A&A (in preparation)
- [14] Anderhub, H., et al. (MAGIC Collab.), 2009, ApJ, 705, 1624
- [15] Arnaud, K.A., 1996, Astronomical Data Analysis Software and Systems V, eds. Jacoby G. and Barnes J., p17, ASP Conf. Series volume 101
- [16] Atwood, W. B., et al. 2009, ApJ, 697, 1071
- [17] Baixeras, C., et al. (MAGIC collab) 2004, Nucl. Instrum. Method., A588, 494
- [18] Berge, D., Funk, S., & Hinton, J. 2007, A&A, 466, 1219
- [19] Błażejowski, M., et al., 2005, ApJ, 630, 130
- [20] Boldt, E., 1987, IAUS, 124, 611B
- [21] Böttcher, M., & Chiang, J. 2002, ApJ, 581, 127
- [22] Böttcher, M., et al. 1997, A&A, 324, 395
- [23] Breiman, L. 2001, Machine Learning, 45, 5

- [24] Bradbury, S.M., & Rose, H. J., 2002, Nuclear Inst. and Methods in Phys. Research A, 481, 521
- [25] Bretz, T. (MAGIC collab) 2005, Proc. of the 29th ICRC, Pune, India, 4, 315
- [26] Bretz, T., & Dorner, D. 2008, AIP Conf. Proc. Vol. 1085, 664
- [27] Brinkmann, W., et al., 2001, A&A, 365, L162
- [28] Cardelli, J. A., et al., 1989, ApJ, 345, 245
- [29] Carroll, B. W., & Ostlie, D. A., 1996, An Introduction to Modern Astrophysics (Reading, MA: Addison-Wesley)
- [30] Catanese et al., ApJ 487,L143, 1997
- [31] Cherenkov, P., 1937, Phys. Rev., 52, 378
- [32] Cogan, P., et al. 2007, ArXiv e-prints, arXiv:0709.4233
- [33] Cogan, P., 2006, Ph.D. Thesis, University College Dublin
- [34] Cortina, J., et al. (MAGIC collab) 2005, Proc. of the 29th ICRC, Pune, India, 5, 359
- [35] Cui, W. 2004, ApJ, 605, 662
- [36] Daum, A., et al., 1997, Astropart. Phys., 8, 1
- [37] Davies, J. M., & Cotton, E. S., 1957, Journal of Solar Energy, 1, 16
- [38] Dermer, C. D., Schlickeiser, R., & Mastichiadis, A. 1992, A&A, 256, L27
- [39] Fath, Edward A., 1909. "The spectra of some spiral nebulae and globular star clusters." Lick Observatory Bulletin, 5, 71
- [40] Fomin, V. P., et al., 1994, Astropart. Phys., 2, 137
- [41] Fossati, G., et al., 2008, ApJ, 677, 906
- [42] Franceschini, A., et al., 2008, A&A, 487, 837F
- [43] Frank, I., & Tamm, I., 1937, Dokl. Akad, SSSR 14, 109
- [44] Gabriel, C., et al., 2004, in Astronomical Society of the Pacific Conference Series, Vol. 314, Astronomical Data Analysis Software and Systems (ADASS) XIII, ed. F. Ochsenbein, M. G. Allen, & D. Egret, 759
- [45] Gaidos, J. A., et al., 1996, Nature, 383, 319
- [46] Huang, et al. (VERITAS Collab.), 2009, in 2009 Fermi Symposium, Washington, D.C., edited by W. N. Johnson and D. J. Thompson, eConf C0911022, [arXiv:0912.3772]
- [47] Hubble, Edwin P., 1926, ApJ, 64, 321
- [48] Galbraith, W., & Jelley, J.V., 1953, Nature 171, 349

- [49] Gaug, M., Bartko, H., Cortina, J., & Rico, J. (MAGIC collab) 2005, Proc. of the 29th ICRC, Pune, India, 5, 375
- [50] George, I. M., et al., 2007, "The Calibration Requirements for Spectral Analysis (Definition of RMF and ARF file formats)", OGIP Calibration Memo CAL/GEN/92-002
- [51] Ghisellini, G. et al., 1996, A&AS, 120, 503
- [52] Ginzburg, V. L., & Syrovatskii, S. I., 1969, ARA&A, 7, 375
- [53] Hall, J., et al., 2003, Proc. of the 28th ICRC, Tsukuba, Japan
- [54] Hillas, A. M. 1985, Proceedings of the 19th ICRC
- [55] Jansen, F. et al., 2001, A&A, 365, L1
- [56] Jelley, J. V. 1958, "Cerenkov Radiation and its Applications," Pergamon Press
- [57] Kelley R. L., et al., 2006, Suzaku Memo, <http://www.astro.isas.jaxa.jp/suzaku/doc/suzakumemo/suzakumemo-2006-38.pdf>
- [58] Kildea, J., et al., 2007, Astropart. Phys., 28, 182
- [59] Kirk, J. G., & Mastichiadis, A. 1999, Astropart. Phys., 11, 45
- [60] Kneiske, T. M., Mannheim, K., & Hartmann, D. H. 2002, A&A, 386, 1
- [61] Kokubun, M., et al., 2007, PASJ, 59, S53
- [62] Konopelko, A., 1995, in Proc. of the Padova Workshop on TeV Gamma-Ray Astrophysics "Towards a Major Atmospheric Cerenkov Detector-IV," (ed. M. Cresti), 373
- [63] Koyama, K., et al., 2007, PASJ, 59, S23S33
- [64] Li, T.-P., & Ma, Y.-Q. 1983, ApJ, 272, 317
- [65] Longair, M., 2004, "High Energy Astrophysics. Vol. 1 Particles, photons and their detection - 2nd ed," Cambridge University Press
- [66] Maeda et al., 2008, JX-ISAS-SUZAKU-MEMO-2008-06, Recent update of the XRT response. III. Effective Area Category: XRT, XIS, HXD
- [67] Mannheim, K. 1993, A&A, 269, 67
- [68] Maraschi, L., et al., 1992, ApJ, 397, L5
- [69] Marscher, A. P., & Gear, W. K. 1985, ApJ, 298, 114
- [70] Mason, K. O., et al., 2001, A&A, 365, L36
- [71] Mattox, J. R., et al. 1996, ApJ, 461, 396243
- [72] McCann, A., et al., 2009, Astropart. Phys., 32, 325
- [73] Millis, J. P., 2008, Ph.D. Thesis, Purdue University

- [74] Mitsuda, K., et al., 2007, PASJ, 59, S1S7
- [75] Mohanty, G., et al., 1998, *Astropart. Phys.*, 9, 15
- [76] Nagai, T., et al., 2007, Proc. of the 30th ICRC, Merida, Mexico
- [77] Pian et al., *ApJ* 492, L17, 1998
- [78] Pohl, M., & Schlickeiser, R. 2000, *A&A*, 354, 395
- [79] Punch, M., et al., 1991, Proceedings of the 22nd ICRC
- [80] Punch, M., et al., 1992, *Nature*, 358, 477
- [81] Quinn, J., et al. 1996, *ApJ*, 456, L831
- [82] Reynolds P. T., et al., 1993, *ApJ*, 404, 206
- [83] Riegel, B., et al. (MAGIC collab) 2005, Proc. of the 29th ICRC, Pune, India, 5, 215
- [84] Roache, E., et al., 2007, Proc. of the 30th ICRC, Merida, Mexico, 3, 1397
- [85] Rybicki, G. B., & Lightman, A. P., 1979, *Radiative Processes in Astrophysics* (New York: Wiley)
- [86] Serlemitsos, P. J., et al. 2007, PASJ, 59, 9
- [87] Seyfert, Carl K., 1943, *ApJ*, 97, 28
- [88] Sikora, M., Begelman, M. C., & Rees, M. J. 1994, *ApJ*, 421, 153
- [89] Stark, A. A., et al. 1992, *ApJS*, 79, 77
- [90] Strüder, L., et al., 2001, *A&A*, 365, L18
- [91] Takahashi, T., et al., 2007, PASJ, 59, 35
- [92] Urry, C. M., & Padovani, P. 1995, *PASP*, 107, 803
- [93] Weekes, T. C., et al., 1989, *ApJ*, 342, 379
- [94] Weekes, T. C., et al., 1988, *Physics Reports*, 160, 1
- [95] Xue, Y., & Cui, W., 2005, *ApJ*, 622, 160
- [96] Xue, Y., Yuan, F., & Cui, W. 2006, *ApJ*, 647, 194

APPENDICES

A. VERITAS Analysis Pipeline Automation

A.1 Introduction

The installation and automation of the VERITAS analysis pipeline using the VEGAS software package (see Section 3.2.2) is described here in more detail. Two scripts were developed as part of this dissertation work: vaPipe and vaMProc. The script vaPipe automates the process of downloading archived data and the initial stages of VEGAS in order to streamline the analysis procedure. The vaMProc script handles the balancing of analysis processes among a user specified number of processors in a multi-core system. This appendix describes the current structure of the installation of the VEGAS package and outlines some basic analysis procedures. All file system references refer to the current installation of VEGAS on `uranus.physics.purdue.edu`. More details concerning the installation of the VEGAS package can be found at the VERITAS offline analysis working group website.¹

A.2 Filesystem

A.2.1 ROOT

The ROOT package is the analysis framework used in the VEGAS package. Multiple versions of ROOT are installed in:

`/usr/local/src`

These installations are sorted into directories using the root version, such as:

¹http://veritas.sao.arizona.edu/OAWGwiki/index.php/Getting_Started

root-5-18-00/

root-5-22-00/

root-5-24-00/

A.2.2 VEGAS

Multiple versions of VEGAS are installed in:

/usr/local/veritas/

with the naming convention as follows:

vegas2.0.5/

vegas2.1.3/

A.2.3 Data Files

On uranus, all data files are stored in:

/veritas/VData/

The stage 4 reduced files are stored in:

/veritas/VData/DST/

in subdirectories that are (hopefully) usefully named.

A.2.4 Configuration Files and Lookup Tables

On uranus, configuration files for different versions of vegas and different analysis requirements are located in:

```
/usr/local/veritas/configfiles/
```

There are subdirectories for different VEGAS versions and analysis requirements. You are encouraged to create your own directory and configuration files within this directory structure for analysis. Please do not change existing configuration files unless they are your own.

A.3 Initial Configuration

Before using VEGAS, you must specify which versions of VEGAS and ROOT to use and correctly set a number of system variables. A set of configuration scripts has been created to automate this process. These scripts are located in:

```
/usr/local/veritas/src
```

You must call one of these scripts to configure the system variables for the VEGAS and ROOT environments. The scripts are named by the version of VEGAS that they load. Alternatively, you can create your own custom script. To call them, you would use, for example:

```
> source /usr/local/veritas/src/vegas/vainit2.1.3.sh
```

They will display the following (for example) when called:

```

> source /usr/local/veritas/src/vainit2.1.3.sh
Using VEGAS version 2.1.3 and ROOT 5.24
setting up VEGAS environment ...
setting up VERITAS CVS environment ...
setting up ROOT environment
You are all set ...
>

```

It can be useful to set an alias in your `.profile` or `.bashrc` to simplify the process of running the configuration scripts. For example, the following lines could be added:

```

alias vegas205="source /usr/local/veritas/src/vainit2.0.5.sh"
alias vegas213="source /usr/local/veritas/src/vainit2.1.3.sh"
alias vegashead="source /usr/local/veritas/src/vainithead.sh"

```

This would allow a user to run the `vainit2.0.5.sh` configuration script by simply typing `vegas205` in the command line.

A.4 vaMProc

vaMProc is a script that was created to run VEGAS stage 1 - 4.2 analysis on multiple processors simultaneously. It has three required arguments: a runlist, an output directory, and a config directory.

The runlist should be located in the directory from which you are running vaMProc and formatted as follows:

```
date runNumber laserNumber
```

Example:

```
20071014 37195 37177
```



```
20071015 37230 37228
20071016 37266 37263
20071017 37297 37296
20071114 37945 37955
20071114 37946 37955
20071114 37947 37955
20071114 37948 37955
20071114 37949 37955
20071114 37950 37955
```

This is the default output of the VERITAS Run Log Generator². You must click on the link in the line that says, "Click here for simple run list format for scripts (this page must fully load first)." Also, make sure you have a carriage return after the last data run, or vaMProc will not read the last file in your list.

The output directory is a subdirectory of `/veritas/VData/DST`. If the directory does not exist, it will be created for you. The config directory is a subdirectory of `/usr/local/veritas/configfiles/` and needs to contain all the configuration and cuts files, using the standard names as well as a subdirectory, `tables`, with the lookup tables for stages 4 and 6 and a star list for exclusion regions.

For example, if you ran:

```
> vaMProc runlist.txt CRAB 2.0.5/1CrabSP
```

the script would use the file `runlist.txt` in the directory where the command was executed and use `/veritas/VData/DST/CRAB/` as an output directory. The config-

²<http://veritasm.sao.arizona.edu/DQM/loggen.html>

uration files would be read from `/usr/local/veritas/configfiles/2.0.5/1CrabSP`.

When you run `vaMProc` (and use the date formatted runlists), it will first attempt to download the runs that have not yet been downloaded. If the runs have been downloaded already, it will print `FILE EXISTS` for each run. Next, `vaMProc` analyzes the laser files. Finally, it will send analysis jobs to each processor and return to the command prompt. **DO NOT CLOSE THIS WINDOW UNTIL ALL PROCESSES HAVE COMPLETED!** Though nothing will show up on your window, the jobs have been submitted and will process in the background. You can use `“top -U [username] ”` to check the status of the analysis.

`vaMProc` splits the runlist into a list for each processor. When `vaMProc` runs, it will create a directory called `”vamp”` that contains each of these split lists and a log of the VEGAS stages for each list. If you would like to watch the progress of the analysis, a log can be displayed in the terminal using this command, for example:

```
> tail -f vamp/vaMProc2.log
```

This will show the log file in the terminal window and update it as the analysis progresses. You can also search the log files for errors after all of the analysis has been completed. `vaMProc` will also create a runlist that you can use in stage 6 called `s6runlist.txt`.

If for some reason you need to stop the analysis jobs, run:

```
> killall vaStage1 vaStage2 vaStage4.2
```

until it states that no processes can be found.

usage:

```
> vaPipe [-stages] [input runlist] [output sub-dir] [config sub-dir]
```

where [input runlist] should be in your working directory and is formatted as follows,

```
for wobble: run runNumber laserNumber -or- date runNumber laserNumber
```

for pair:

```
pair onNumber offNumber laserNumber
```

This script will process a list of runs on multiple processors simultaneously. The inputs are the same as vaPipe. It will split your runlist into X number of runlists, one for each processor. The log files for each processor will be created in a subdirectory called "vamp" in your working directory as well as a stage 6 runlist.

Runlist format is slightly different for vaMProc. If you format your runlist as:

```
run 666 667
```

it will assume that the files already exist on uranus.

If you format your runlist as:

```
20080621 666 667
```

it will search for the file and if it is not found, it will download it into /veritas/VData.

When you run vaMProc (and use the date formatted runlists), it will first attempt to download the runs that have not yet been downloaded. If the runs have been downloaded already, it will print FILE EXISTS for each run. Next, vaMProc analyzes the laser files. Finally, it will send vaPipe jobs to each processor and return the command prompt. Though nothing will show up on your window, the jobs have been submitted and will process in the background. You can use "top -U [username]" to check the status of the analysis.

If for some reason you need to stop the analysis jobs, run: `uranus$ killall vaStage1 vaStage2 vaStage4.2` until it states that no processes can be found.

At this time, you must leave the window that you started vaMProc from open or the jobs will crash. Please let me know if you have any questions. dgall@physics.purdue.edu

A.5 vaPipe

usage:

```
> vaPipe [-stages] [input runlist] [output sub-dir] [config sub-dir]
```

where [input runlist] should be in your working directory and is formatted as follows,

for wobble: run runNumber laserNumber -or- date runNumber laserNumber

for pair:

pair onNumber offNumber laserNumber

Note: vaPipe will look for the files in /veritas/VData for data runs

[output sub-dir] is a subdirectory of /veritas/VData

[config sub-dir] is a subdirectory of /usr/local/veritas/

Currently we are using Ben's cuts, "ZCuts" Type 'standard' to use the standard settings, 'simulation' for simulated runs, or feel free to create your own directory and config files, just be sure to name your config and cut files in the format of the other directories.

A.6 vaPipe: Code

```
#!/bin/bash
```

```
#vegasPipe:
```

```
#This script processes a list of runs from  
#a text file through stages 1-4 of VEGAS.
```

```
#VEGAS code should be installed in CODEDIR  
#which is set below.
```

```
#All vbf and cvbf data file should be kept  
#in the directory set as VBFDIR below.
```

```
#Configuration files should be kept in  
#sub-directories of the directory set in  
#CONFIGDIR.
```

```
#Data will be output in sub-directories of  
#the main directory set in OUTPUTDIR.
```

```
#Run as:
```

```
#vaPipe [-stages] <input runlist> <output sub-dir> <config sub-dir>
```

```
#Default is to process stages 1-4.
```

```
STAGES=s124
```

```
#=====#  
#DO NOT MAKE ANY CHANGES BELOW THIS POINT#  
#=====#
```

```

if [ "$1" = "-1" ]; then
    echo "#####"
# ATTENTION: Processing through Stage 1 ONLY! #
#####"
    STAGES=s1
    shift
elif [ "$1" = "-12" ]; then
    echo "#####"
# ATTENTION: Processing through Stage 1 and 2 ONLY! #
#####"
    STAGES=s12
    shift
elif [ "$1" = "-124" ]; then
    STAGES=s124
    shift
elif [ "$1" = "-2" ]; then
    echo "#####"
# ATTENTION: Processing through Stage 2 ONLY! #
#####"
    STAGES=s2
    shift
elif [ "$1" = "-4" ]; then
    echo "#####"
# ATTENTION: Processing through Stage 4 ONLY! #
#####"
    STAGES=s4
    shift
elif [ "$1" = "-24" ]; then

```

```

        echo "#####"
# ATTENTION: Processing through Stage 2 and 4 ONLY! #
#####"

    STAGES=s24

    shift

elif [ "$1" = "-1246" ]; then

    echo "#####"

# ATTENTION: Processing through all Stages! #
#####"

    STAGES=s1246

    shift

fi

echo $4

if [ $# -ne 3 ] && [ "$4" != "mp" ]; then
#if [ $# -ne 3 ];then
echo "usage:
vaPipe [-stages] <input runlist> <output sub-dir> <config sub-dir>

where <input runlist> should be in your working directory and is
formatted as follows,
for wobble:
run runNumber laserNumber
for pair:
pair onNumber offNumber laserNumber
Ex: (wobble mode)
run 30003 30001
run 30004 30001

```

Note: vaPipe will look for the files under \$VBFDIR for data runs
and \$MCDIR for simulated files

<output sub-dir> is a subdirectory of \$OUTPUTDIR

<config sub-dir> is a subdirectory of \$CONFIGDIR

type 'standard' to use the standard settings, or feel
free to create your own directory and config files,
just be sure to name your config and cut
files in the format of the other directories.

"

else

```
    if [ "$4" = "mp" ]
```

```
then
```

```
echo "#####"
```

```
# RUNNING IN MULTI PROCESSOR MODE #
```

```
#####"
```

```
    fi
```

```
#=====#
```

```
#Inputs#
```

```
#=====#
```

```
INFILE=$1
```

```
OUTPUT=$2
```

```
CONFIG=$3
```

```
#=====#
```



```
#Set Directories Here#
#=====#
#CODEDIR=/usr/local/veritas/vegas/bin
CODEDIR=$VEGAS/bin
VBFDIR=/veritas/VData
CONFIGDIR=/usr/local/veritas/configfiles/$CONFIG
OUTPUTDIR=/veritas/VData/DST/$OUTPUT
MCDIR=/veritas/VData/MCFILES
LASEROLD=foo

echo "ANALYSIS TIMES FOR ANALYSIS BEGINNING" > time.txt
date>>time.txt
echo>>time.txt
echo "run listed with start and
end times for analysis">>time.txt
echo>>time.txt

#=====#
#Checking to make sure directories and inputs exist#
#=====#
if test -f $INFILE
then
    echo Found runlist at $INFILE
else
    echo ERROR - Input file $INFILE does not exist
    exit
fi
```

```
if test -d $OUTPUTDIR
then
    echo Writing data to $OUTPUTDIR
else
    echo Making $OUTPUTDIR to write data to
    mkdir $OUTPUTDIR
fi

if test -d $CONFIGDIR
then
    echo Using Config Files here: $CONFIGDIR
else
    echo ERROR - Config directory $CONFIG does not exist
    exit
fi

if test -d $VBFDIR
then
    echo Using data from $VBFDIR
else
    echo ERROR - No data directory at $VBFDIR
    exit
fi

#=====#
#Stage 1 Data Mode#
#=====#
function Stage1_Data()
```

```

{
    echo Stage1_Data IN PROGRESS
    RUNS1D=$1
    if test -d $OUTPUTDIR
    then
if test -f $VBFDIR/$RUNS1D.cvbf
then
    $CODEDIR/vaStage1 -config=$CONFIGDIR/Stg1.config\
        -Stage1_RunMode=data $VBFDIR/$RUNS1D.cvbf\
            $OUTPUTDIR/$RUNS1D.root
elif test -f $VBFDIR/$RUNS1D.vbf
then
    $CODEDIR/vaStage1 -config=$CONFIGDIR/Stg1.config\
        -Stage1_RunMode=data $VBFDIR/$RUNS1D.vbf\
            $OUTPUTDIR/$RUNS1D.root
else
    echo Stage1data - $VBFDIR/$RUNS1D does not exist
fi
    else
echo Stage1data - output directory $OUTPUTDIR does not exist
    fi
}

#=====#
#Stage1 Laser Mode#
#=====#
function Stage1_Laser()
{
    echo Stage1_Laser IN PROGRESS

```

```

    RUNS1L=$1
    if test -d $OUTPUTDIR
    then
if test -f $VBFDIR/$RUNS1L.cvbf
then
    $CODEDIR/vaStage1 -config=$CONFIGDIR/Stg1.config\
        $VBFDIR/$RUNS1L.cvbf $OUTPUTDIR/$RUNS1L.laser.root
elif test -f $VBFDIR/$RUNS1L.vbf
then
    $CODEDIR/vaStage1 -config=$CONFIGDIR/Stg1.config\
        $VBFDIR/$RUNS1L.vbf $OUTPUTDIR/$RUNS1L.laser.root
else
    echo Stage1laser - $VBFDIR/$RUNS1L does not exist
fi
    else
echo Stage1laser - output directory $OUTPUTDIR does not exist
    fi
}

```

```

#=====#
#Stage2#
#=====#
function Stage2()
{
echo Stage2 IN PROGRESS
RUNS2=$1
LASERS2=$2

```

```

if test -f $OUTPUTDIR/$LASERS2.laser.root
then
    if test -f $VBFDIR/$RUNS2.cvbf
    then
$CODEDIR/vaStage2 -config=$CONFIGDIR/Stg2.config\
$VBFDIR/$RUNS2.cvbf $OUTPUTDIR/$RUNS2.root\
$OUTPUTDIR/$LASERS2.laser.root
        elif test -f $VBFDIR/$RUNS2.vbf
        then
$CODEDIR/vaStage2 -config=$CONFIGDIR/Stg2.config\
$VBFDIR/$RUNS2.vbf $OUTPUTDIR/$RUNS2.root\
$OUTPUTDIR/$LASERS2.laser.root
        else
echo Stage2 - $VBFDIR/$RUNS2 does not exist
        fi
        else
echo Stage2 - $OUTPUTDIR/$LASERS2.laser.root does not exist
        fi
    }

#=====#
#STAGE4.2#
#=====#
function Stage4()

{

```

```

echo Stage4.2 IN PROGRESS
if [ $# -eq 1 ]
then
RUNS4=$1
if test -f $OUTPUTDIR/$RUNS4.root
then
    $CODEDIR/vaStage4.2 -config=$CONFIGDIR/Stg4.2.config\
        -cuts=$CONFIGDIR/Stg4.2cuts.config\
        -table=$CONFIGDIR/tables/table.root\
        $OUTPUTDIR/$RUNS4.root
    else
        echo can not find $OUTPUTDIR/$RUNS4.root
    fi
else
    echo Stage4.2 - wrong number of parameters for Stage4.2 function
fi
}

#=====#
#Steps Through Analysis#
#=====#
function run()
{
    if [ $STAGES = s124 ]; then
RUNR=$1
LASERR=$2
echo $RUNR >> time.txt

```

```
date >> time.txt
Stage1_Data $RUNR
Stage2 $RUNR $LASERR
    Stage4 $RUNR
date>>time.txt
    elif [ $STAGES = s1 ]; then
RUNR=$1
LASERR=$2
echo $RUNR >> time.txt
date >> time.txt
Stage1_Data $RUNR
date>>time.txt
    elif [ $STAGES = s2 ]; then
RUNR=$1
LASERR=$2
echo $RUNR >> time.txt
date >> time.txt
Stage2 $RUNR $LASERR
date>>time.txt
    elif [ $STAGES = s4 ]; then
RUNR=$1
LASERR=$2
echo $RUNR >> time.txt
date >> time.txt
Stage4 $RUNR
date>>time.txt
    elif [ $STAGES = s12 ]; then
RUNR=$1
LASERR=$2
```

```

echo $RUNR >> time.txt
date >> time.txt
Stage1_Data $RUNR
Stage2 $RUNR $LASERR
date>>time.txt
    elif [ $STAGES = s24 ]; then
RUNR=$1
LASERR=$2
echo $RUNR >> time.txt
date >> time.txt
Stage2 $RUNR $LASERR
    Stage4 $RUNR
date>>time.txt

    fi

}

#=====#
#Reading Input File#
#=====#
{
while read TYPE RUN1 RUN2 RUN3;do
#=====#
#Wobble analysis#
#=====#
echo Reading File
case $TYPE in
    run)

```



```

RUN=$RUN1
LASER=$RUN2
if [ "$LASER" != "$LASEROLD" ] && [ "$STAGES" != "s24" ] && \
    [ "$STAGES" != "s2" ] && [ "$STAGES" != "s4" ] && \
    [ "$4" != "mp" ]
    then
        Stage1_Laser $LASER
    fi
run $RUN $LASER
LASEROLD=$LASER ;;
    20*)
RUN=$RUN1
LASER=$RUN2
if [ "$LASER" != "$LASEROLD" ] && [ "$STAGES" != "s24" ] && \
    [ "$STAGES" != "s2" ] && [ "$STAGES" != "s4" ] && \
    [ "$4" != "mp" ]
    then
        Stage1_Laser $LASER
    fi
run $RUN $LASER
LASEROLD=$LASER ;;

#=====#
#Pair analysis#
#=====#
    pair)
ON=$RUN1
OFF=$RUN2
LASER=$RUN3

```

```
Stage1_Laser $LASER
run $ON $LASER
run $OFF $LASER
echo -n $ON $OFF
Stage3 $ON $OFF
Stage4 $ON.padded
Stage4 $OFF.padded
date>>time.txt ;;
```

```
*)
echo "input file should be formatted as:"
echo "run <run number> <laser run number>"
echo "or"
echo "pair <on run number> <off run number> <laser run number>"
echo "please be sure VBFDIR has been correctly set" ;;
esac
done
} < $INFILE

chmod g+w $OUTPUTDIR/*

fi
```

A.7 vaMProc: Code

```
#!/bin/bash
```

```
INFILE=$1
```

```
OUTPUT=$2
```

```
CONFIG=$3
```

```
if [ $# = 0 ]; then
```

```
    echo "This script will process a list of  
runs on multiple processors simultaneously.  
The inputs are the same as vaPipe. It will  
split your runlist into X number of runlists,  
one for each processor. The log files for  
each processor will be created in your  
working directory as well as a stage 6  
runlist. Runlist format is slightly different  
for vaMProc.
```

```
    If you format your runlist as:
```

```
run 666 667
```

```
it will assume that the files already  
exist on uranus.
```

```
    If you format your runlist as:
```

```
20080621 666 667
```

```
it will search for the file and  
if it is not found, it will download it into  
VData."
```

```
else
```

```
    if test -d vamp
```

```
then
echo deleting old files from vamp
rm -f ./vamp/*
    else
echo creating vamp directory
mkdir vamp
    fi

#=====#
#Set Directories Here#
#=====#
CODEDIR=$VEGAS/bin
VBFDIR=/veritas/VData
CONFIGDIR=/usr/local/veritas/configfiles/$CONFIG
OUTPUTDIR=/veritas/VData/DST/$OUTPUT
MCDIR=/veritas/VData/MCFILES

#=====#
#Stage1 Laser Mode#
#=====#
function Stage1_Laser()
{
    echo Stage1_Laser IN PROGRESS
    RUNS1L=$1
    if test -d $OUTPUTDIR

then
```

```
if test -f $VBFDIR/$RUNS1L.cvbf
then
    $CODEDIR/vaStage1 -config=$CONFIGDIR/Stg1.config\  
    $VBFDIR/$RUNS1L.cvbf $OUTPUTDIR/$RUNS1L.laser.root
elif test -f $VBFDIR/$RUNS1L.vbf
then
    $CODEDIR/vaStage1 -config=$CONFIGDIR/Stg1.config\  
    $VBFDIR/$RUNS1L.vbf $OUTPUTDIR/$RUNS1L.laser.root
else
    echo Stage1laser - $VBFDIR/$RUNS1L does not exist
fi

else
echo Stage1laser - creating output directory $OUTPUTDIR
mkdir $OUTPUTDIR

if test -f $VBFDIR/$RUNS1L.cvbf
then
    $CODEDIR/vaStage1 -config=$CONFIGDIR/Stg1.config\  
    $VBFDIR/$RUNS1L.cvbf $OUTPUTDIR/$RUNS1L.laser.root
elif test -f $VBFDIR/$RUNS1L.vbf
then
    $CODEDIR/vaStage1 -config=$CONFIGDIR/Stg1.config\  
    $VBFDIR/$RUNS1L.vbf $OUTPUTDIR/$RUNS1L.laser.root
else
    echo Stage1laser - $VBFDIR/$RUNS1L does not exist
fi
fi
}
```

```

function CheckLasers()
{
    RUNLIST=$1
    LASEROLD=bar
    {
while read LASER; do
    #if [ "$LASER" != "$LASEROLD" ] && [ "$STAGES" != "-24" ] &&\
#[ "$STAGES" != "-2" ] && [ "$STAGES" != "-4" ]
    if [ "$STAGES" != "-24" ] && \
[ "$STAGES" != "-2" ] && [ "$STAGES" != "-4" ]
then
Stage1_Laser $LASER
    fi
    #LASEROLD=$LASER
done
    } < $RUNLIST
}

#Checking to see which stages will be run.
case $1 in -*)
echo WILL RUN SELECTED STAGES
STAGES=$1
INFILE=$2
OUTPUT=$3
CONFIG=$4
echo using "$INFILE" as runlist
esac

```

```
#The variable "nfiles" is an integer that counts the number of
#line in the file.
```

```
declare -i nfiles=0
declare -i runcount=0
declare -i MAXPROC=7
declare -i PROC=1
```

```
nfiles=$(less $INFILE| wc -l)
```

```
echo $nfiles files in runlist, dividing into files containing\
    approximately $((($nfiles/$MAXPROC)) files each.
```

```
echo $INFILE
```

```
#This splits the runs into maxproc number of runlists.
```

```
{
    LASEROLD=foo
    while read IN1 IN2 IN3 IN4;do
        #creating download list
    case $IN1 in
        20*)
    echo gamma1.astro.ucla.edu:/veritas/data/d$IN1/$IN2.cvbf\
        >> vamp/nrd1.vamp
    if [ "$IN3" != "$LASEROLD" ]
        then
        echo gamma1.astro.ucla.edu:/veritas/data/d$IN1/$IN3.cvbf\
        >> vamp/nrd1.vamp
```

```

fi
LASEROLD=$IN3
esac

#creating runlists for data
if [ $PROC -lt $((MAXPROC+1)) ]; then
    if [ $runcount -lt $((nfiles*PROC/MAXPROC)) ]; then
echo "$IN1 $IN2 $IN3 $IN4" >> vamp/vaMProc$PROC.vamp
((runcount= $runcount + 1))
    else
((PROC= $PROC + 1))
echo "$IN1 $IN2 $IN3 $IN4" >> vamp/vaMProc$PROC.vamp
((runcount= $runcount + 1))
    fi
fi

echo "$OUTPUTDIR/$IN2.root">>s6runlist.txt

case $IN1 in
20*)
    awk '{print $3}' $INFILE > vamp/lasers.vamp;;
    #perl /veritas/VData/Newdldata.pl -r vamp/nrdl.vamp -o\
#/veritas/VData
    #rm -f vamp/nrdl.vamp;;
run)
    awk '{print $3}' $INFILE > vamp/lasers.vamp;;
esac

```



```
done
} < $INFILE

#writing file with unique lasers
LASEROLD=foo
{
    while read LASER; do
if [ "$LASER" != "$LASEROLD" ] ; then
    echo $LASER >> vamp/lasersunique.vamp
    LASEROLD=$LASER
fi
done
} < vamp/lasers.vamp

declare -i nlasers=0
declare -i lasercount=0
declare -i LPROC=1

nlasers=$(less vamp/lasersunique.vamp| wc -l)

#splitting laser runs
{
    while read IN1; do
#if [ $nlasers -gt $MAXPROC ]; then
if [ $LPROC -lt $((MAXPROC+1)) ]; then
```

```

        if [ $lasercount -lt $((nlasers*LPROC/MAXPROC)) ]; then
echo "$IN1" >> vamp/lasers$LPROC.vamp
((lasercount= $lasercount + 1))
        else
((LPROC= $LPROC + 1))
echo "$IN1" >> vamp/lasers$LPROC.vamp
((lasercount= $lasercount + 1))
        fi
fi
done
} < vamp/lasersunique.vamp

```

```

if test -f vamp/nrdl.vamp
then
perl /veritas/VData/Newdldata.pl -r vamp/nrdl.vamp -o\
/veritas/VData
fi

```

```

#case $1 in
#    200*)
#
# perl /veritas/VData/Newdldata.pl -r vamp/nrdl.vamp -o\
#    /project/veritas/VData
#
# rm -f vamp/nrdl.vamp
#esac

```

```

#This processes the laser runs before starting the vaPipes
PROC=1
while [ $PROC -lt $((MAXPROC+1)) ]; do

    if [ $PROC -lt 4 ] # $MAXPROC
then
if test -f vamp/lasers$PROC.vamp; then
    CheckLasers vamp/lasers$PROC.vamp &> vamp/lasers$PROC.log &
fi
    else
if test -f vamp/lasers$PROC.vamp; then
    CheckLasers vamp/lasers$PROC.vamp &> vamp/lasers$PROC.log
fi
    fi
    ((PROC= $PROC + 1))
done

#Sending the runlists to vaPipe for processing.

PROC=1
while [ $PROC -lt $((MAXPROC+1)) ]; do

    case $1 in
    -*)
        vaPipe $1 vamp/vaMProc$PROC.vamp $3 $4 mp &>\
vamp/vaMProc$PROC.log &;;

```

```

    #./vaPipe $1 vaMProc2.vamp $3 $4 mp &> vaMProc2.log &
    #./vaPipe $1 vaMProc3.vamp $3 $4 mp &> vaMProc3.log &
    #./vaPipe $1 vaMProc4.vamp $3 $4 mp &> vaMProc4.log & ;;
*)
    #./vaPipe vaMProc1.vamp $2 $3 mp &> vaMProc1.log &
    #./vaPipe vaMProc2.vamp $2 $3 mp &> vaMProc2.log &
    #./vaPipe vaMProc3.vamp $2 $3 mp &> vaMProc3.log &
    vaPipe vamp/vaMProc$PROC.vamp $2 $3 mp &>\
vamp/vaMProc$PROC.log & ;;

    esac

    ((PROC= $PROC + 1))

done

echo "*****"
*****WARNING!!!*****
*****
**** DO NOT CLOSE THIS TERMINAL ****
**** WINDOW UNTIL ALL VEGAS ****
**** PROCESSES HAVE COMPLETED ****
*****"

fi

```

VITA

VITA

Daniel Gall was born the only child of David and Becky Gall in Fort Wayne, IN on September 11, 1981. He graduated from Leo Jr/Sr High School in May 2000 as valedictorian and then pursued studies at Taylor University in Upland, IN. At Taylor University, he majored in engineering physics and received a Bachelor of Science in May 2004, graduating Magna Cum Laude. He then pursued graduate studies in physics at Purdue University. He married his wife, Jacquelyn in July of 2005. Later, he received a Master of Science in physics in May 2006 and a Doctorate of Philosophy in physics in 2010. He has taken a postdoctoral research position at the University of Iowa to continue work with VERITAS and X-ray astronomy.